Universitat Autònoma de Barcelona

PhD Thesis

Resistive Memory Devices based on Complex Oxides

Author: Mr. Rafael Ortega Hernández

Supervised by:

Prof. Jordi Suñé Tarruella
Electronic Engineering Department
Universitat Autònoma de Barcelona

Prof. Ma. Teresa Puig Molina
Department of Superconducting Materials and Large Scale Nanostructures
Institut de Ciència de Materials de Barcelona, ICMAB-CSIC

PhD program in Electronic Engineering
Electronic Department

2015

Universitat Autònoma de Barcelona

Prof. Jordi Suné Taruella, full professor of the Electronic Department of the Universitat Autònoma de Barcelona and **Prof. Ma. Teresa Puig Molina**, full professor of the Superconducting Material and Large Scale Nanostructures of the Institut de Ciència de Materials de Barcelona,

Certify

That the dissertation **Resistive Memory Devices based on Complex Oxides (Dispositivos de Memoria Resistiva basados en Óxidos Complejos)** submitted by Mr. Rafael Ortega Hernández to the School of Engineering in fulfillment of the requirements for the degree of Doctor of Philosophy in the Electronic Engineering program has been performed under their supervision.

Prof. Jordi Suñé Taruella

Electronic Engineering Department

Universitat Autònoma de Barcelona

Prof. Ma. Teresa Puig Molina

Department of Superconducting Materials and Large Scale Nanostructures

Institut de Ciència de Materials de Barcelona, ICMAB-CSIC

Bellaterra, Barcelona Spain. October, 2015

Acknowledgements

I would like to thank to Prof. Jordi Suñé and Prof. Teresa Puig for the valuable guidance along this work. In the same manner, thanks to Prof. Xavier Obradors for the discussions for the understanding of the results and Prof. Enrique Miranda for his collaboration with the device model.

To the Generalitat de Catalunya through the Agència de Gestió d'Ajuts Universitaris i de Recerca (AGAUR) for providing the three-year grant for the development of this work. This work was funded by project TEC2012-32305 of the Spanish Ministerio de Econimía y Competitividad, co-funded by the EU under the FEDER program. Project MAT2011-28874-C02-01, Project MAT2014-51778-C2-1-R and infrastructure project (MINECO+FEDER) CSIC-13-4E-1798.

Thanks to my family and my friends in Mexico who supported me in the distance and encouraged me to reach the goal. Thank you to everyone for your love.

To Dr. A. Palau, Dr. M. Coll, Dr. X. Lian, Dr. Victor Rouco and Dr. A. Crespo for teaching me the fundaments of the layer deposition and experimental techniques at the beginning of the work.

To all the technician personnel who helped me to develop different experiments and measurements. From the superconductivity group to Mr. X. Palmer and Ms. M. de Palau. From the SQUID to Mr. B. Bozzo. From AFM to Ms. M. Simon and Mr. A. Gómez. From Nanoquim platform, to Dr. E. León, Mr. E. Irisarri, Ms. N. Romá, and Mr. L. Morrone. To Dr. L. Balcells and Mr. J. Cisneros for sputtering deposition. From electronic lab, to Mr. J. Hellin and to the people from X-ray lab.

Thanks to all members of the superconductivity group. To the members of the resistive switching thematic for their time in the discussion of the results. Especially to Mr. J.C. González not only for his valuable help but also for his friendship. To all senior members of the group Prof. N. Mestres and Prof. S. Ricart. To all members and former members of the superconductivity group, especially to Dr. R. Vlad for her valuable

friendship, Dr. C. Pop, and Dr. M. Tristany. To Dr. C. F. Sánchez, Dr. A. Queraltó, Dr. M. Vilardell and Dr. J. Gázquez. To Mr. P. Cayado, Ms. P. Garcés, Ms. S. de Arriba, Ms. L. Soler, Mr. F. Vallès, Mr. B. Villarejo, Mr. B. Mundet. Mr. Z. Li, Ms. J. Jareño, Mr. A. Stangl, Mr. J. Sintas, Mr. V. Rodríguez, Dr. M. de la Mata, Dr. A. Genç, Mr. R. Ortigosa, Mr. R. Ayala and Ms. C. Fu.

Thanks to my office's friends Dr. P. Niu and Ms L. Gonzalez for all their support and very nice discussions about life's problems.

Thanks to all my friends from different departments in ICMAB and UAB campus.

Thank you very much to all of you.

Abstract

Resistive Random Access Memory (RRAM) devices has been proposed as candidates to replace the actual technologies employed as non-volatile memory devices. The origin of this proposal relies on the observation of the extraordinary properties required for the scaling down of these kind of devices. In this regard, a great variety of oxide materials displaying resistive switching phenomena have been studied lately. However, the lack of understanding of the physical mechanism producing the resistive switching has limited mainly their commercialization. In this thesis, we explore the resistive switching properties of the complex oxide $La_{1-x}Sr_xMnO_3$ and bilayer $CeO_{2-x}/La_{1-x}Sr_xMnO_3$ for non-volatile memory applications. First, we study the $La_{1-x}Sr_xMnO_3$ thin layer deposition technique and perform physical and structural characterization measurements in order to fully optimize this process. In addition, microfabrication techniques are used to obtain the memristor-like metal/$La_{1-x}Sr_xMnO_3$/metal and metal/$CeO_{2-x}/La_{1-x}Sr_xMnO_3/CeO_{2-x}$/metal lateral micro-devices where the resistive switching is evaluated through I-V measurements. In line with the results, a mechanism based on the oxygen ion exchange through the metal-insulator transition is proposed as responsible of the bipolar and complementary resistive switching induced in this kind of lateral devices. Furthermore, based on volume switching induced in metal/$CeO_{2-x}/La_{1-x}Sr_xMnO_3/CeO_{2-x}$/metal bilayers, a three-terminal device is presented as innovative part of this work. The current conduction along the $La_{1-x}Sr_xMnO_3$ layer is modulated by using a metal electrode which acts as a gate terminal. As a consequence of the evaluation of the volume switching, we confirm that the CeO_{2-x} layer acts as an oxygen reservoir favouring the oxygen ion exchange with the $La_{1-x}Sr_xMnO_3$ layer and modify its resistive switching properties. In addition, we demonstrate that the resistive switching is homogenously produced inside of the $La_{1-x}Sr_xMnO_3$ layer and that the electroforming process to induce the resistive switching in bilayer devices does not produce any breakdown neither in the CeO_{2-x} nor in the $La_{1-x}Sr_xMnO_3$ layer. Finally, the conclusions derived from our results can be of relevance for the understanding of the resistive switching phenomena in complex oxides.

Resumen

Los dispositivos de Memoria Resistiva de Acceso Aleatorio (RRAM) han sido propuestos como posibles candidatos para substituir a las tecnologías actualmente empleadas como dispositivos de memoria no volátil. El origen de esta propuesta se basa en la observación de las extraordinarias propiedades requeridas para el escalamiento de este tipo de dispositivos. En este sentido, una gran variedad de óxidos que exhiben fenómenos de conmutación resistiva se han estudiado últimamente. Sin embargo, la falta de comprensión del mecanismo físico que produce la conmutación resistiva ha limitado principalmente su comercialización. En esta tesis, se exploran las propiedades de conmutación resistiva del óxido complejo $La_{1-x}Sr_xMnO_3$ y bicapa $CeO_{2-x}/La_{1-x}Sr_xMnO_3$ para aplicaciones de dispositivos de memoria no volátil. En primer lugar, se estudia la técnica de depósito de capas delgadas de $La_{1-x}Sr_xMnO_3$ y se realizan medidas de caracterización de las propiedades físicas y estructurales con el fin de optimizar al máximo este proceso. Además, se emplean técnicas de microfabricación para obtener dispositivos laterales tipo memristor metal/$La_{1-x}Sr_xMnO_3$/metal y metal/$CeO_{2-x}/La_{1-x}Sr_xMnO_3/CeO_{2-x}$/metal en los cuales se evalúa la conmutación resistiva a través de medidas I-V. De acuerdo con los resultados, se propone un mecanismo basado en el intercambio de iones de oxígeno a través de la transición metal-aislante como responsable de la conmutación resistiva de tipo bipolar y complementario inducida en este tipo de dispositivos laterales. Asimismo, basándonos en la conmutación de volumen inducida en dispositivos bicapa metal/$CeO_{2-x}/La_{1-x}Sr_xMnO_3/CeO_{2-x}$/metal se presenta un dispositivo de tres terminales como parte innovadora de este trabajo. La conducción de corriente a lo largo de la capa de $La_{1-x}Sr_xMnO_3$ se modula mediante el uso de un electrodo metálico que actúa como terminal de puerta. Como consecuencia de la observación de la conmutación de volumen, se confirma que la capa de CeO_{2-x} actúa como reservorio de oxígeno la cual favorece el intercambio de iones de oxígeno con la capa de $La_{1-x}Sr_xMnO_3$ y que además modifica las propiedades de conmutación resistiva. También, se demuestra que la conmutación resistiva se produce homogéneamente en el interior de la capa de $La_{1-x}Sr_xMnO_3$ y que el proceso de electroformado para inducir el cambio de resistencia en los dispositivos bicapa no produce ruptura alguna ni en la capa de CeO_{2-x} ni en la capa de $La_{1-x}Sr_xMnO_3$. Finalmente, las conclusiones obtenidas de los resultados de este trabajo pueden ser de relevancia para la comprensión de los fenómenos de conmutación resistiva en óxidos complejos.

Contents

Acknowledgements iv

Abstract vii

Resumen viii

Contents ix

Presentation 1

Chapter 1 Introduction 3

1.1 Overview of resistive switching in oxides 3

1.1.1 Device operation 4

1.1.1.1 Unipolar resistive switching 4

1.1.1.2 Bipolar resistive switching 4

1.1.1.3 Complementary resistive switching 5

1.1.2 Classification of resistive switching mechanisms 6

1.1.3 Three-terminal memristive devices for memory and logic applications 8

1.2 Lanthanum manganite background 10

1.2.1 Introduction 10

1.2.2 Crystal structure of $La_{1-x}Sr_xMnO_3$ 10

1.2.3 Electronic structure of $La_{1-x}Sr_xMnO_3$ 11

1.2.4 Phase diagram of $La_{1-x}Sr_xMnO_3$ 13

1.2.5 Electronic transport of $La_{1-x}Sr_xMnO_3$ 14

1.2.6 Importance of the oxygen content in of $La_{1-x}Sr_xMnO_3$ 15

1.2.7 Introduction to metal-insulator transition (MIT) 15

1.3 Ion mobility in Cerium dioxide 17

1.4 Outline of the thesis 18

Chapter 2 $La_{1-x}Sr_xMnO_3$ and CeO_{2-x} layer deposition, characterization and device microfabrication 21

2.1 Substrate preparation 21

2.2 Chemical Solution Deposition route to grow epitaxial $La_{1-x}Sr_xMnO_3$ layers 24

2.2.1 Solution preparation from acetate metal-organic precursors ... 24

2.2.2 Spin coating solution deposition ... 26

2.2.3 Decomposition at low temperature and crystallization at high temperature ... 27

2.3 $La_{1-x}Sr_xMnO_3$ layer physical and structural characterization ... 28

2.3.1 Structural characterization of $La_{0.7}Sr_{0.3}MnO_3$ thin films ... 29

2.3.2 Magnetic properties of $La_{0.7}Sr_{0.3}MnO_3$ thin films ... 30

2.4 Changes in $La_{1-x}Sr_xMnO_3$ stoichiometry ... 32

2.5 CeO_{2-x} layer deposition and characterization on $La_{1-x}Sr_xMnO_3$ ... 36

2.6 Memristor device microfabrication ... 38

2.6.1 Photolithography ... 39

2.6.2 Metal deposition through Physical Vapor Deposition (PVD) processes ... 41

2.6.2.1 Metal thermal evaporation ... 42

2.6.2.2 Metal sputtering ... 43

2.6.3 Oxide etching ... 45

2.7 Resistivity and contact resistance measurements of devices ... 48

2.8 Conclusions about layers deposition and device microfabrication ... 52

Chapter 3 Resistive Switching evaluation in $La_{1-x}Sr_xMnO_3$ layers and $CeO_{2-x}/La_{1-x}Sr_xMnO_3$ bilayers memristor-like devices ... 55

3.1 Bipolar Resistive Switching in of $La_{0.8}Sr_{0.2}MnO_3$ ... 56

3.1.2 Oxygen ion migration as the mechanism for BRS in $La_{1-x}Sr_xMnO_3$ ... 59

3.1.3 Influence of the $La_{1-x}Sr_xMnO_3$ thickness in the memory operation ... 63

3.1.4 Resistive Switching evaluation in $La_{1-x}Sr_xMnO_3$ with different stoichiometry ... 66

3.1.5 Summary of results observed in $La_{1-x}Sr_xMnO_3$ ... 68

3.2 Resistive Switching evaluation in bilayer devices ... 69

3.2.1 Evaluation of CeO_{2-x} single layer in lateral devices ... 70

3.2.2 Evaluation in $CeO_{2-x}/La_{1-x}Sr_xMnO_3$ bilayer using Ag electrodes ... 71

3.2.3 Resistive switching mechanism in bilayer devices ... 73

3.2.4 Complementary Resistive Switching in $CeO_{2-x}/La_{0.8}Sr_{0.2}MnO_3$ bilayer devices 75

3.2.5 Resistive Switching in $CeO_{2-x}/La_{0.7}Sr_{0.2}MnO_3$ bilayer devices 77

3.2.6 Conclusions about Resistive Switching in $CeO_{2-x}/La_{1-x}Sr_xMnO_3$ bilayers.. 79

3.3 Volume switching in bilayer devices 80

3.3.1 Evaluation of volume switching in three-terminal (3T) devices 81

3.3.2 Conclusions about volume switching in bilayer devices 88

3.4 Evaluation of the Resistive Switching in vertical devices 89

3.4.1 Characterization of $La_{0.8}Sr_{0.2}MnO_3$ layers on conductive Nb:STO substrate 89

3.4.2 Resistive Switching in $La_{0.8}Sr_{0.2}MnO_3$ layers and $CeO_{2-x}/La_{0.8}Sr_{0.2}MnO_3$ bilayers in vertical devices 91

3.4.3 Conclusions about resistive switching in vertical devices 94

3.5 Evaluation of the resistive switching in other different perovskite-like oxides: the case of $YBa_2Cu_3O_7$ cuprates 95

3.5.1 Characterization of $YBa_2Cu_3O_7$ cuprate layers....................... 96

3.5.2 Resistive switching in $YBa_2Cu_3O_{7-x}$-based lateral devices..... 99

3.5.3 Conclusions about resistive switching in $YBa_2Cu_3O_7$ devices... 102

Chapter 4 General Conclusions 105

Appendix A Characterization techniques overview 111

A.1 Atomic Force Microscopy (AFM) 111

A.2 X-ray diffraction (XDR)... 113

A.3 Magnetization measurements 115

A.4 Electric transport 116

A.5 Modified four-probe measurements 118

A.6 Contact resistance.. 120

A.6.1 Evaluation of the contact resistance using the cross-bridge structure 120

A.6.2 Evaluation of the contact resistance using the transmission line method 121

A.7 Resistive switching measurements setup 123

Bibliography 125

List of symbols and abbreviations 136

Publication and conference contributions 139

Presentation

There is a continuous demand of increasing the data storage capacity of non-volatile memories. Currently, flash memory devices have been expanding fast into the market. However, commercial flash memory devices will reach their technological limits in the near future due to scaling down facts [1].

One of the possible candidates to overcome this problem is the Resistive Random Access Memories (RRAM or ReRAM), sometimes termed memristors (memory resistors), based on the resistive switching (RS) phenomenon [2], [3]. These structures are ideal for crossbar memory arrays that are presently considered as the most promising implementation of memory devices [4], [5]. The basic principle of this kind of memory is to use a high resistance state (HRS) or low resistance state (LRS) to store the information data as “0” or “1”, where the transition between the two states can be achieved by electrical inputs.

On the other hand, metallic complex oxides have generated a lot of interest due to the physical properties such as high Tc superconductivity, ferroelectricity, magnetoresistance and resistive switching (RS) phenomena [6]–[8]. Among some other complex oxides, strontium-doped lanthanum manganese oxide ($La_{1-x}Sr_xMnO_3$) with perovskite structure has been reported to exhibit reversible resistive switching.

Although a number of groups have worked in the study of resistive switching based on complex oxides, there is a limited understanding of the uniform switching in perovskite oxide-based memristor devices. In addition, the physical mechanism producing the resistive switching phenomena has to be deeply understood, enhancing the possibility of development of new commercial memory devices based on this phenomenon.

In this regard, we depart from the fact that Bipolar Resistive Switching (BRS) has been demonstrated at nanoscale in $La_{0.7}Sr_{0.3}MnO_3$ layers by means of Conductive-Scanning Force Microscopy (C-SFM) strategy [9]. In order to demonstrate the feasibility of using these devices as non-volatile memory devices, we aim at fabricating uniform switching devices based on perovskite oxides and to the holistic understanding of their conduction and switching properties.

Moreover, we want to implement a three-terminal device based on volume switching [9] by using the perovskite oxide layer with fixed metal electrodes as a micro-device. Our goal is the proof-of-concept demonstration of a bulk switching memristor based on complex oxides.

Chapter 1
Introduction

The summary presented in this chapter aims at providing a comprehensive overview, introducing some basic concepts and terminology mainly used in this thesis related to materials and resistive switching phenomena.

1.1 Overview of resistive switching in oxides

In the current digital era, there is a demand to find a new kind of universal memory which can cover the market requirements such as high density and speed, low power consumption and long data retention. Dynamic Random Access Memory (DRAM) and Static Random Access Memory (SRAM) are fast and provide good performance but they are volatile, i.e., data is lost when the power supply is removed. On the other hand, Hard Disk Drives (HDD) are a cheap non-volatile memory but they are limited by the relatively poor performance, speed and reliability. Flash Memory is another type o solid state memory that is highly used in gadgets although it cannot be used as a computer's main memory due to fast degradation of the oxide during operation which eventually produces the memory failure [10].

RRAM based on the Resistive Switching (RS) effect of transition metal oxides (TMOs) has been proposed as a candidate for non-volatile memory applications not only for the possibility of scaling down into nano-devices but also for their performance and simplicity of their structures [11]. In addition, TMOs have allowed the first solid state device implementation of the memristor, a device theoretically predicted by Chua in 1971 [12]. This device is very promising for reconfigurable logic applications and for the implementation of neuromorphic computer architectures.

Recently, different oxide materials have been successfully investigated for RS effect including binary oxides and mixed valence oxides such as NiO [13], [14], TiO_2 [15], CeO_2 [16], [17], HfO_2 [18], [19], $Pr_{0.7}Ca_{0.3}MnO_3$ [20], [21] and $La_{0.7}Sr_{0.3}MnO_3$ [9], [22], [23]. However, multiple mechanisms have been proposed in order to explain the physics involved in the RS phenomena. These mechanisms are based on the formation/rupture of conducting filament [18], [24], redox process involving oxygen-drift from bulk oxide

to one metal/oxide interface [7], modification of a Schottky barrier induced by space charge [25] and metal-insulator (MIT) Mott transition [26], [27] among others.

1.1.1 Device operation

The typical metal oxide memory cell is a simple metal-insulator-metal (MIM) structure, as shown in Fig. 1.1a. The switching event from high resistance state (HRS) to low resistance state (LRS) is referred to as the "*Set*" process. Conversely, the switching event from LRS to HRS is referred to as the "*Reset*" process. In some cases, for the fresh samples in its initial resistance state, a larger voltage is needed to induce the resistive switching in the subsequent cycles. This is called the "*Electroforming*" process. The switching modes of metal oxide memory can be broadly classified into two switching modes: unipolar and bipolar [28]. In addition, we present the complementary resistive switching mode which will be discussed in the following chapters.

1.1.1.1 Unipolar resistive switching

Unipolar resistive switching (URS) means that the switching direction depends on the amplitude of the applied voltage but not on the polarity, thus set/reset can occur at the same polarity, and usually it can symmetrically occur at both forward and reversed voltages, as illustrated in Fig. 1.1b. During the Set process the current is limited by the compliance of the control system and, in most of the cases, it has to be increased to a higher value in order to achieve the Reset of the memory devices.

1.1.1.2 Bipolar resistive switching

Bipolar resistive switching (BRS) means that the switching direction depends on the polarity of the applied voltage, thus Set can only occur at one polarity and Reset can only occur at the opposite polarity, as illustrated in Fig. 1.1c. During the Set process, compliance current is used to avoid a hard dielectric breakdown. To read the data from the cell, a small voltage is applied which does not affect the state of the memory cell.

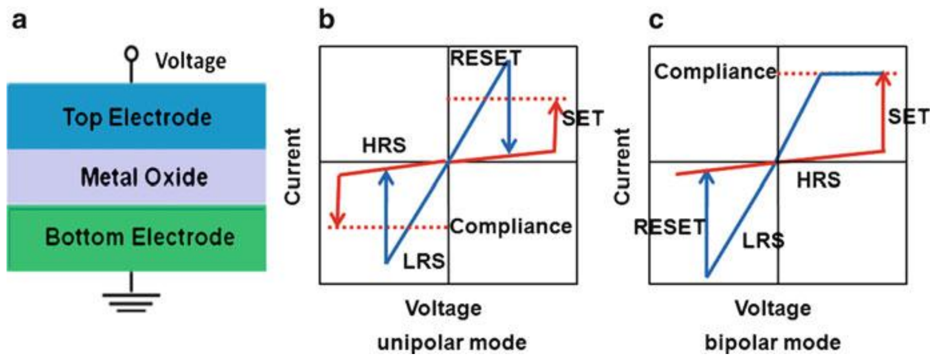

Fig. 1.1 a) Schematic of metal-insulator-metal(MIM) structure for metal oxide memory cell, and I-V curves showing two modes of operation b) unipolar and c) bipolar [28]

1.1.1.3 Complementary resistive switching

From the architectural point of view, the Complementary Resistive Switching (CRS) consists of a stack of two memristive devices anti-serially-connected as can be seen in the schematics of figure 1.2a. The result is a memory device with inert top and bottom metal electrodes and two solid-electrolyte switching layers separated by a common active electrode [29]. The two binary logic states necessary to store a bit of information correspond to the formation or rupture of a conductive filament either on the top switching layer or the bottom switching layer. In CRS a HRS is always achieved at the end of any program operation thus avoiding the presence of leaky path which is very helpful to solve the sneak-path problem in RRAM cross arrays [4].

Considering the sketch in figure 1.2b where the CRS constitutes a voltage divider if memristive element A is in the LRS and memristive element B is the HRS. Then, almost all the applied voltage drops over memristive element B until V_{th1} is reached. At this point, element B switches to the LRS and element A remains in the LRS. The CRS state is defined ON with both memristive elements in the LRS having equal voltage drop. If the applied voltage reaches V_{th2} memristive element A becomes HRS which is defined as ‘0’. On the opposite bias, for all applied voltages larger than V_{th3}, the memristive element A stays HRS and element B LRS. If a potential V comes into the range $V_{th4}<V<V_{th3}$, the HRS in element A switches to the LRS and both memristive elements are in the ON state. If the negative potential exceeds V_{th4}, element B switches back to the HRS and the resulting state is ‘1’. All the possible states in CRS are summarized in table 1.1. State ON occurs only during the read operation. State OFF is the initial state present only after fabrication in a pristine state.

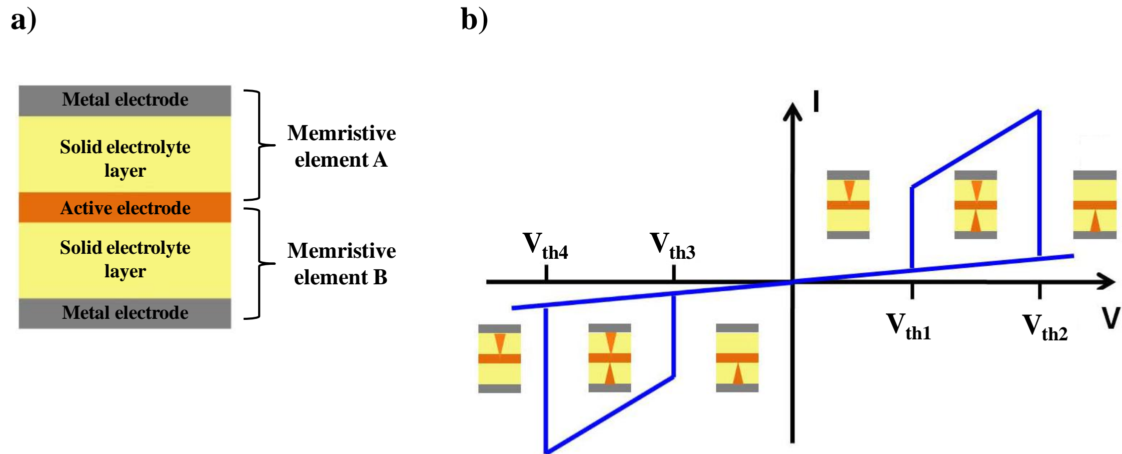

Fig 1.2 a) Schematic of the CRS memory device resulting of the combination of two anti-serially connected memristive elements A and B. b) I-V characteristics of the conventional CRS showing the evolution of the conducting filament, as an example, during the voltage sweep [29].

Table 1.1 Possible states during the CRS [4]

CRS state	Memristive element A	Memristive element B	Resistance CRS
0	HRS	LRS	≈HRS
1	LRS	HRS	≈HRS
ON	LRS	LRS	2*LRS
OFF	HRS	HRS	>>HRS

The CRS uses essentially the same principle as the CMOS inverter in which one of the transistors is always in the OFF state. As a consequence, the total resistance of the memory device becomes independent of the stored information and at the steady state the energy consumption is greatly reduced.

1.1.2 Classification of resistive switching mechanisms

In addition to classification in terms of switching behaviour, the nature of the mechanism producing this effect is also used to categorize the RS. A large variety of physical phenomena are known, which can lead to non-volatile RS memory effects. According to Waser *et al.* [7], there are three main mechanisms which involve chemical effects i.e., effects which relate to redox processes in the memristive devices either triggered by temperature or electrical voltage or both as can be seen in figure 1.3.

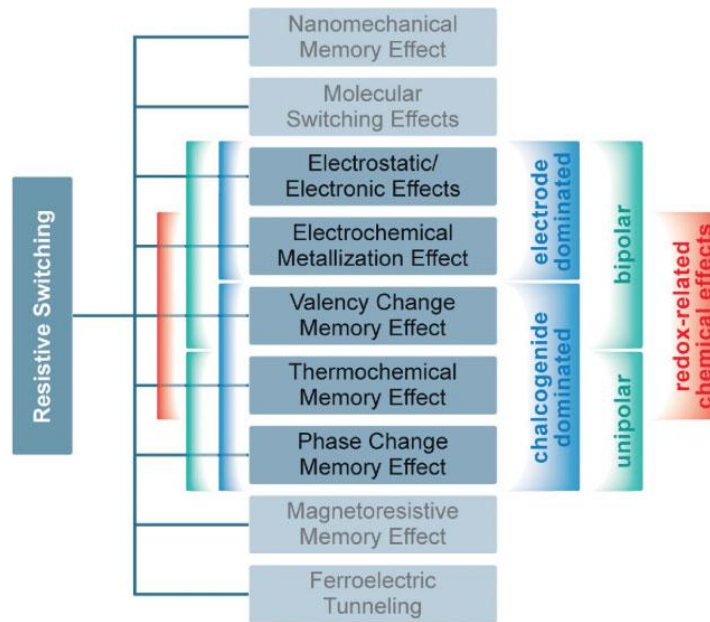

Fig. 1.3 Classification of the resistive switching effects considered for non-volatile memory applications. The mechanisms involving redox-related chemical effects are highlighted in red brackets [7].

The valence change memory effect mechanism (VCM) occurs in specific transition metal oxides such as $La_{0.7}Sr_{0.3}MnO_3$ [9], and is triggered by migration of oxygen anions, sometimes described as oxygen vacancies as well. A change in the stoichiometry of the layer leads to a redox reaction expressed by a valence change of the cation sublattice of Mn^+ and thus a change in the electronic conductivity. This memory switching is induced by voltage where the polarity determines the reduction or oxidation of the material.

On the other hand, there are two different geometrical localizations of the switching event, the filamentary switching scenario (figure 1.4a) and the area distributed switching scenario (figure 1.4b) [6]. In the first case, the formation of a conductive path is produced in the insulating matrix connecting the two electrodes in a MIM structure. This can be associated with both URS and BRS behaviour. In the area distributed switching scenario, the resistive switching takes place at the interface between the metal electrode and the oxide. This switching mechanism is usually related to the BRS behaviour observed in perovskite oxides.

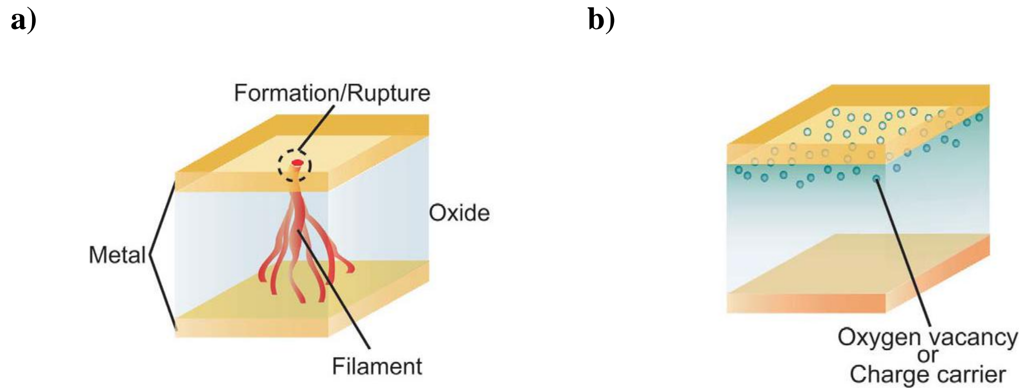

Fig. 1.4. Geometrical localization of the switching event a) filamentary conducting path and b) interface-type conducting path [6].

1.1.3 Three-terminal memristive devices for memory and logic applications

The realization of three-terminal devices to prove the implementation of gate-controlled systems for memory and logic applications is one of the main objectives of this thesis. In this regard, for electron devices, the memristive functionality can be generally attributed to a material state modification, whose dynamics can be engineered to target a specific application. The concept of three-terminal memristive device is presented in terms of memristive functionality for logic and memory applications. Examples of three-terminal memristive devices are the electrochemical organic memristor [30], the solid electrolyte nanometer switch [31], the ferroelectric FET [32], and the bipolar Si nanowire Schottky barrier FET [33], [34].

A classification [35] of three-terminal memristive devices can be based from the general concept of the FET structure (fig. 1.5a) in which memristive functionality can be inserted either by engineering the gate dielectric or by gating a memristive channel. For instance, trap charging dielectric layers inserted between the channel and the gate fall into the category of FET with capacitive memory storage (fig. 1.5b). Examples of devices falling into this category can be the flash memory for which the trap charging into the gate dielectric influences the transconductance state of the channel. A second category is the gated memristor (fig. 1.5c). An examples of this category is the solid-electrolyte nanometer switch [31]. This device shows a typical bistable resistance state but using 100 times less current than standard two terminal devices which is based on controlling the filament formation mechanism using the voltage of a gate terminal.

Figure 1.5d represents the Schottky-barrier FET with Si nanowires channel which falls in both categories of gated memristor and trap charging dielectric, as it shows dynamic trap charging mechanisms at the Schottky junctions and in the gate dielectric insulator.

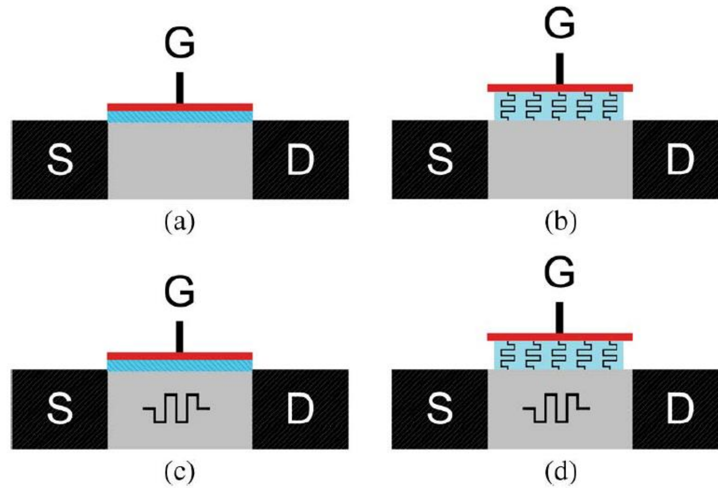

Fig. 1.5 Categorization of FET-like memristive functionality devices: a) conventional FET, b) FET with memristive gate dielectric, c) gated memristor (memristive channel) and d) gated memristor with memristive dielectric [35].

Very different applications belonging to signal processing, memory, and sensing are envisaged for three-terminal memristive devices. The possibility to build very dense crossbar arrays of two-terminal memristive devices is often seen as a disruptive technology for ultradense RRAM nonvolatile memory storage [36]. Another application that can exploit the memristive functionality is related to the design of cellular neural networks [37]. The Hodgkin–Huxley model [38] for the synapse was one of the earlier examples reported by Chua and Kang [39] of systems that can be modeled with the memristors.

1.2 Lanthanum Manganite background

In this section, an overview of the lanthanum manganite material is provided in order to introduce some basic concepts for the understanding of the resistive switching phenomena observed in this material.

1.2.1 Introduction

The term manganites refers to a kind of perovskite oxide compounds with the formula $R_{1-x}A_xMnO_3$ (R=rare earth, A=Ca, Sr, Ba, Pb) where the doping parameter x is equal to the density of carriers. Manganites belong to the family of strong correlated oxides in which diverse physical phenomena has been observed, including resistive switching (RS) phenomena [6], [11], [40]. Here, we attempt to give an overview of the fundamental properties of manganites, especially $La_{1-x}Sr_xMnO_3$, the most relevant material for this thesis.

1.2.2 Crystal structure of $La_{1-x}Sr_xMnO_3$

Figure 1.6 illustrates the crystal structure of the $La_{1-x}Sr_xMnO_3$ unit cell. The large sized La^{3+}/Sr^{2+} ions occupy the R^{3+}, A^{2+} sites located at the corners of the unit cell with 12-fold oxygen coordination while the smaller $Mn^{3+/4+}$ ions are located at the centre of an oxygen octahedron with 6-fold coordination.

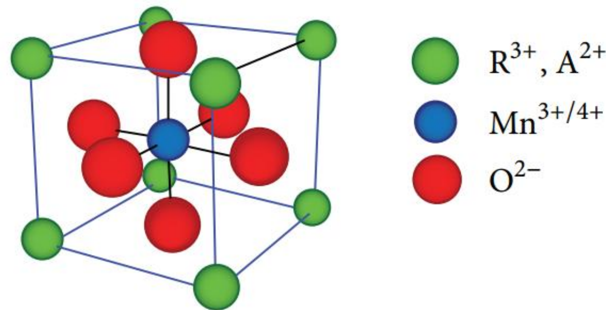

Fig. 1.6 Crystal structure of $La_{1-x}Sr_xMnO_3$ unit cell

The structure of this ideal cubic perovskite is governed by the tolerance factor (*f*) [41] which is defined as:

$$f = \frac{(R_{\mathrm{R,A}} + R_O)}{\sqrt{2}(R_{Mn} + R_O)} \tag{1.1}$$

Where $R_{R,A}$ and R_{Mn} are the ionic radii of La/Sr and Mn ions respectively, and R_O is the ionic radius of oxygen. The perovskite structure is stable for $0.89 < f < 1.02$. The value of $f=1$ corresponds to a perfect perovskite structure. Generally, this value differs from 1 and the material tends to adopt lower symmetries. The average cation radius $R_{R,A}$ influences the tilting and rotation of the oxygen octahedra with a consequent impact on the Mn-O-Mn bond angle. This bond angle, in turn, will determine some of the physical properties such as transport and magnetic properties of the manganite layers.

1.2.3 Electronic structure of $La_{1-x}Sr_xMnO_3$

The physics of manganites is mainly determined by the mixed valence of the manganese ions. In a crystal with symmetry lower than cubic, the degeneracy of the e_g and t_{2g} levels is lifted, as shown in figure 1.7, for an axial elongation of the oxygen octahedron. Although the energy of Mn^{4+} remains unchanged by such a distortion, the energy of Mn^{3+} is lowered. Thus Mn^{3+} has a marked tendency to distort the octahedral environment in contrast to Mn^{4+}. This Jahn-Teller distortion [42] is rather effective in lightly doped manganites, i.e. with a large concentration 1-x of Mn^{3+} ions

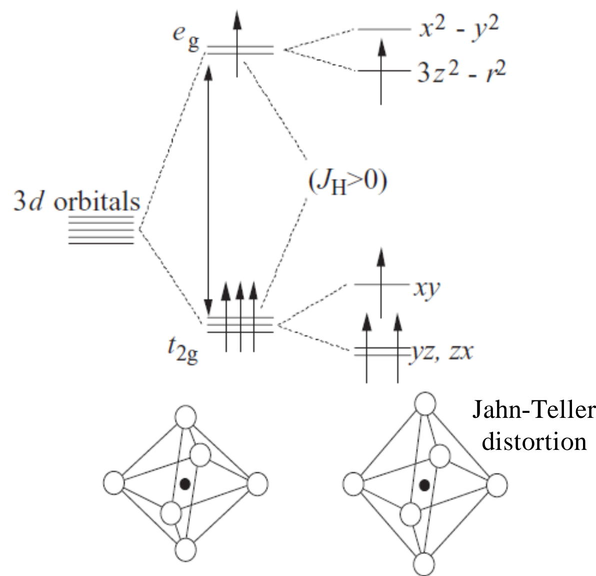

Fig. 1.7 Crystal-field splitting of the five-folded degenerate atomic 3d levels into lower t_{2g} and e_g levels of the Mn ion. The Jahn-Teller distortion of the MnO_6 octahedron further lifts each degeneracy. [43]

The reason why ferromagnetism and metallic behaviour go hand in hand in $La_{1-x}Sr_xMnO_3$ compound is based on the electronic features described above (large J_H~2-

3eV) [43]. The double exchange mechanism consist in the jump of one e_g electron to a neighbouring empty e_g state mediated by the oxygen in between [44]. In particular, the electron leaving Mn^{3+} jumps to the oxygen orbital while the electron in the oxygen with the parallel spin simultaneously jumps to the Mn^{4+} (fig. 1.8a) [45]. The probability of the e_g electron transfer from Mn^{3+} to neighbouring Mn^{4+} is $t_0{\cdot}cos(\theta/2)$, being θ the angle between the Mn spins (fig. 1.8b) [46].

a)

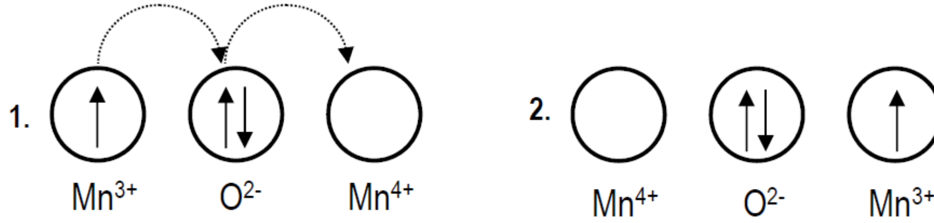

b)

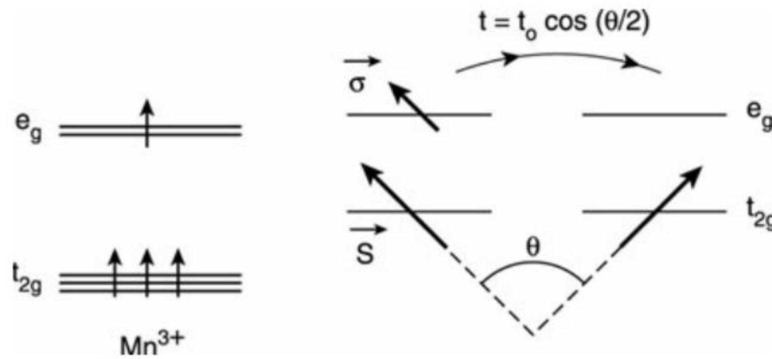

Fig. 1.8. a) Double exchange mechanism in Mn^{3+}-O^{2-}-Mn^{4+} [45] *and b)Probability of the e_g electron transfer from Mn^{3+} to Mn^{4+}* [46].

The transfer of e_g electron from Mn^{3+} to Mn^{4+} by double exchange is the basic mechanism of electrical conduction in manganites [46]. In $La_{1-x}Sr_xMnO_3$ materials with strong double exchange, the e_g electrons become delocalized in the ferromagnetic phase for a certain range of doping centred on x=0.3 and a ferromagnetic state is established. The electronic structure of such ferromagnetic phase is shown in figure 1.9. The up- and down-spin bands are separated by 1eV and the upper band is empty leading to a half-metallic behaviour. The $La_{1-x}Sr_xMnO_3$ with $x<0.5$ have a conduction band more than half-filled whereas those with $x>5$ have a conduction band less than half-filled and thus, the charge carriers are holes and electrons respectively.

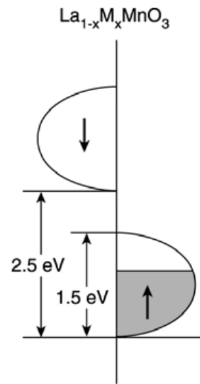

Fig. 1.9. Schematic view of the band structure corresponding to $La_{1-x}M_xMnO_3$ [47].

1.2.4 Phase diagram of $La_{1-x}Sr_xMnO_3$

The physical properties of perovskite-type manganites are determined mainly by two parameters: the average size of the cation A and the doping parameter x (in $R_{1-x}A_xMnO_3$). Both parameters are changed in manganites by acting upon a chemistry of the compound. The change in the average cation A radius (change Sr to Ca, for instance) leads to a change in the Mn-O-Mn bond angle θ which affects the probability of the e_g electron transfer. On the other hand, by changing the doping parameter x we vary the band filling n (n=1-x). In the case of $La_{1-x}Sr_xMnO_3$ compound, the doping parameter x leads to a change in the magnetic and electronic phases shown in the phase diagram of the figure 1.10 [43]. A stable ferromagnetic-metallic (FM) state, ranging from Sr doping between x=0.16 to x=0.5, is observed. A maximum T_C (~360K) is observed around x=0.3. Other phases such as paramagnetic metallic (PM), paramagnetic insulating (PI), ferromagnetic insulating (FI) and spin-canted insulating (CI) are observed.

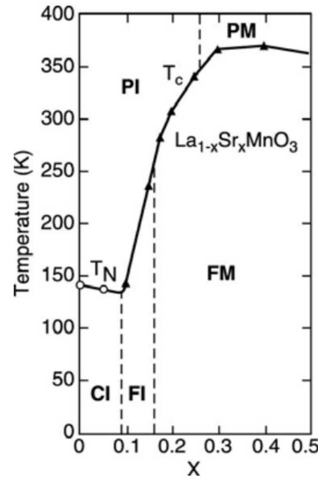

Fig. 1.10. Phase diagram showing transition temperature versus doping parameter x in $La_{1-x}Sr_xMnO_3$. [43]

1.2.5 Electronic transport in $La_{1-x}Sr_xMnO_3$

The electrical resistivity as a function of temperature depends strongly of the doping level. The temperature at which transition from insulator to metallic behaviour, and vice versa, is observed in the material is known as the metal-insulator transition (MIT) Figure 1.11 shows the curves reported by Urushibara et al. [48] on single crystal of $La_{1-x}Sr_xMnO_3$. In the set of curves two different resistivity behaviours are observed. On one hand, the metallic conduction is observed in the low temperature regime ($T<T_{M-I}$) where $d\rho/dT>0$. On the other hand, at high temperature ($T>T_{M-I}$), the curves are characteristics of a non-metallic layer, i.e., $d\rho/dT<0$. In addition, at low doping, $La_{1-x}Sr_xMnO_3$ has an insulating behaviour for all the range of temperatures. The metallic behaviour is induced by increasing the relative amount of Mn^{4+}. This is done by substitution of La^{3+} ions for Sr^{2+}. From close to x=0.2 and up to x=0.4, the material is metallic at room temperature in the bulk form.

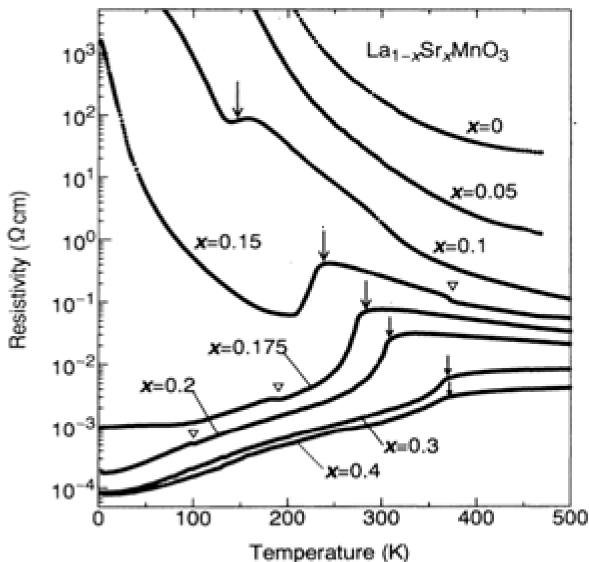

Fig. 1.11 Temperature dependence of the resistivity in $La_{1-x}Sr_xMnO_3$. The arrows indicate the temperature at which the MIT occurs. [48].

1.2.6 Importance of the oxygen content in $La_{1-x}Sr_xMnO_3$

In thin films, the oxygen content is also crucial for determining the magnetic and transport properties in manganites even at fixed doping level. The oxygen stoichiometry in manganite films can be varied by changing the pressure of the oxygen ambient gas during the growth and also by postdeposition thermal annealing in oxygen [49]. The ferromagnetic transition temperature (T_C) and the metal-insulator transition temperature (T_{M-I}) of the films progressively increase as the oxygen partial pressure during the film growth is increased. In addition, similar to what has been proposed when the doping parameter x changes in $La_{1-x}Sr_xMnO_3$, the creation of oxygen vacancies (V^0_y) may produce a valence change from Mn^{3+} to Mn^{4+} and modify the conduction due to the double exchange mechanism. This can change when biaxial strain is applied in the case of thin epitaxial films or even if the oxygen stoichiometry is varied i.e. oxygen vacancies are generated in the structure. In this case, the true ionic structure is given by $La^{3+}_{1-x}Sr^{2+}_xMn^{3+}_{1-x+2y}Mn^{4+}_{x-2y}O^{2-}_{3-y}V^0_y$ [50]. In this work, we will propose a mechanism of oxygen ion movement produced by electric field in which the resistance of the $La_{1-x}Sr_xMnO_3$ can be modified and can be used to generate two stable memory states.

1.2.7 Introduction to metal-insulator transition (MIT)

Transition metal oxides are materials with strong electron correlation which have demonstrate novel phenomena such as metal-insulator transition (MIT) among others.

The metal-insulator transition occurs in materials that change form a metallic to an insulating phase produced mainly by doping concentration. The mechanism driving the transition strongly depends on the phase composition and in many cases it is still under controversy since very small structures and electronic changes play correlated roles [51]. In general, the Mott MIT can be understood by different theories, depending on what drives the transition in the material [52].

According to the so-called electron correlation theory, in which Coulomb interaction between electrons is taking into account, the conduction happens by electron hopping through the lattice from one site to another. If the Coulomb repulsion energy U is much larger than the electrons' kinetic energy, electrons would be bounded to their original sites instead of being itinerant in the lattice. This effectively splits the original single half-filling band into a full lower band (lower Hubbard band, LHB) formed from electrons occupying an empty site and an empty higher band (upper Hubbard band, UHB) from electrons occupying a site already with one electron, as shown in figure 1.12a [53]. By tuning the splitting of the band gap given by the Coulomb repulsion U and the bandwidth W, transitions between the insulating and metallic state are allowed.

Moreover, when the degree of covalent bonding is important, the overlapping between the metal *d* and the oxygen *2p* orbitals have to be taken into account. According to the position of the oxygen band, two different situations arise as shown in figure 1.12b. If the Coulomb repulsion energy U is smaller than Δ, the energy of the so-called charge transfer gap, the material is a Mott-insulator and the gap closed during the MIT will be U. Otherwise, when the energy of the O 2p band is above of the lower Hubbard band, the gap closed during the transition will be Δ. These materials are called charge-transfer gap insulators and the role of the oxygen band is essential not only for their properties but also for their MIT.

In addition, the Mott MIT can be induced by tuning the relative magnitude of the Coulomb repulsion U to bandwidth W (U/W) through applying stress to change the atom spacing. In the case of $La_{1-x}Sr_xMnO_3$, the substitution of La^+ cation sites by Sr^+ modulates the atomic distance and consequently the MIT. Moreover, the other way to induce a MIT transition is by doping of the upper (lower) Hubbard band with holes (electrons) which can be accomplished through carrier injection by electric field. Figure 1.13 illustrates such modulation of the MIT.

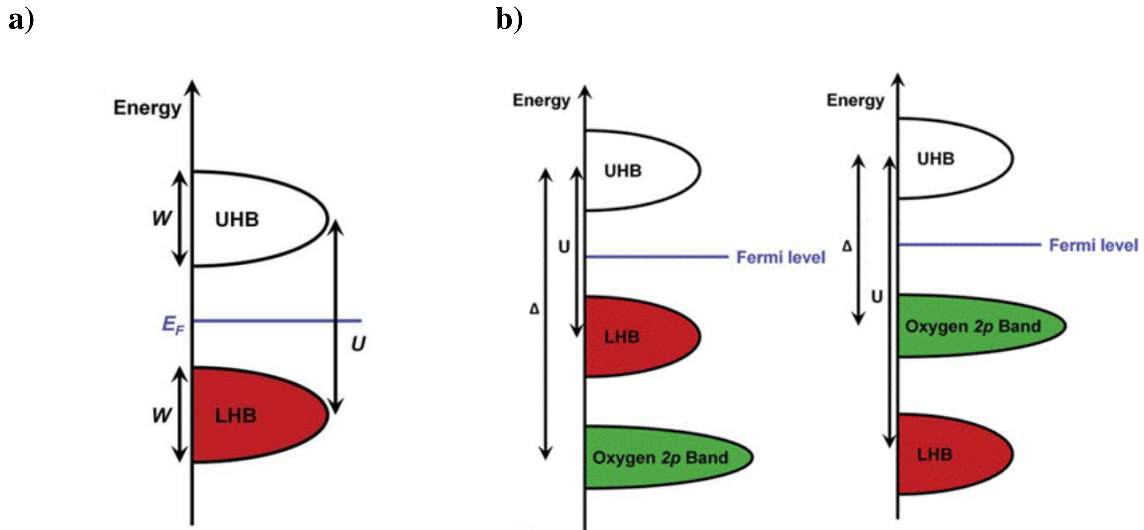

Fig.1.12 Band scheme of the of the strongly correlated electron systems. a) Band splitting into upper and lower Hubbard bands and b) charge-transfer gap insulators with two different gaps depending on which gap Δ or U is smaller. [52]

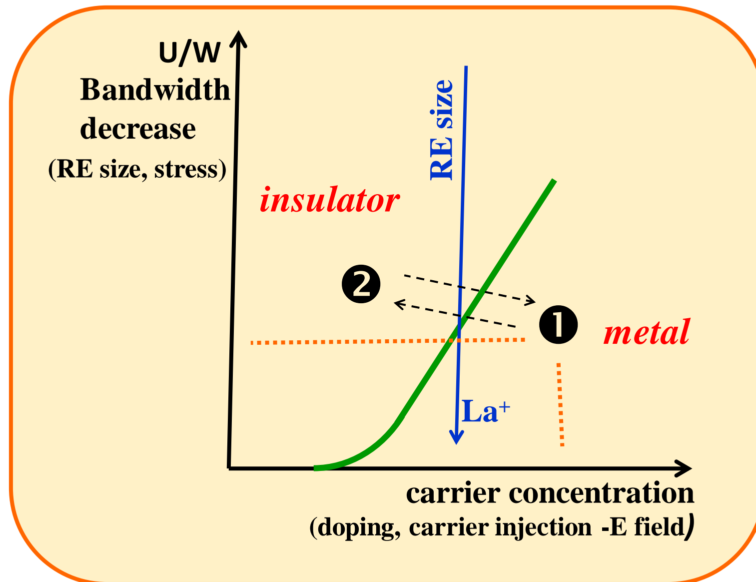

Fig.1.13.Tuning of the MIT.

1.3 Ion Mobility in Cerium dioxide

Cerium dioxide (CeO_2) is presented in this section in order to provide enough knowledge about its ability of oxygen ion conductor due to the fact that CeO_2 is used in this work as a thin layer to modify the resistive switching properties of the $La_{1-x}Sr_xMnO_3$ layers.

In the literature, CeO_2 heterostructures represent a valuable improvement for scientific and technological applications since they exhibit functional properties. For instance, CeO_2 can be used in electronics due to its compatibility with silicon, high chemical and mechanical stability and high dielectric constant of 26 [54]. Furthermore, it has been chosen as a buffer layer for coated conductors in high temperature superconductors [55]. Finally, CeO_2 also presents important catalytic properties and oxygen diffusion, very appealing for fuel cells and sensing devices [56].

In this context, CeO_2 is of our interest as a material because of its relatively high oxygen ion conductivity. Under reducing conditions, a large amount of oxygen vacancies within the CeO_2 electrolyte can be formed. Some of the Ce^{4+} is reduced to Ce^{3+}, which consequently increases the electronic conductivity [57]. As a result of reduction of the cation from Ce^{4+} to Ce^{3+} state, oxygen vacancies are formed for chemical compensation as represented in the following reaction [58].

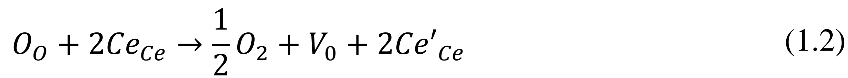

$$O_O + 2Ce_{Ce} \rightarrow \frac{1}{2}O_2 + V_0 + 2Ce'_{Ce} \qquad (1.2)$$

The mobility of oxygen ions inside of the CeO_2 layer produces an imbalance which is compensated through stoichiometry modifications. This process leads to modifications of CeO_2 to CeO_{2-x} out of stoichiometry and will be used along this thesis to act as a good oxygen capture and donor i.e. as an oxygen reservoir in $CeO_{2-x}/La_{1-x}Sr_xMnO_3$ bilayer devices upon the application of an electric field to the bilayer.

1.4 Outline of the thesis

RRAM devices has been widely investigated in the last years due to its possibility of replacing present solid state memory devices [11]. Apart from non-volatile memory devices, some other applications such as memristor-based reconfigurable electronics and neuromorphic computing architectures might have a large impact in the information and communication technologies market. However, the lack of adequate understanding of the physics of the mechanism is one of the key issues to overcome in order to transfer to market applications. In addition, the scaling down of electronic devices has opened the possibility to investigate new functional materials which can fulfill all the requirements for such applications. In this regard, $La_{1-x}Sr_xMnO_3$ has emerged as

promising material due to its resistive switching properties with large resistance ratios and multilevel operation at room temperature [9].

Giving further evidence and understanding of the resistive switching effect in $La_{1-x}Sr_xMnO_3$-based memristors devices, its characteristics as plausible non-volatile memory devices and first attempts to develop three-terminal devices where the RS effect is controlled through a gate electrode, are the main objectives of this thesis.

The manuscript has been divided in four main chapters. The present Chapter 1 includes a brief introduction to the concepts of resistive switching phenomena such as a classification according to the polarity operation and the mechanism producing the effect. In this chapter, we also present a brief description of the physical properties of the materials employed, $La_{1-x}Sr_xMnO_3$ to produce the resistive switching and CeO_{2-x} as oxygen reservoir layer. The conduction model in $La_{1-x}Sr_xMnO_3$ form the valence state of the ions point of view is presented here.

Chapter 2 presents a detailed description of the fabrication process of the devices. Here, the metal-organic decomposition chemical solution deposition (MOD-CSD) is described as methodology to grow functional $La_{1-x}Sr_xMnO_3$ thin epitaxial layers. In addition, the atomic layer deposition (ALD) is indicated as a CeO_{2-x} deposition method easy to implement together with the CSD to obtain reliable thin layers. The characterization of the structural and physical properties of these layers is also presented. In the last part of the chapter, the methodology carried out to fabricate memristor devices with microelectronic techniques is described.

In Chapter 3, the results of the evaluation of the resistive switching properties in devices based on $La_{1-x}Sr_xMnO_3$ layers and $CeO_{2-x}/La_{1-x}Sr_xMnO_3$ bilayer are presented. A mechanism based on the oxygen ion movement is presented in order to support the resistive switching phenomena in this kind of devices. In addition, one of the most promising results of this thesis, the gate-controlled volume resistive switching in three-terminal devices is presented and explained in this chapter. Finally, a first approach to vertical configuration to induce the resistive switching phenomena in $La_{1-x}Sr_xMnO_3$ and the use of another different $YBa_2Cu_3O_7$ perovskite complex oxide layer to handle the resistive switching, are presented to generalize the mechanism proposed.

The main conclusions of this research are summarized in Chapter 4. The manuscript includes, as an appendix at the end, a description of the characterization techniques employed during this thesis.

Chapter 2

$La_{1-x}Sr_xMnO_3$ and CeO_{2-x} layer deposition, characterization and device microfabrication

In this chapter, the routes followed for the deposition and growth of $La_{1-x}Sr_xMnO_3$ and CeO_{2-x} layers and the fabrication of memristor-like devices for non-volatile memory applications are presented. Based on the results obtained within the ICMAB research group where this work has been developed in collaboration with, the resistive switching characteristics were demonstrated to have a strong dependence on layers physical properties [9], [59]. In addition, studies on thin film deposition of $La_{0.7}Sr_{0.3}MnO_3$ [60] and CeO_2 [61] has been carried out indicating that their use could be suitable to accomplish the requirements of scaling down in electronic devices.

The evaluation of their physical and structural properties was carried out in order to characterize the layers and evaluate the correlation with the resistive switching characteristics as well. In this regard, Atomic Force Microscopy (AFM), X-ray diffraction (XRD), magnetization and resistivity measurements were performed to the different layers. In addition, microfabrication techniques such as photolithography, etching and metallization were implemented to obtain the final memristor devices.

Finally, in this chapter we will show that the combination of Chemical Solution Deposition (CSD) and Atomic Layer Deposition (ALD) methods, which are used to deposit the $La_{1-x}Sr_xMnO_3$ and CeO_{2-x} layers respectively, results in a non-cost-effective methodology to obtain final reliable devices. The second layer deposition method can be easily implemented without modification of the first layers properties.

2.1 Substrate preparation

Substrates play an important role in the heteroepitaxial growth of thin films, especially at the nanoscale level where interfacial effects are important. The crystal structure and properties of the oxide nanostructures are determined by the nucleation and growth on

single crystal oxide substrates [62]. A clean surface free of contaminants, with roughness in the atomic scale and high crystallinity is required. A single-terminated surface in complex oxides such as perovskite is often also desirable where an atomic-scale control of the alternating planes is necessary for tailoring their physical properties [63].

In this work, the strontium titanate $SrTiO_3$ (STO) is used as substrate owing to the fact that it has the same perovskite structure to grow heteroepitaxial $La_{1-x}Sr_xMnO_3$ layers and a tensile lattice mismatch with this layer of only 0.9%. The STO substrates are $5mmx5mmx0.5mm$ single crystal available from Crystec. They are one side polished and they have (001) crystal orientation.

In order to achieve the clean, flat surface substrate we have followed the methodology described by Koster et al.[64] where after a high temperature thermal annealing, the Sr-O termination of the STO reacts with CO_2 and water to give $SrCO_3$ and $Sr(OH)_2$, respectively. The latter hydroxide dissolves in acid solutions and leaves the more stable TiO_2 termination after a second thermal annealing.

Figure 2.1a shows the AFM image of a (001)STO substrate as received after cleaning with acetone and methanol in ultrasonic bath to eliminate non-polar and polar impurities respectively. The terraces due to the miscut angle are observed but they are not well defined. In order to improve the quality and to achieve well defined step-terraces, after the cleaning, the substrates are put in an alumina crucible. Then, this is placed inside of a tubular furnace to perform the first high temperature thermal annealing. Substrates are annealed at 900ºC for 300min under oxygen flux at 0.5 $l{\cdot}min^{-1}$. Heating and cooling rates are $15ºC{\cdot}min^{-1}$ and $10ºC{\cdot}min^{-1}$ respectively as observed in the thermal profile (fig. 2.1b). This process has been reported to generate atomically step-terraces with majority of Sr-O termination as showed in the image 2.1b. Then, in order to obtain single $Ti\text{-}O_2$ step terraces, the substrates are cleaned in ultrasound bath with Milli-Q water for 5min and attacked with a buffer fluorhydric acid solution (BHF) 5:1 for 2min. The acid is rinsed with more Milli-Q water and finally, the substrates are placed inside the tubular furnace to be treated at 950ºC 60min with heating and cooling rates of $30ºC{\cdot}min^{-1}$ and $3ºC{\cdot}min^{-1}$ respectively as observed in the thermal profile (fig. 2.1c). As a result, the more stable $Ti\text{-}O_2$ termination is observed at the substrate surface like in image 2.1c.

These images correspond to different STO substrates and are just presented to give an idea of how the substrate surface is improving in each step.

a)

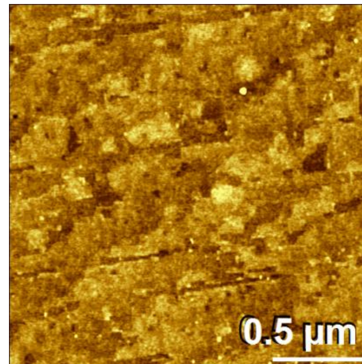

b)

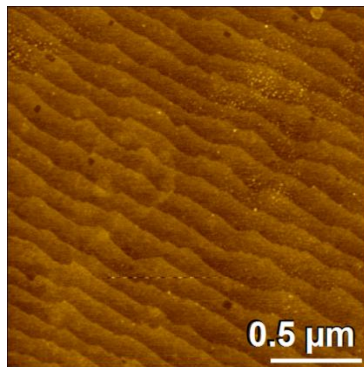

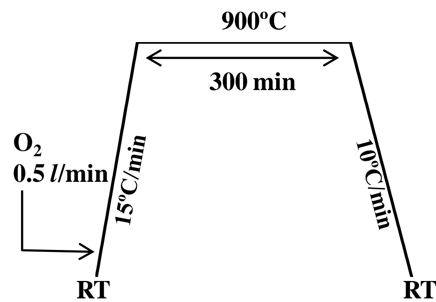

c)

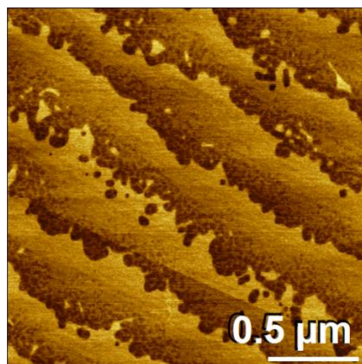

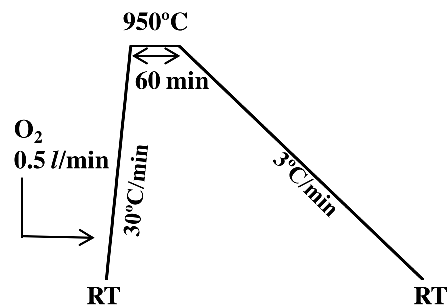

Fig. 2.1. a) As received STO substrate. b) STO with step-terraces with majority of Sr-O termination after the first thermal annealing showed next to the surface image. c) Different STO substrate after the first thermal annealing plus BHF acid attack and second thermal annealing, showing step-terraces with expected majority Ti-O_2 termination

2.2 Chemical Solution Deposition route to grow epitaxial $La_{1-x}Sr_xMnO_3$ layers

The chemical solution deposition (CSD) technique is a highly flexible method for the fabrication of electronic oxide thin films. In particular, in this work we have followed the Metal-Organic Decomposition method (MOD). This method has demonstrated the formation of perovskite-type oxides as thin films that possess the desirable properties of the corresponding bulk materials [65]–[67]. Figure 2.2 illustrates the typical CSD process that was used during the growth of epitaxial $La_{1-x}Sr_xMnO_3$ following previous experience of the group [68]. In the subsequent subsections, each step is described and discussed in detail.

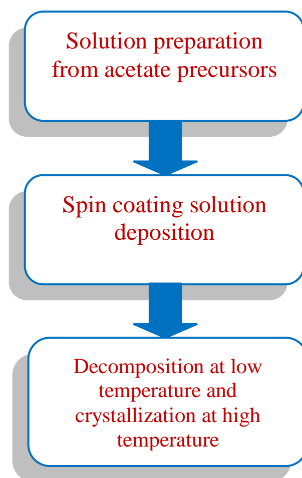

Fig 2.2. Flow chart of the Chemical Solution Deposition (CSD) method used to grow LSMO thin films in this work

2.2.1 Solution preparation from acetate metal-organic precursors

The $La_{1-x}Sr_xMnO_3$ precursor solution is synthesized from stoichiometric amounts of metal Lanthanum (La), Strontium (Sr) and Manganese (Mn) acetates. According to the molar solution, respect to the Mn, and the desired Sr content (x value in $La_{1-x}Sr_xMnO_3$), the weight of each metal salt is calculated using the following expression:

$$m = C * V * MW * x \tag{2.1}$$

Where m is the weight of acetate salts. C is the molar concentration in $mol{\cdot}l^{-1}$, which is also referred to as molarity. V is the volume of the dissolution in liters in which the indicated mass of solute is dissolved to make the desired molar concentration. It is worth noting that V is the total volume of solution, in our case, we have used 4ml of acetic acid (CH_3COOH) plus 1ml of DI water, i.e. 5ml of solvent in total. MW is the

molecular weight in g·mol^{-1} for each acetate salt and finally x is the stoichiometry relationship of each precursor of $La_{1-x} Sr_xMnO_3$. Table 2.1 indicates the weight for each salt according to the desired molarity and the stoichiometry used along this work.

Molarity (M)	Sr content (x) stoichiometry	La Acetate (g)	Sr Acetate (g)	Mn Acetate (g)
0.03	0.3	0.0331	0.0092	0.0367
0.05	0.3	0.0553	0.0154	0.0612
0.07	0.3	0.0774	0.0216	0.0857
0.1	0.3	0.1106	0.0308	0.1225
0.3	0.3	0.3318	0.0920	0.3676
0.3	0.25	0.3555	0.0771	0.3676
0.3	0.2	0.3792	0.0617	0.3676
0.1	0.2	0.1264	0.0205	0.1225
0.3	0.15	0.4029	0.0462	0.3676

Table 2.1 Calculated weight of the acetate salt used in the preparation of the $La_{1-x}Sr_xMnO_3$ *solution*

The metal acetates precursors, $La(CH_3CO_2)_3$, $Sr(CH_3CO_2)_3$ and $Mn((CH_3CO_2)_2$, are acquired from commercially available acetates (Aldrich). The *MW* of each salt, taken from supplier specifications, is shown in table 2.2

Salt	Molecular weight (MW g·mol^{-1})
Mn acetate	245.09
Sr acetate	205.71
La acetate	343.05

Table 2.2 Molecular weight of the three different acetate salts involved in the preparation of the $La_{1-x}Sr_xMnO_3$ *solution, taken from supplier specifications*

Just after the stoichiometric amounts of acetate salts are mixed with the 5ml of solvent, this initial solution is stirred up for 30min at 50ºC in a hot plate. Then, it is filtered with a 0.2µm diameter filter in order to remove the bigger particles if any, and it is kept at ambient temperature. As a result, the prepared solution has maintained the main goals of the CSD route: inexpensive starting compounds, adjustability of concentration and stoichiometry and solution handling at ambient temperature [65].

2.2.2 Spin coating solution deposition

After the synthesis, 15μl of precursor solution are deposited onto a clean and atomically flat substrate described in the past section, positioned at the center of the rotatory plate of a commercial spin-coater (fig. 2.3). This deposition is performed under low humidity conditions. The substrate attains 6000 rpm rotational speed in 1s, which is kept constant for 2min. Then, the sample is placed on top of a hot plate at 90ºC for 10min in order to dry the excess of solvent. At the end of the process, the solvent has evaporated and the substrate appears covered with a homogeneous gel layer. Under identical deposited volume, angular velocity, acceleration, and spinning time, we expect the amount of deposited material to be the same, since the wettability is the same for all substrates.

Fig. 2.3. Schematic of the spin coating solution deposition

The angular velocity and the spinning time, together with the solution viscosity, can be used to control the thickness of the film [65]. However, in this work the molar solution concentration is used to determine the thickness of the final layer. Figure 2.4 shows the measured thickness of different LSMO layers as a function of the molar concentration.

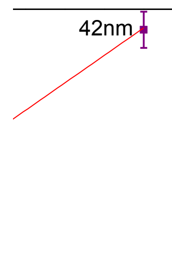

Fig. 2.4 $La_{1-x}Sr_xMnO_3$ thicknesses for different molar concentration of the deposited solution

2.2.3 Decomposition at low temperature and crystallization at high temperature

The process of the transformation of the as-deposited precursor layer into the desired crystalline phase has been carried out using a thermal treatment at high temperature. Right after deposition, the film contains an important fraction of organic material including solvent that may remain inside of the film structure. The thermal treatments are often used to eliminate those organic species and proceed to the formation of the desired oxide phase.

For this purpose, the spin-coated sample is placed in an alumina crucible in order to perform the high temperature annealing process. The samples are placed in a tubular furnace where metal-organic precursors decompose between 250ºC-300ºC according to the thermogravimetric analysis performed to the solution [69]. This decomposition is controlled by the low ratio of the heating ramp (3ºC$\cdot$min^{-1}) during the thermal treatment and the subsequent LSMO crystallization occurs at high temperatures (>700ºC).

According to the experimental conditions, the growth temperature and the dwell duration has been optimized to obtain flat and homogeneous films [70] for different concentrations of the deposited LSMO solution as observed in the thermal profiles for different samples in figure 2.5. This thermal annealing was completed under oxygen atmosphere at flowing rate of 0.6*l*·min which was introduced to the chamber at 700ºC and removed again at the same temperature during the cooling ramp [60], [70].

The AFM images in figure 2.5 show three different $La_{0.7}Sr_{0.3}MnO_3$ layers grown on STO substrates. For each concentration, the thermal process has been modified as indicated in thermal profiles under each image. Terraces can be easily distinguished in figure 2.5a for 0.03M solution but not in figures 2.5b and 2.5c. As mentioned before, the molar solution concentration determines the thickness of the final LSMO layer being the latter layers thicker than the first one but maintaining low root mean square (RMS) roughness [70].

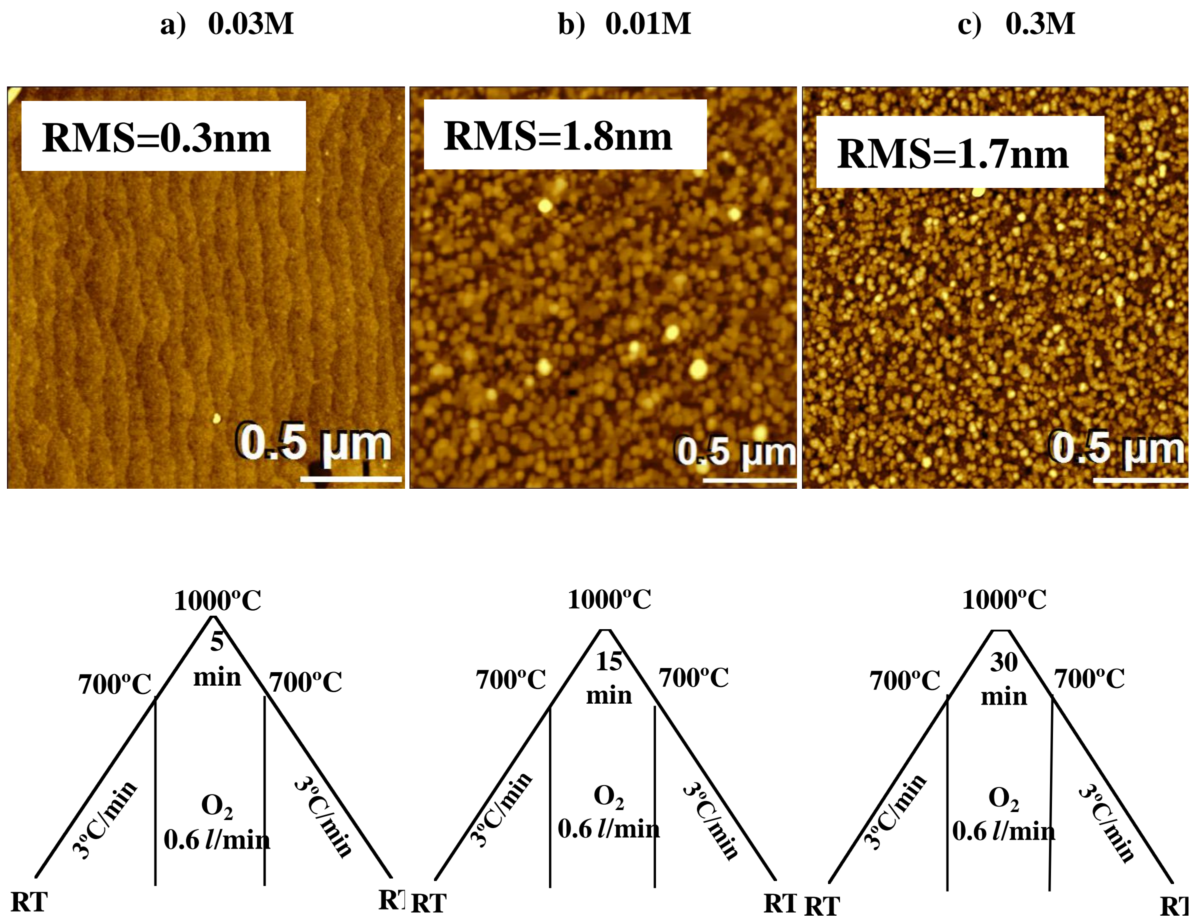

Fig 2.5 AFM images and thermal profile performed to $La_{0.7}Sr_{0.3}MnO_3$ layers on STO substrates a)0.03M, b)0.1M and c)0.3M

2.3 $La_{1-x}Sr_xMnO_3$ layer physical and structural characterization

The results of the characterization techniques used to investigate the physical and structural properties of the deposited layers are presented in this section: Atomic Force Microscopy (AFM), x-ray diffraction (XRD), magnetization measurements performed with a Superconducting Quantum Interference Device (SQUID) and resistivity measurements done with a Physical Properties Measurements System (PPMS) were used for this purpose. In the following chapters along this thesis, some of these properties are correlated with the resistive switching and device performance. In addition, an overview of these characterization techniques is presented in the appendix part.

Some of the AFM images have been already shown to demonstrate the step-terraces like in the substrate treatment (fig 2.1) and to compare the different thermal annealing process (fig. 2.5) for instance. Other properties are presented as follows.

2.3.1 Structural characterization of $La_{0.7}Sr_{0.3}MnO_3$ thin films

In order to identify the $La_{0.7}Sr_{0.3}MnO_3$ structure we conducted X-ray diffraction (XRD) measurements. The θ-2θ scans were performed with a Rigaku Rotaflex RU 200BV diffractometer using a Cu Kα radiation. Data acquisition was typically performed with a 0.02º step size. For the thinner $La_{0.7}Sr_{0.3}MnO_3$ layers, the resolution was unable to detect the $La_{0.7}Sr_{0.3}MnO_3$ peaks. The main difficulties are caused by the small amount of material, which yield a low signal, and for the fact that the intense STO substrate peaks are located close to the $La_{0.7}Sr_{0.3}MnO_3$ peaks [60].

Figure 2.6a shows the XRD peaks obtained from a scan around the (003) reflection. The most intense peaks correspond to the $K_{\alpha 1}$ and $K_{\alpha 2}$ (003)STO substrate. A shoulder, which indicates the (003) $La_{0.7}Sr_{0.3}MnO_3$ reflection, is detected around the value of 2θ=73.8º and its intensity is increasing as the $La_{0.7}Sr_{0.3}MnO_3$ layer becomes thicker. From the inset of figure 2.6a we can observe a scan from 20º-80º where the peaks of the STO substrate are detected. Since no other peaks than the (00*l*) $La_{0.7}Sr_{0.3}MnO_3$ shoulder are observed, we can conclude that the $La_{0.7}Sr_{0.3}MnO_3$ layers grown on top of the STO substrates by the CSD approach have a crystalline structure.

In addition, the Scanning Transmission Electron Microscopy (STEM) image displayed in figure 2.6b was obtained from a sample growth with similar CSD-MOD method in the ICMAB group [71]. It is observed that the $La_{0.7}Sr_{0.3}MnO_3$ is highly crystalline and grows cube-on-cube on top of the STO substrate, i.e. (00*l*)LSMO[100]‖(00*l*)STO[100]. The interface is very flat and shows no structural disorder such as misfit dislocations. These results indicate that the $La_{0.7}Sr_{0.3}MnO_3$ layer grows fully epitaxial on STO substrates and they are free of other possible organic contaminants.

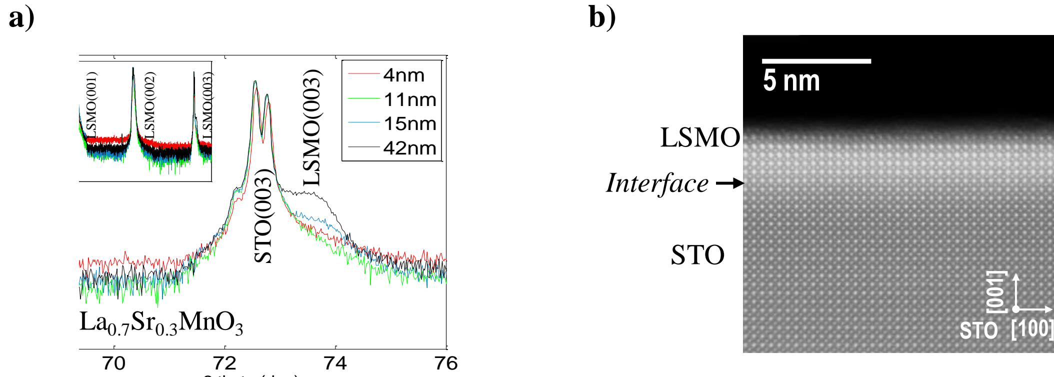

Fig. 2.6 a) XRD pattern of LSMO/STO with different thickness. The intensity of the LSMO (003) shoulder is higher as the thickness increases. The inset shows that only peaks related to the STO and LSMO b) STEM image showing that the LSMO has grown fully epitaxial. Taken from M. Roldán and J. Gázquez work [71].

2.3.2 Magnetic properties of $La_{0.7}Sr_{0.3}MnO_3$ thin films

Manganite films have been intensively studied due to their colossal magnetoresistance properties among others[48][72]. In the case of epitaxial structures, a strain relaxation of lattice mismatch between the film and the substrate at the interface, occurs as the film thickness increases beyond a certain critical thickness of the film [73]. Above this thickness, the film is relaxed to exhibit lattice constant similar to bulk sample. It has been reported that this strain may influence the physical properties by inducing a magnetic dead layer. The exact results depend a lot on the growth method employed [60], [67], [70].

The magnetic properties of the $La_{0.7}Sr_{0.3}MnO_3$ films were measured using a Superconducting Quantum Interference Device (SQUID). The magnetization loops, shown in figure 2.7a, exhibit the typical ferromagnetic hysteresis observed in $La_{0.7}Sr_{0.3}MnO_3$ layers [48], [70]. These measurements were performed at constant temperature of 35K while the magnetic applied field was varying between ±30kOe. In the figure, the scale has been adapted in order to clearly show the ferromagnetic hysteresis behavior of the $La_{0.7}Sr_{0.3}MnO_3$ samples. It has been reported that bulk $La_{0.7}Sr_{0.3}MnO_3$ exhibits a magnetization of ~590kA/m [48][74]. In figure 2.7a, the saturation magnetization (M_S) decreases with thickness which is more evident in figure 2.7b. This could be attributed to strain and critical thickness effects of the dead layer described above. As a result, we can calculate the contribution of this dead layer to the total volume of the $La_{0.7}Sr_{0.3}MnO_3$ layer assuming that it is homogenously distributed in the whole $5x5mm^2$ of the substrate. In the case of the $La_{0.7}Sr_{0.3}MnO_3$ layer with

thickness of 15nm, the calculated dead layer is ~1.3nm and ~2.6nm for the $La_{0.7}Sr_{0.3}MnO_3$ layer with thickness of 4nm.

a) b)

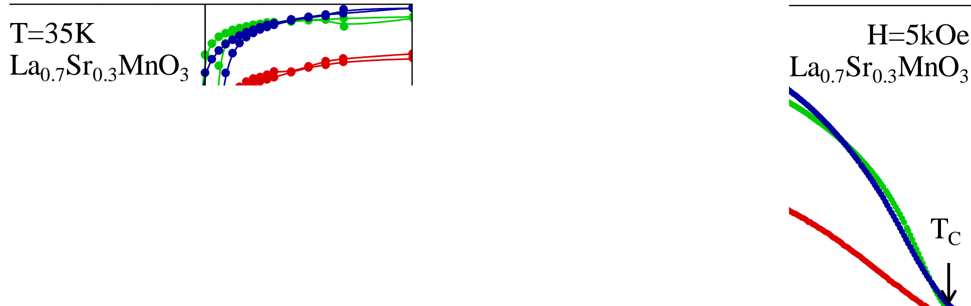

Fig. 2.7. Magnetic characteristics of $La_{0.7}Sr_{0.3}MnO_3$ with different thickness. a) Magnetization as a function of applied magnetic field where ferromagnetic hysteresis is observed. b) Magnetization as a function of temperature where the T_C value decreases with thickness.

The magnetization dependence of temperature is shown in figure 2.7b for three different $La_{0.7}Sr_{0.3}MnO_3$ thicknesses. These measurements were performed at constant magnetic field of 5kOe where it has been observed that the magnetization has decreased with the thickness as well. However, we can observe that the ferromagnetism is maintained at room temperature (300K) in all cases. A ferromagnetic-paramagnetic transition is observed with different Curie temperature (T_C) for each sample. A comparison of the T_C for $La_{0.7}Sr_{0.3}MnO_3$ with different thickness is shown in figure 2.8. Here, T_C is kept at the bulk values of 360K. The CSD-MOD method [67] is so far the only that could preserve T_C=360K even in 4nm films.

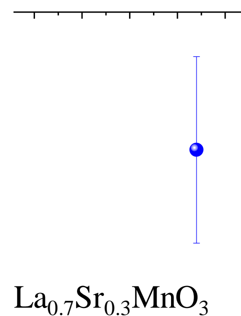

Fig 2.8. Curie temperature T_C as a function of LSMO thickness.

Therefore, we can conclude that CSD-MOD method is reliable method to obtain high quality epitaxial thin films of $La_{1-x}Sr_xMnO_3$.

2.4 Changes in $La_{1-x}Sr_xMnO_3$ stoichiometry

The change in stoichiometry in $La_{1-x}Sr_xMnO_3$ has been carried out in order to study the possible effect on the resistive switching behavior. By using the CSD method, stoichiometry can be easily modified during the solution preparation described before.

It is known that the electrical and magnetic properties of the perovskite structure $LaMnO_3$ can be enhanced by chemical doping, introducing a divalent cation such as Sr^{2+} into La^{3+} cation sites. The valence disproportion which is caused by the substitution of this La^{3+} by Sr^{2+} is balanced with the conversion of Mn valence state from Mn^{3+} to Mn^{4+}. This valance state transformation was proposed by Jonker et al. [75] and the ionic structure of the La_{1-x} Sr_xMnO_3 is balanced as $La^{3+}{}_{1-x}Sr^{2+}{}_xMn^{3+}{}_{1-x}Mn^{4+}{}_xO_3$ [22]. The created Mn^{4+} combines with Mn^{3+} and O^{2-} ions and creates a Mn^{3+}-O^{2-}-Mn^{4+} bond. The Mn ions can exchange their valences between Mn^{3+} and Mn^{4+} through simultaneous jumping of electrons in the 3*d* shell which contributes to electron conduction in LSMO. This electron conduction mechanism is referred as the double exchange theory [76] which leads to a change in the physical properties of the LSMO layers. Additionally, an interaction with the lattice takes place via Jahn-Teller distortions around the Mn^{3+} ion [77]. The degrees of freedom of the spin, orbital and charge open the field for a rich phase diagram with antiferromagnetic, ferromagnetic and paramagnetic phases which may be conducting or insulating [48].

In this work, $La_{1-x}Sr_xMnO_3$ layers with different Sr_x content ($0.15<x<0.3$) were deposited to elucidate the effect of the resistive switching properties. The same CSD method described before, including the substrate treatment, the solution preparation and the final thermal annealing, was followed in order to compare the results among these samples. The thermal annealing used to grow $La_{1-x}Sr_xMnO_3$ with different Sr content (stoichiometry) was the same studied before according to the molarity of the deposited solution. The surface characterization with AFM images is shown in figure 2.9. Four different samples with Sr_x doping concentration of x=0.3 (fig. 2.9a), x=0.25 (fig. 2.9b), x=0.2 (fig. 2.9c) and x=0.15 (fig. 2.9d) are compared. In any case, the step-terraces of the STO substrate are observed due to these images belong to samples with 42nm in

thickness. In addition, low RMS roughness is observed in all cases. Moreover, in LSMO x=0.3 and x=0.2 images small located porosity at the surface is evident maybe indicating an initial dewetting process due to the high temperature [78]. However, these defects do not modify the $La_{1-x}Sr_xMnO_3$ properties as can be seen later in this work.

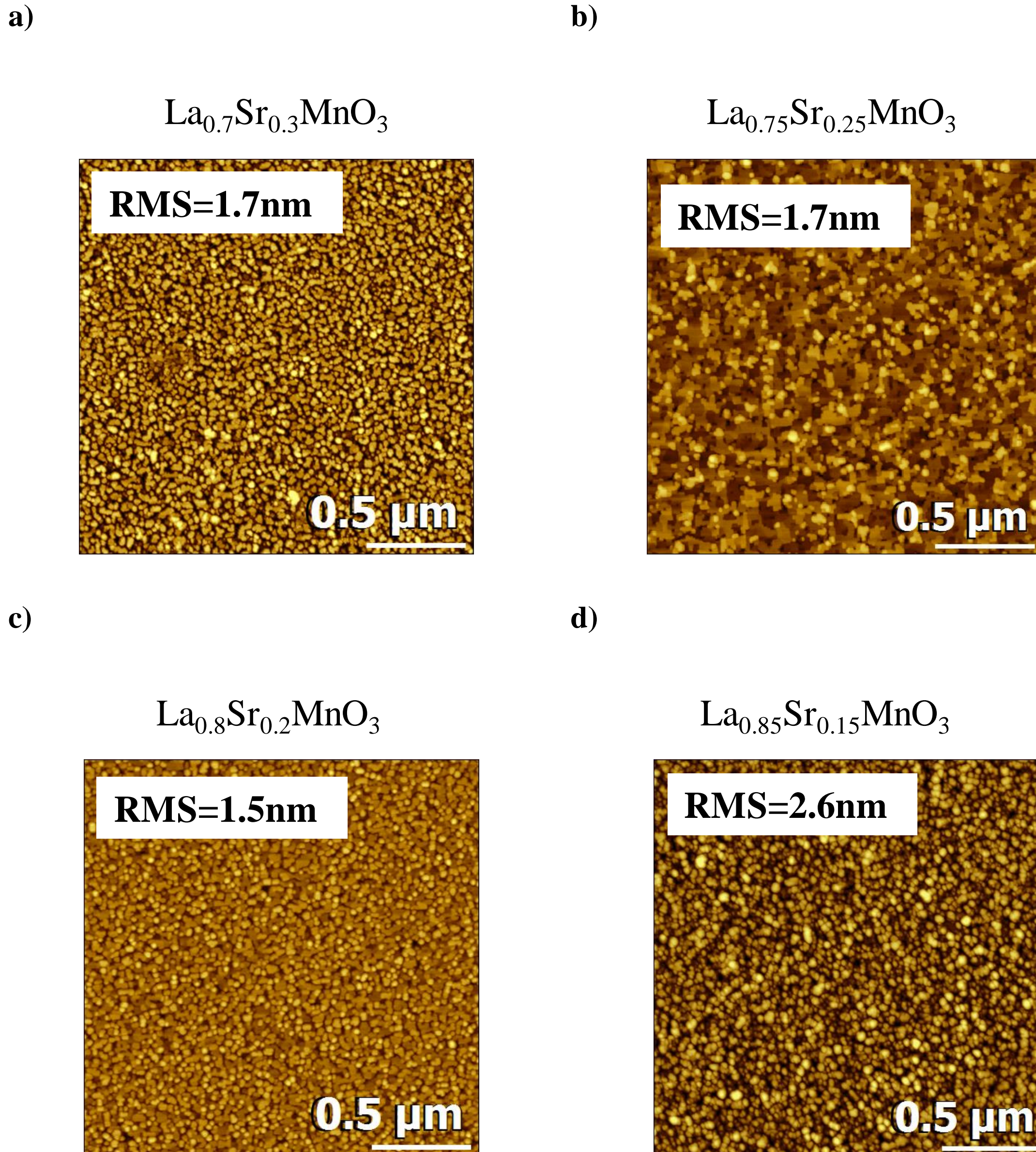

Fig. 2.9. AFM images of four different samples with La doping concentration of a) x=0.3 b) x=0.25 c) x=0.2 and d) x=0.15. No steps terraces are observed due to they are 42nm in thickness.

On the other hand, the magnetic properties as a function of temperature are shown in figure 2.10a. In this figure the M_S decreases as the Sr content. The ferromagnetic-paramagnetic transition temperature T_C is observed to decrease as the doping concentration as well. This can be better observed in figure 2.10b where the T_C is plotted as a function of the Sr content x.

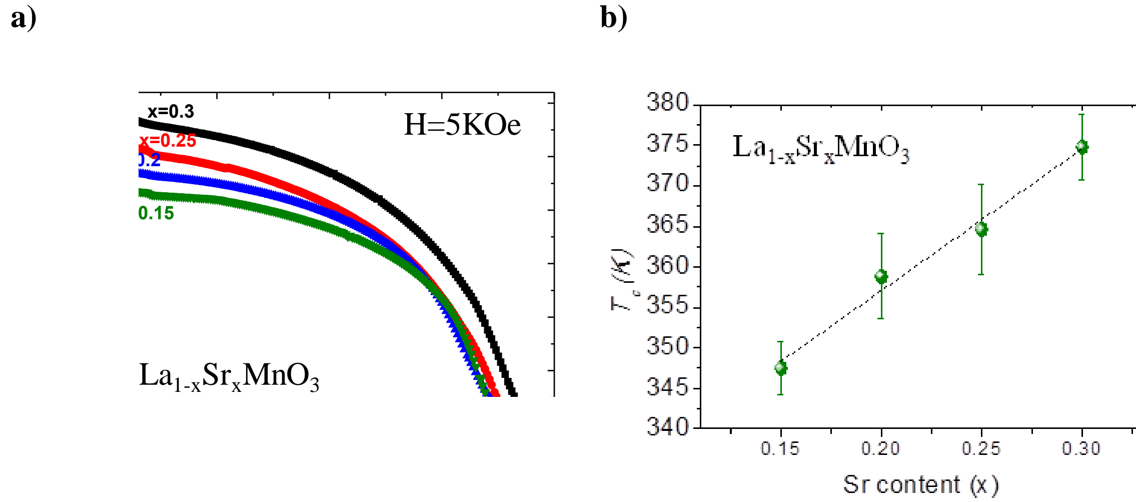

Fig. 2.10. a) M(T) for different stoichiometry (x) of $La_{1-x}Sr_xMnO_3$ b) Comparison of the T_C measured for these layers.

Urushibara et al. studied the evolution of the T_C for different Sr content in $La_{1-x}Sr_xMnO_3$ layers [48]. They observed similar trend in single crystals grown by the floating zone (FZ) method [79] while adopting different stoichiometries between $0<x<0.6$. A maximum T_C value is reported for x=0.3 and decreasing while Sr content decreases until 238K for x=0.15. In our measurements, T_C values for all stoichiometries are over 300K which means that layers are ferromagnetic at room temperature.

The growth method, crystal structure and thickness of the films can influence their final physical properties due to different impact in the strain microstructure. For instance, in line with the results of Angeloni *et al.*[80] and Tsui *et al.*[81], different T_C values of $La_{2/3}Sr_{1/3}MnO_3$ have been reported for PLD and Sputtering growth techniques respectively.

In addition to magnetic properties, electric transport properties of the CSD-derived thin $La_{1-x}Sr_xMnO_3$ films were also investigated. The temperature dependence of resistivity, ρ(T), was measured with the Van der Pauw method [82] using a Physical Properties Measurement System (PPMS, Quantum Design). An overview of this method is provided in the appendix section. Figure 2.11 shows the resistivity behavior of LSMO films grown on STO from different stoichiometries. Metal-insulator transition (MIT) has been observed for all samples. In the figure, the arrows indicate the metal-insulator transition temperature.

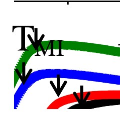

Fig. 2.11. Resistivity as a function of temperature for different LSMO stoichiometries. The arrows indicate the metal-insulator transition for each layer.

Metallic conduction is observed in the low temperature regime (T<T_{MI}) where *dρ/dT*>0. In the high temperature (T>T_{MI}), the curves are characteristics of a non-metallic layer, i.e., *dρ/dT*<0. In all cases, the MIT is accompanied by a maximum in the resistivity. At room temperature, all samples are in the metallic state as expected for the stoichiometry employed. The resistivity value at room temperature (300K) is plotted as a function of the Sr content in figure 2.12a. From this plot, we can observe that the resistivity decreases as the Sr doped concentration x increases, indicating that the $La_{1-x}Sr_xMnO_3$ layers become more conductive. In the curve, similar resistivity values were measured for samples with x=0.25 and x=0.3.

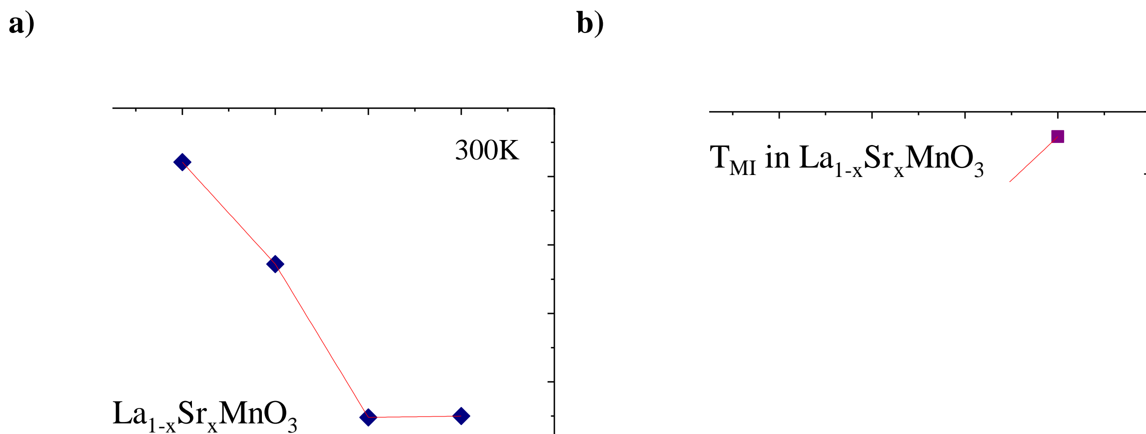

Fig. 2.12. a) Resistivity values measured at 300K and b) the T_{MI} as a function of Sr doping concentration.

Moreover, the T_{MI} as a function of the Sr content x is plotted in figure 2.12b. A transition temperature of 303K has been measured in $La_{1-x}Sr_xMnO_3$ sample with Sr content x=0.2. The temperature transition has a maximum value for $La_{1-x}Sr_xMnO_3$ with x=0.3 and decreases for samples with x=0.25 and x=0.2. However, an unexpected increase is observed for $La_{1-x}Sr_xMnO_3$ x=0.15. This seems to indicate that the oxygen stoichiometry is not kept constant in all layers and that oxygen vacancies could be present already at the synthesis stage particularly if the Sr content increases. Non-oxygen stoichiometric films have been previously reported [83] to be a general trend in thin film growth due to the strain induced by the substrate.

2.5 CeO_{2-x} layer deposition and characterization on $La_{1-x}Sr_xMnO_3$

In this section we will introduce the CeO_{2-x} thin layer characterization that was used to modify the resistive switching characteristics of the $La_{1-x}Sr_xMnO_3$ layers in $CeO_{2-x}/La_{1-x}Sr_xMnO_3$ bilayer devices. Recently in the group, modifications of the bipolar resistive switching (BRS) behavior in bilayer $CeO_{2-x}/La_{0.7}Sr_{0.3}MnO_3$, has been demonstrated by using C-SFM approach [59]. In addition, memristors with CeO_2 as a dielectric have also been proposed for memory applications [16]**.** On the other hand, the CeO_2 has been studied as electrode material in solid oxide fuel cell anodes for its high oxygen ion conduction [84].

In this work, CeO_{2-x} has been deposited by Atomic layer Deposition (ALD) technique. ALD is a chemical gas-phase deposition technique where the film growth proceeds through self-limiting surface reaction achieved by alternating the precursor gases in the chamber [85]. Here, CeO_{2-x} films were prepared in a Cambridge Nanotech Savannah 200 flow-type ALD reactor using commercial $Ce(thd)_4$ (thd = tetrakis(2,2,6,6-tetramethyl-3,5-heptanedionato) (STREM) and ozone (O_3) as the oxygen source at 275ºC. M. Coll et al. [61] have carried out a complete study of the CeO_2 deposition at low temperature achieving epitaxial nanometric layers growth on different substrates. Their results have been used in this work. The thickness of the CeO_2 layers studied was in the range between 4nm-16nm according to the pulse number of the precursors. In this work, we have used 10nm layers. They have also demonstrated that the structural and physical properties of the $La_{1-x}Sr_xMnO_3$ are not modified after ALD-CeO_2 deposition [59]. The growth of the ALD layers used in this work has been undertaken by Dr. M.

Coll from the ICMAB group, whereas the CDS growth and all the characterizations were done by this PhD student.

In order to confirm the latter results, we investigated the surface modification of the CeO_{2-x} /$La_{1-x}Sr_xMnO_3$ bilayer. First, following the CSD methodology, $La_{0.7}Sr_{0.3}MnO_3$ was grown on STO substrate. The surface of this layer was analyzed by AFM as shown in figure 2.13a. The RMS value of this layer is 2.3nm. Then, CeO_{2-x} 10nm is deposited on top of this layer and the surface is analyzed again. Figure 2.13b show the AFM image where RMS is 2.5nm. In addition, the same CeO_{2-x} 10nm layer has been deposited on single conductive STO doped Niobium (Nb:STO) substrate in order to evaluate its own resistive switching characteristics. The substrate followed the same preparation as undoped STO substrates described before. The AFM image of this layer is shown in figure 2.13c. In this image, the step terraces are also reproduced with RMS=1.4nm.

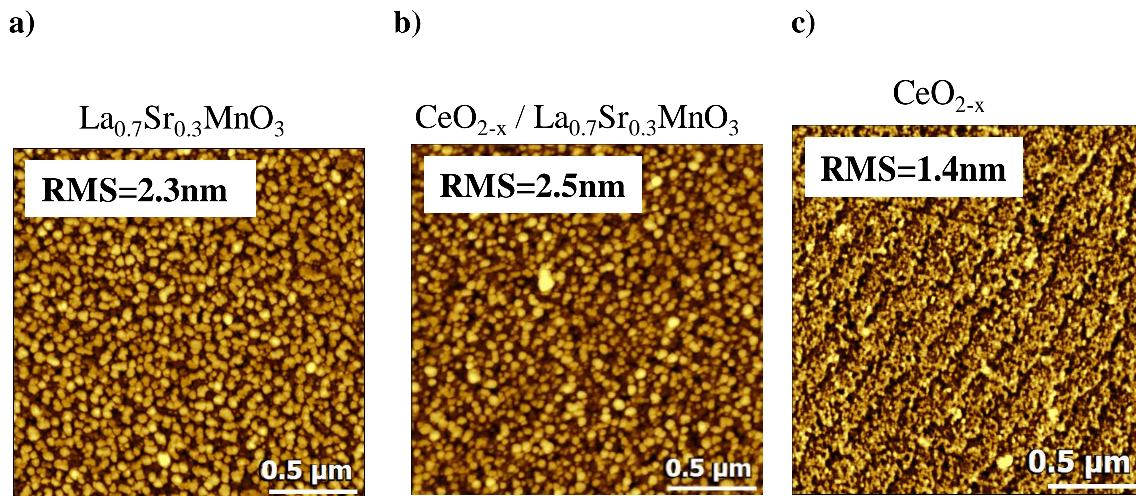

Fig 2.13. AFM images of a)$La_{0.7}Sr_{0.3}MnO_3$ layer which was used to deposit 10nm of CeO_{2-x} by ALD b) bilayer CeO_{2-x}/ $La_{0.7}Sr_{0.3}MnO_3$ and c) CeO_{2-x} on STO doped Nb

On the other hand, in order to evaluate the effect of ALD conditions on the $La_{1-x}Sr_xMnO_3$ physical properties we measured the magnetic properties. These measurements were performed on $La_{0.7}Sr_{0.3}MnO_3$/STO sample before and after CeO_{2-x} deposition. Figure 2.14 shows the magnetization as a function of temperature when an in-plane magnetic field of 5kOe is applied while varying the temperature from 10K to 400K. We can observe from the figure that the T_C is around 370K and this is no modified after the CeO_2 deposition. As a result, we can conclude that the ALD CeO_2

deposition is completely compatible method with the CSD and combining both techniques, microdevices for electronic applications can be successfully fabricated.

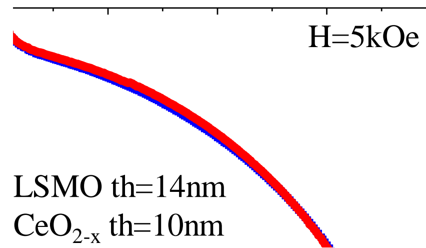

Fig. 2.14 Magnetization as a function of temperature performed to $La_{0.7}Sr_{0.3}MnO_3$ before and after CeO_{2-x} deposition by ALD at low temperature

2.6 Memristor device microfabrication

In this section, the memristor device microfabrication is presented. Different techniques such as photolithography, etching and metallization process are described in detail in order to provide enough knowledge about the device fabrication. No experience existed in the group about the overall fabrication processes and thus knowledge needed to be gathered during this thesis. Figure 2.15 describes the complete fabrication process followed to obtain the memristor devices. The optimization of the step processes have been done in order to maintain the $La_{1-x}Sr_xMnO_3$ properties described before. In addition, resistivity and contact resistance measurements were performed in order to fully characterize the fabrication process. Photolithography, etching and metal deposition processes were performed in the clean room facilities at the Institut de Ciència de Materials de Barcelona (ICMAB-CSIC).

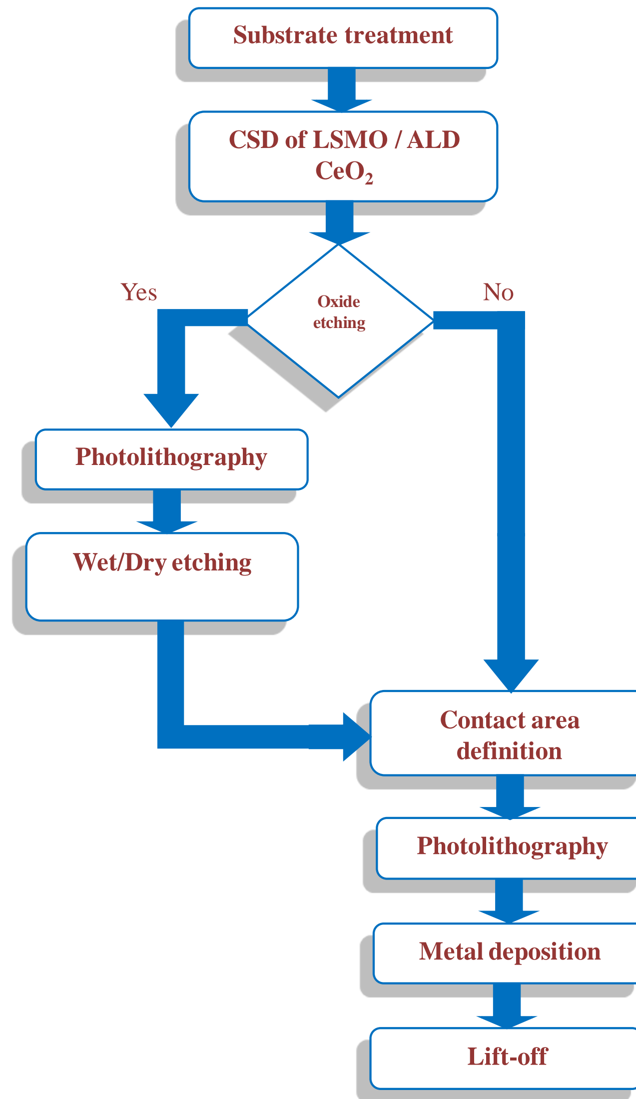

Fig. 2.15. Flux diagram of the fabrication process followed to obtain memristor devices for the valuation of resistive switching.

2.6.1 Photolithography

Lithography is a technique used to transfer a pattern onto a substrate (silicon, glass, etc.). This pattern is subsequently used to etch an underlying thin film or as a contact definition area. Photolithography refers to a one type of lithography that uses a light source (ultraviolet UV) to define the transferred patterns. This technique is by far the most widely used lithography technique in the microelectronic fabrication [86]. The starting point is the design of the pattern layout by using specialized software which is very useful due to the fact that modifications of the layout can be easily done. This layout is used as a photomask to transfer the pattern to the sample according to the process described in figure 2.16. The photoresist is a polymeric photosensitive material

which can be spun onto the sample in liquid form. The spinning speed and photoresist viscosity will determine the final resist thickness. Two different kinds of photoresist are available: positive and negative. With positive resist, UV-exposed areas will be dissolved in the subsequent development stage, whereas with negative photoresist, the exposed areas will remain intact after development [87]. Due to its better performance with regard to process control in small geometries, positive resist is the most extensively used in the very-large-scale integration (VLSI) processes [88].

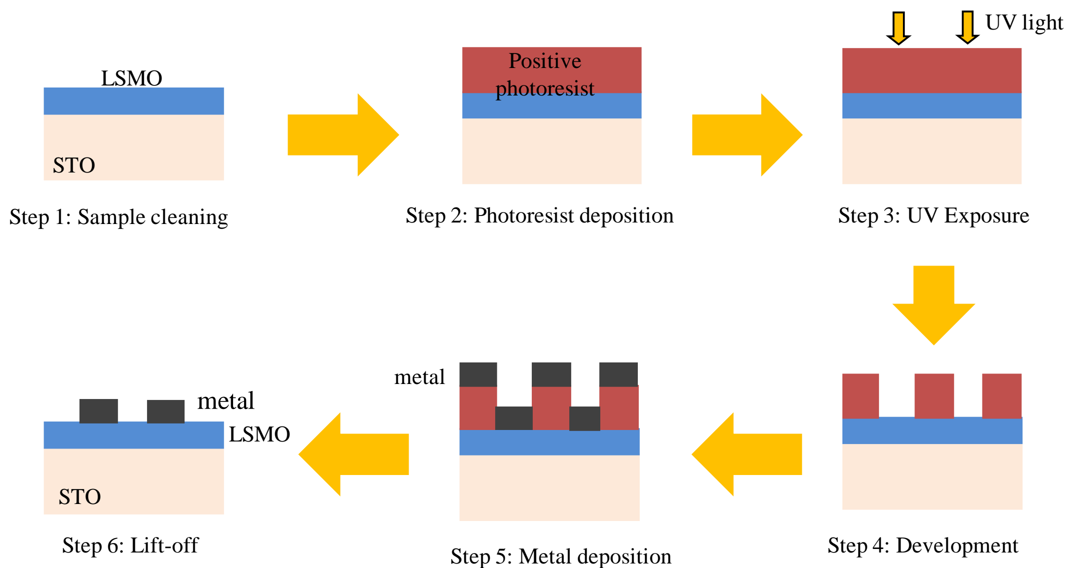

Fig. 2.16. Photolithography process followed to obtain the memristor devices.

1. After deposition of LSMO and/or CeO_2, the sample is cleaned in ultrasound bath with acetone by 5 min in order to remove impurities from the sample surface.
2. The photolithography process starts with spin-coating the substrate with a photoresist. Along this work, positive photoresist MOCROPOSIT S181342 is deposited by spin-coating at 5000rpm for 20sec. After spinning the photoresist onto the sample, it is soft-baked at 90ºC for 1min in a hot plate in order to remove the solvents from the resist and improve adhesion.
3. Subsequently, the exposure of the sample is performed. A MicrowriterML by Durham Magneto Optics is used in this stage. The sample is placed in a chamber where an autofocus correction and alignment is performed prior the exposure. Once these tasks have been successfully completed, the layout is loaded through software, specifying the dose correction and the desired laser exposure thickness

(UV source). Typical values of dose correction for LSMO samples are between 200-250mJ/cm^2 using a laser of 1µm which is in this case, the minimum size of the transferred pattern that can be accomplished. The time required to carry out this step is around 30min and it is automatically calculated by the software. This process is known as direct-write lithography process [89].

4. Then, once the exposure stage has finished, the photoresist is developed in a solution composed of water 98% and tetramethyl ammonium 2% MICROPOSIT MF-319 for 45seg. The exposed areas are dissolved, leaving trenches in the photoresist, where the sample surface is ready for metal deposition. At the same time, the undeveloped areas act as a protection where metal deposition is undesirable. At the end of this stage, the photoresist thickness is around 1.4µm. Figure 2.17 shows the images of the photolithography process performed on a $La_{0.7}Sr_{0.3}MnO_3$ sample.
5. Metal deposition stage through metal evaporation or sputtering is carried out. These techniques are explained in detail in following subsection.
6. Finally, metal lift-off step is performed. The photoresist and uncovered metal areas are removed by rinsing the sample in acetone. As a result, the sample structure has been accomplished as shown in step 6 of figure 2.16.

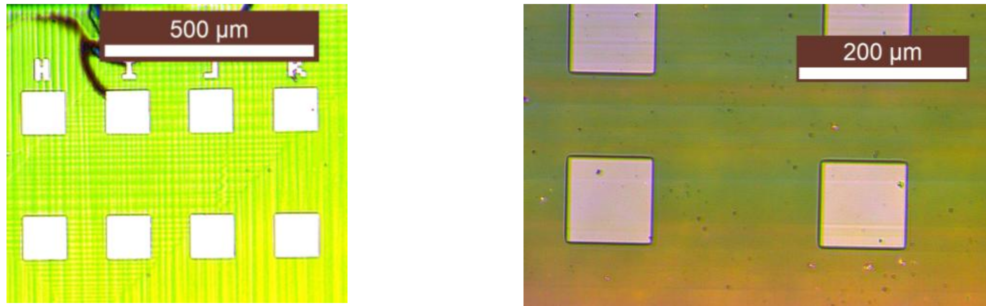

Fig. 2.17. Optical images of the photolithography processes preformed on two different LSMO samples.

2.6.2 Metal deposition through Physical Vapor Deposition (PVD) processes

Metal electrodes play an important role when evaluation of the electronic characteristics of the memristor devices for resistive switching applications is performed [31][32]. Recent studies have demonstrated diverse effects of the metal electrodes on the RS as the electrode material can participate in oxidation-reduction process [92], or in trapping and detrapping of the oxygen vacancies at the interface metal/oxide [93]. In this regard,

we have chosen three different metal electrodes: Au, Ag and Pt which are typically used to investigate the RS characteristics in other different metal oxides [91], [92], [94], [95]. In this work, these metals have been deposited by Physical Vapor Deposition (PVD) methods. PVD is an atomic deposition process in which material is vaporized from a solid or liquid source in the form of atoms or molecules and transported in the form of a vapor through a vacuum or plasma environment to the substrate, where it condenses. Two physical principles were used to do this: thermal evaporation and sputtering [96].

2.6.2.1 Metal thermal evaporation

In thermal evaporation, the metal source is placed in a container, called the crucible, and is heated up to melting temperature prior evaporation occurs. In order to ensure step coverage and minimize shadow effects during deposition, the sample is rotated or heated during the deposition [97]. Au and Ag metal were evaporated in an evaporation system Auto 306 from Boc Edwards at high vacuum ambient. This system applies a current passing through the metal in the crucible producing the evaporation of the metal. The control of the metal deposition rate is done by metal mass and post calibration. The deposition was carried out at typical values of current around 3A.

We have observed that, after metal deposition of Ag and Au when the lift-off is performed, metal layers are poorly attached and easily removed due to poor adhesion of the metal to the sample surface (fig 2.18a). In order to improve the adherence, a thin layer (5nm) of Cr or Ti was evaporated prior Ag or Au [98]. As a result, well defined metal electrodes were obtained, indicating that the Ag and Au evaporation has been improved (fig 2.18b).

a)

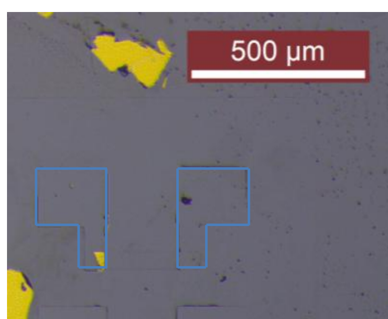

b)

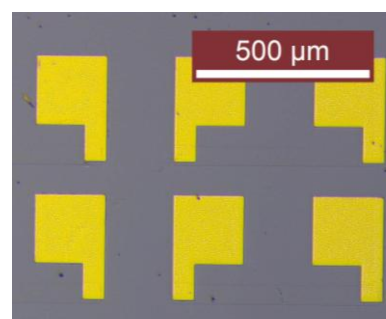

Fig. 2.18 Optical images of two different samples showing adhesion of metal layer after thermal evaporation. In a) metal was removed due to poor adhesion to the surface of LSMO. b) The adhesion was improved by evaporating a thin Cr or Ti layer prior to Au deposition in this case.

Moreover, a final thermal annealing needed to be performed in order to reduce the metal-oxide contact resistance which initially was ~24kΩ. Despite the LSMO layers are in the metallic state at room temperature, the contact resistance has to be maintained as low as possible. For this reason, the samples were placed in a tubular furnace in order to perform a post annealing thermal process at 450ºC for 60min in oxygen flux at 0.12 $l\cdot min^{-1}$. Figure 2.19a shows the thermal profile of the post annealing performed to the sample in order to reduce contact resistance which could be decreased down to ~4.5kΩ. The magnetization measurements performed to as grown LSMO layer and after the metal evaporation and post annealing shown in figure 2.19b. According to these measurements, the magnetization has decreased after the metal deposition and post annealing thermal treatment which indicates that the properties of the LSMO layer have been slightly modified.

a). **b)**

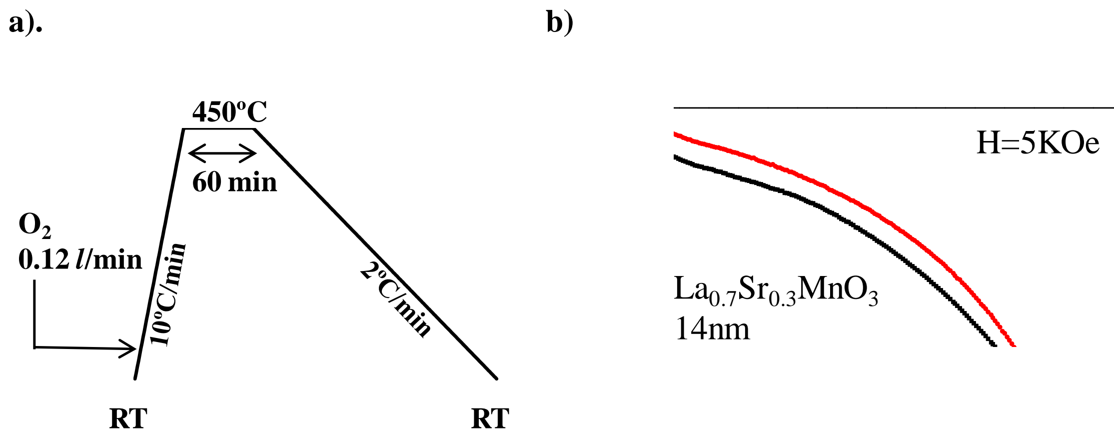

Fig. 2.19 a) Post annealing thermal profile performed to samples after metal evaporation, b) magnetization measurements performed to an as grown LSMO sample and after metal evaporation and post annealing.

Several attempts were evaluated changing the evaporation and post annealing conditions in order to optimize the process. However, in any case, the $La_{1-x}Sr_xMnO_3$ properties could be maintained and the resistive switching characteristics were not clearly observed.

2.6.2.2 Metal sputtering

In sputtering, a target of the metal to be deposited is bombarded with high-energy inert ions in plasma ambient. The outcome of the bombardment is that individual atoms or clusters are removed from the surface and ejected towards the sample. The inert ions

bombarding the target are produced in direct current plasma. In spite of the lower deposition rate, step coverage in sputtering is much better than in thermal evaporation [97]. A sputtering system from Twente Solid State Technology (TSST) is used to sputter Au, Ag and Pt metal electrodes on the same sample (fig. 2.20), using Ar to generate the ion plasma ambient. The patterned structures have 100x100μm^2 and they are separated from one to another 100μm. For each metal sputtering, the operation conditions are presented in table 2.3. In all cases, the sputtered metals present a very good adhesion to $La_{1-x}Sr_xMnO_3$ and CeO_{2-x} surfaces without the need to use an adhesive thin metal layer. In addition, the contact resistance has been demonstrated to be of low enough values without to perform any post annealing process. Typical values of contact resistance measured in metal sputtered samples are presented in the following sections.

Metal	Vacuum (mbar)	Ar flux (sscm)	Gas pressure (mbar)	Voltage (V)	Current (A)	Time (min)	Thickness (nm)
Pt	~10^{-6}	20	0.02	450	0.01	15	50
Ag	~10^{-6}	20	0.02	325	0.08	10	50
Ag*	~10^{-6}	20	0.05	425	0.09	5	50
Au	~10^{-6}	20	0.05	500	0.08	10	50

Table 2.3 Sputtering condition for three different metal electrodes

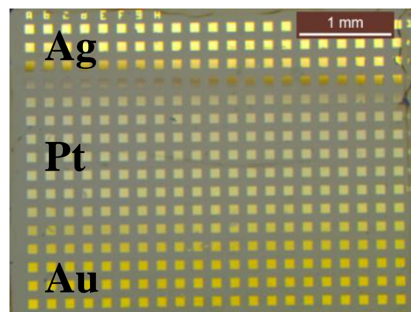

Fig. 2.20. Optical image of one LSMO sample where three different metals (Ag, Au and Pt) were sputtered.

Similar magnetization measurements were performed in order to investigate the properties of the LSMO layer. After the successive deposition of these three metal electrodes, magnetization has decreased as presented in figure 2.18a. This behavior could be explained by the continuous exposure of the LSMO layer to Ar ambient during sputtering, producing some important changes in the oxygen content in LSMO mainly associated to the creation of oxygen vacancies. On the other hand, sputtering of Ag* (table 2.3) was optimized by the members of the group at ICMAB, for other different

processes where oxygen plays an important role such as in superconductivity of $YBa_{0.2}Cu_{0.3}O_7$ (YBCO) layers. However, this optimization has been performed lately at the end of this work so that most of the samples used to induce the RS phenomena were not fabricated with this process. For this reason, some of the results are conditioned by the formation of oxygen vacancies in the LSMO layer due to metal electrodes sputtering.

Figure 2.18b shows that the magnetization measured in as grown LSMO layer is maintained after metal Ag* sputtering which indicates that the physical characteristics of the LSMO layer are not degraded after this process.

a) **b)**

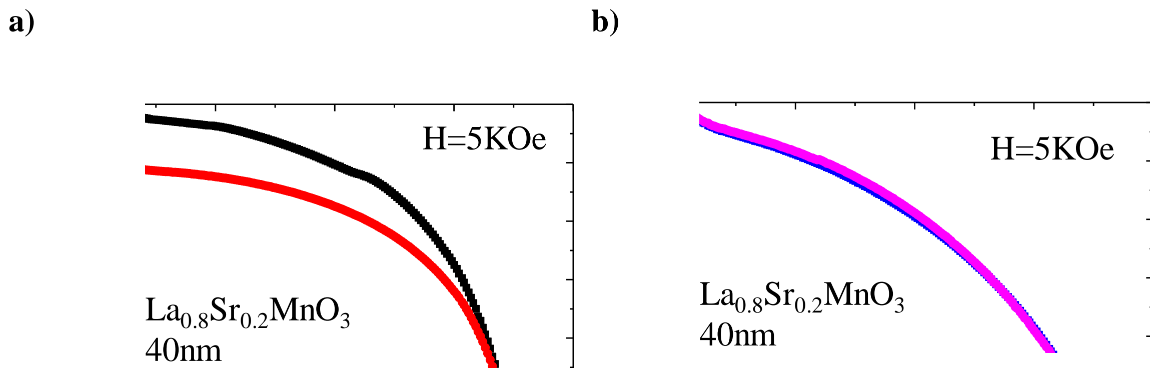

Fig. 2.18 Magnetization measurements performed to LSMO samples before and after metal sputtering. a) Shows a decrease of the magnetization after continued sputtering of the three metals and b) Optimization of the Ag sputtering indicate that LSMO properties are not modified after this process.

2.6.3 Oxide etching

Etching is used to remove material selectively in order to create patterns. The pattern is defined by the etching mask using photolithography, because the parts of the material, which should remain, are protected by the mask. The unmasked material can be removed either by wet (chemical) or dry (physical) etching [99]. Wet etching is strongly isotropic which limits its application and the etching time can be controlled difficultly. Because of the under-etch effect, wet etching is not suited to transfer patterns with sub-micron feature size. However, wet etching has a high selectivity (the etch rate strongly depends on the material) and it does not damage the material. On the other hand, dry

etching is highly anisotropic but less selective. Yet it is more capable for transferring small structures.

Test structures of LSMO layers to conduct resistivity and contact resistance measurements are defined by etching. Similar photolithography process described before is used to transfer the test structures patterns. After development, the selected areas are protected with photoresist while the unprotected ones will be removed by etching as indicated in figure 2.19. Finally, the photoresist is cleaned with acetone in ultrasound bath.

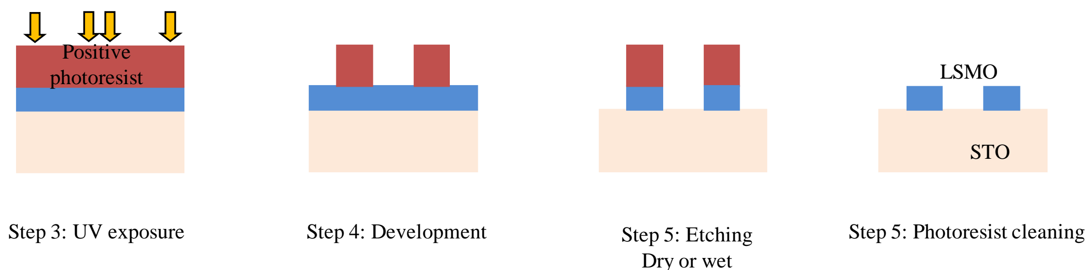

Fig. 2.19 Schematic of the etching process

Wet etching of LSMO layers is performed using a piranha acid solution. The wet etching process consists of the chemical attack in which the sample is immersed in 0.2% diluted piranha solution ($H_2SO_4 + H_2O_2 + H_2O$). As a result, the pattern is transferred to the LSMO. However, it is not possible to etch CeO_{2-x} layers with this solution.

On the other hand, in dry etching, also known as reactive ion etching (RIE), the sample is exposed to plasma, which is generated by a radio frequency electric field. The energetic species react chemically with the exposed regions of the material to be etched, while the ions in the plasma bombard the surface vertically and remove films from the sample surface. The latter action is directional which means that the etching is anisotropic. We have taken advantage of this phenomenon to etch the $La_{1-x}Sr_xMnO_3$ and CeO_{2-x} layers since it is not possible to produce any reaction owing to the fact that we use only Ar plasma during this process. Figure 2.20a shows a schematic of this dry etching process and fig 2.20b and 2.20c compare the optical images after wet and dry etching respectively.

a)

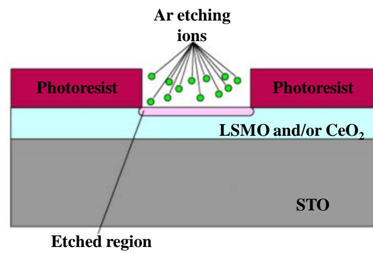

b) **c)**

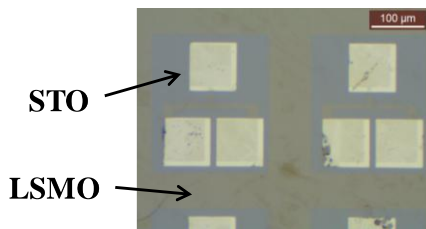

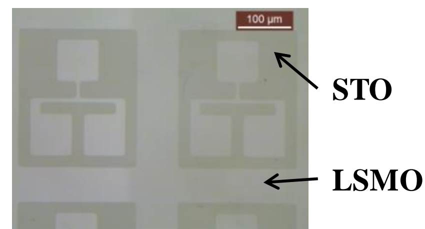

Fig 2.20 a) Schematic of the etching process used to remove LSMO and CeO_2 layers. Optical image of two different LSMO samples where b) wet etching and c) dry etching has been performed

RIE 2000 CEA from South Bay Technology is used to perform etching to LSMO and CeO_{2-x} layers in Ar ambient. The etching rate for these layers has been measured for different operation power as observed in figure 2.21. The Ar pressure inside of the chamber has been maintained constant at 100mTorr for the different etching processes. Figure 2.21a shows the etching rate of $La_{0.7}Sr_{0.3}MnO_3$ for three different operation powers. The etching rate increases while the power also increases; however, at short times, the etching of $La_{0.7}Sr_{0.3}MnO_3$ is observed to be abrupt when power is set at 100W and 120W. Figure 2.21b shows the etching rate for CeO_{2-x} layer for only two power operations. It is worth noting to say that properties degradation of samples was observed when the sample is maintained under Ar ambient at long time, typically above 10min, during etching process.

a) **b)**

Fig. 2.21 a) LSMO etching rate and b) CeO_{2-x} etching rate for different power operations in RIE

2.7 Resistivity and contact resistance measurements of devices

The resistivity at device stage of $La_{0.7}Sr_{0.3}MnO_3$ is measured after device fabrication through specific structures used in microelectronics to this purpose. An image of the so-called cross-bridge structure [100] is shown in figure 2.22; it consists of a long bridge with small contact arms separated at different distances. The evaluation of the resistivity is conducted through a modified 4-point probe measurement technique as indicated in the same schematic and described in detail in the appendix part of this thesis.

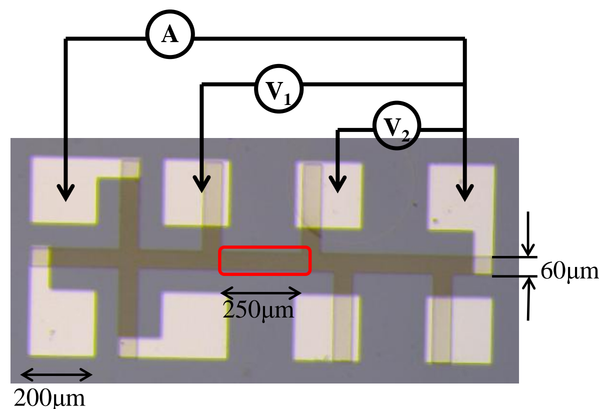

Fig. 2.22 Schematic of the cross-bridge structure used to perform resistivity measurements in a modified 4-probe technique.

From the part of the track marked inside of a red box in the figure, where the voltage drop V_1 and V_2 is measured, has a uniform cross section with a uniform flow of current between the two terminals. In this case, the electrical resistivity ρ is defined as [100]:

$$\rho = R\frac{W \cdot t}{L} \qquad (2.2)$$

Where R is the measured resistance; W is the width of the track; t is the LSMO thickness and L is the length of the bridge where the voltage drop is measured. The resistance is deduced from the slope of the voltage drop V_1 minus V_2. In this way, we are taking into account just the resistance across the length L of the track. Figure 2.23a shows a set of measured curves according to the modified 4-probe technique from which the resistance is calculated. Therefore, the resistivity is easily deduced from these measurements. A comparison between the Van der Pauw method performed to $La_{0.7}Sr_{0.3}MnO_3$ after growth and $La_{0.7}Sr_{0.3}MnO_3$ bridges after fabrication is shown in figure 2.23b. The resistivity measured by the four-probe method of ~4.6mΩ·cm is very much comparable to the measured by Van der Pauw of ~4mΩ·cm. The reported resistivity value of $La_{0.7}Sr_{0.3}MnO_3$ at room temperature is 0.84mΩ·cm [101] measured in thicker films.

a) **b)**

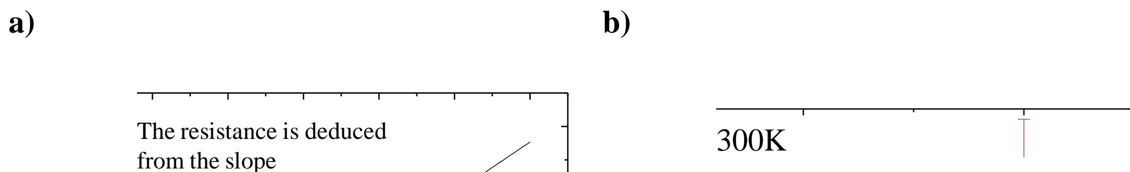

Fig. 2.23 a) I-V curves measured at the length L of the LSMO track from which resistance is deduced. b) Resistivity comparison between Van der Paw and modified 4-point probe method

When measuring resistance with the four-point probe or van der Pauw methods, 4 contacts have been used to determine the resistivity of the layer while minimizing the effects of contact resistance. It is useful to determine the contact resistance during the evaluation of the resistive switching characteristics in order to have some idea of how it may affect the memory performance. For this purpose, we have used two approaches in order to better compare results. The first one uses the same cross-bridge structures, described before, to perform two-point probe I-V measurements; and the second one

uses the transmission line method (TLM). An introduction for both methods is presented as it follows.

Consider the two-point probe arrangement of figure 2.24a. Each contact serves as a current and as a voltage probe. If we want to know the resistance of the device under test (DUT), we have to consider the total resistance R_T of the circuit which is given by [100]

$$R_T = {}^{V}/_{I} = 2R_W + 2R_C + R_{DUT} \tag{2.3}$$

R_W is the resistance of the wires/cables used to connect the DUT, R_C is the contact resistance and R_{DUT} the resistance of the device under test. Clearly, it is impossible to determine R_{DUT} with this measurement arrangement. The solution is the four-point probe method shown in figure 2.24b. The current path is identical in both cases; however, the voltage is now measured with two additional contacts. Although the voltage path contains R_W and R_C as well, the current flowing through the voltage path is very low due to the high input impedance of the voltmeter. As a result, the voltage drop across R_W and R_C are negligibly small and can be neglected as we did for resistivity measurements.

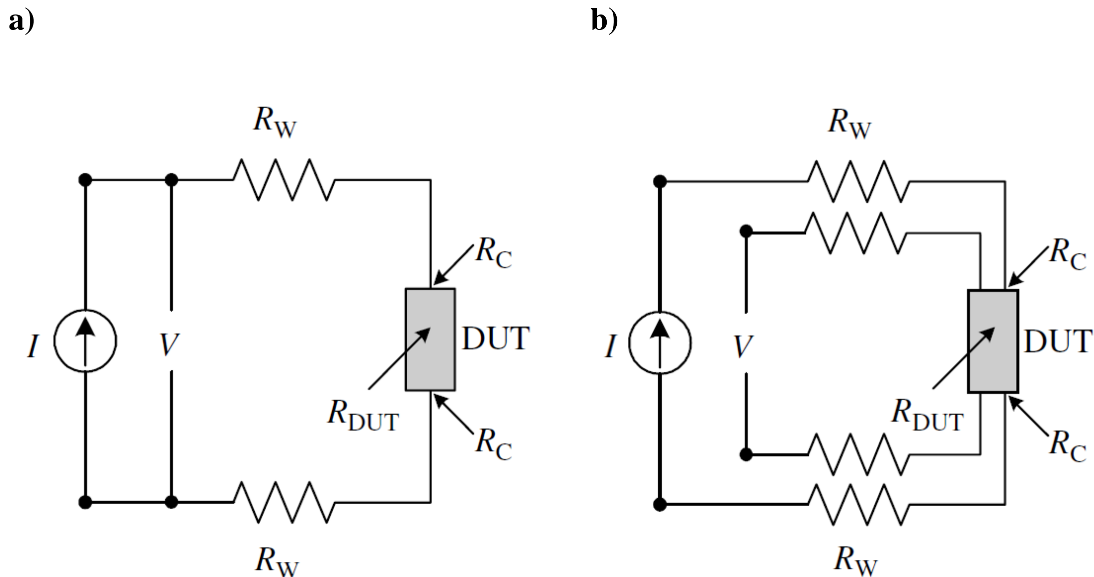

Fig. 2.24 a)Two terminal and b) four-terminal resistance measurements arrangements

Once the resistance of the LSMO track is known from the resistivity measurements, i.e. the R_{DUT}, a 2-point probe measurement is performed in the same LSMO track in order to obtain the R_{2point}. In this case, we have neglected the influence of the R_W and hence only the R_C is obtained from the difference of the resistances as it follows:

$$R_C = \frac{R_{2point} - R_{DUT}}{2} \tag{2.4}$$

It is worth noting that the contact resistance measurements were performed to the three different metal electrodes. In each case, the resistivity of the $La_{0.7}Sr_{0.3}MnO_3$ and the contact resistance were found to be slightly different for each case. However, these values give us a general idea of the influence of the metal-$La_{0.7}Sr_{0.3}MnO_3$ contact resistance in the resistive switching characteristics. Table 2.4 shows these results, comparing the contact resistance value, the Ag-$La_{0.7}Sr_{0.3}MnO_3$ contact demonstrate the lowest value of 350Ω.

metal	$La_{0.7}Sr_{0.3}MnO_3$ Resistivity (mΩ·cm)	R_{2point} (kΩ)	R_{DUT} (kΩ)	R_C (Ω)
Au	4.6	11.5	10.2	650
Ag	4.8	11.3	10.6	350
Pt	4.1	10.1	9.03	535

Table 2.4 Summary of resistivity and resistance values measured in order to calculate the contact resistance Rc. The lowest value was observed in Ag-LSMO metal electrodes

The $La_{0.7}Sr_{0.3}MnO_3$ resistivity values showed in the table 2.4 were obtained from the modified 4-point probe measurements using the same logic described before, taking into account the geometric parameters of the cross-bridge structures. These values are also in agreement with the values measured in the $La_{0.7}Sr_{0.3}MnO_3$ layers using the Van der Pauw method.

The second method that we have used to measure the R_C is the Transmission Line Method (TLM). The first step is to deposit the metal and pattern it so that they have identical pads spaced varying distances apart. All the pads in any one row must be the same size, and the distances between pads must vary. The implementation of this method is displayed in figure 2.25 and it is explained in detail in the appendix part.

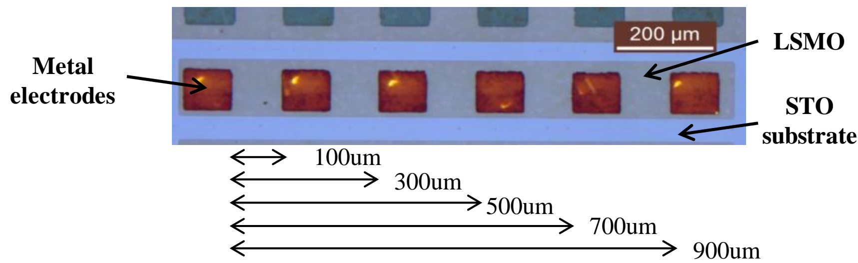

Fig. 2.25. Implementation of the Transmission Line Method (TLM) to measure the contact resistance R_C.

The measurements required are simple I-V curves, from where the resistance is calculated between two pads. The total resistance is the series combination of 3 resistors: metal- $La_{0.7}Sr_{0.3}MnO_3$ junction, through the $La_{0.7}Sr_{0.3}MnO_3$ layer, and back into metal-$La_{0.7}Sr_{0.3}MnO_3$ junction. In the limit where the distance between the pads approaches 0, resistance of the $La_{0.7}Sr_{0.3}MnO_3$ goes to 0 and what is left is $2R_C$. Figure 2.26 shows the curves with the extrapolation of the resistance to 0 where the $2R_C$ is obtained.

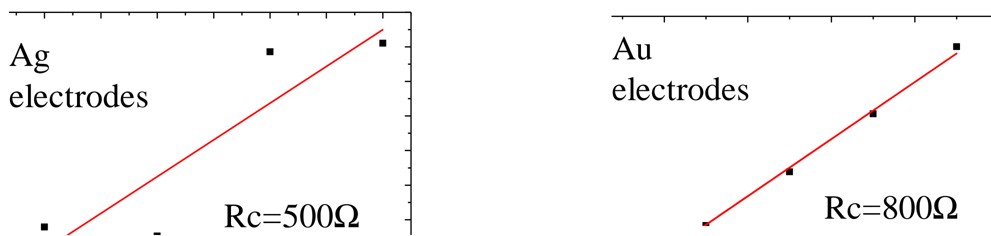

Fig. 2.26 Contact resistance R_C values obtained by the transmission line method for a) Ag electrodes and b) Au electrodes

These R_C values are slightly higher compared with those measured with cross-bridge structures. However, the lowest resistance was found in Ag-$La_{0.7}Sr_{0.3}MnO_3$ contact which is agreement with the result showed before.

2.8 Conclusions about layers deposition and device microfabrication

In this chapter, the $La_{1-x}Sr_xMnO_3$ and CeO_{2-x} layer growth methods have been presented. It has been demonstrated that the Chemical Solution Deposition method is suitable to obtain high-quality thin $La_{1-x}Sr_xMnO_3$ epitaxial layers. In addition, CSD and

ALD are compatible techniques which can be used together to deposit thin layers without any properties degradation.

The structural and physical properties of deposited layers have been investigated by using different characterization techniques such as AFM, XDR, magnetization and transport measurements. Moreover, the differences in the physical properties where determined among $La_{1-x}Sr_xMnO_3$ layers when Sr content was modified. These layers are suitable to study the resistive switching behavior due to their excellent physical properties.

In addition, microfabrication processes has been conducted in order to obtain the devices where resistive switching will be evaluated. Photolithography, etching and metal deposition have been used to achieve this purpose. Optimization of the fabrication process after each step has been conducted in order to minimize the modification of the $La_{1-x}Sr_xMnO_3$ properties and be able to correlate the initial layer properties to resistive switching characteristics. However, in some of the layers studied in the next chapters we cannot discard non-stoichiometric oxygen content of the layers. In general, we should assume ionic structure like $La^{3+}_{1-x}Sr^{2+}_{x}Mn^{3+}_{1-x+2y}Mn^{4+}_{x-2y}O^{2-}_{3-y}V^{0}_{y}$ where V^0 represents the formation of oxygen vacancies.

Finally, device resistivity and contact resistance measurements have been conducted in order to evaluate the actual initial state of our devices. We demonstrated that these parameters depend on the fabrication conditions which have been optimized as well.

Chapter 3

Resistive Switching evaluation in $La_{1-x}Sr_xMnO_3$ layers and $CeO_{2-x}/La_{1-x}Sr_xMnO_3$ bilayers memristor-like devices

In this chapter, we will present the results of the evaluation of resistive switching in $La_{1-x}Sr_xMnO_3$ layer and $CeO_{2-x}/La_{1-x}Sr_xMnO_3$ bilayer memristor-like devices. In addition, a model of the mechanism producing the resistive switching will be proposed.

Right after the observation of resistance change effect induced by electric pulses in $Pr_{0.7}Ca_{0.3}MnO_3$ (PCMO) films [102], perovskite manganite materials attracted considerable attention. In this regard, electric-induced resistive switching has been reported in $La_{1-x}Sr_xMnO_3$ films [22], [103]. Different from PCMO which is in the insulating-paramagnetic phase at room temperature, crystalline $La_{1-x}Sr_xMnO_3$ is a robust ferromagnetic metal at 300K.

Most of the previous works, where resistive switching in $La_{0.7}Sr_{0.3}MnO_3$ has been reported, give a description of the switching mechanism based on the creation and recombination of oxygen vacancies inside the layer [9], [104]. In addition, volume switching has been demonstrated in bulk $La_{0.7}Sr_{0.3}MnO_3$ layers when local resistance changes are induced through a C-SFM approach [9]. Taking advantage of these properties, we want to demonstrate that the bulk resistive switching phenomena can be induced at device level using micrometric probes. Consequently, the application of $La_{1-x}Sr_xMnO_3$ as an oxide to induce resistive switching would be confirmed as an interesting candidate for non-volatile memory devices.

In this work, the I-V characteristics of each memristor device were investigated by applying systematic voltage sweep loops ($0 \rightarrow +V_{max} \rightarrow 0 \rightarrow -V_{max} \rightarrow 0$) using a Keithley 4200-Semiconductor Characterization System and an Agilent 4156C Semiconductor Parameter Analyzer. All these measurements were performed at room temperature using W-Au probes to contact the micro-devices.

3.1 Bipolar Resistive switching in $La_{08}Sr_{0.2}MnO_3$ devices

The resistivity measurements, presented in the last chapter, performed to $La_{1-x}Sr_xMnO_3$ with different stoichiometries indicate that the metal-insulator transition (MIT) for x=0.2 is close to room temperature (300K). For this reason, our first step has been the evaluation of RS in $La_{0.8}Sr_{0.2}MnO_3$ films. Three different metals electrodes (Ag, Au and Pt) were sputtered to form metal/$La_{0.8}Sr_{0.2}MnO_3$/metal lateral devices. The probes are placed on top of metal electrodes and voltage is applied until ±30V as described before. However, only the metallic state is measured and no remarkable RS has been induced for any device as can be seen in fig. 3.1.

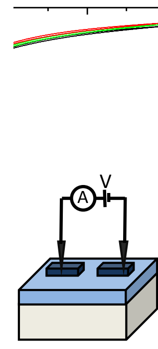

Fig. 3.1. I-V curves for the three different metal electrodes with $La_{0.8}Sr_{0.2}MnO_3$ lateral devices. No RS has been induced with voltage sweep up to ±30V

The metallic state of the $La_{0.8}Sr_{0.2}MnO_3$ layer is measured when probes are located on metal electrodes. This behavior can be explained taking into account oxygen ion migration which has been already proposed as the mechanisme to drive resistive switching in $La_{0.7}Sr_{0.3}MnO_3$ [9]. The metal electrodes act as a barrier and they do not allow oxygen interchange with the ambient. This mechanism will be presented in more detail in the following sections.

These results are different when compared with other reports where resistive switching in amorphous $La_{0.7}Sr_{0.3}MnO_3$ has shown to display a dependence with the metal used as electrode. For instance, the resistive switching behavior is attributted to an electrochemical migration of Ag ions into the $La_{0.7}Sr_{0.3}MnO_3$ to form a conductive path or the variation of the Schottky-like barrier height formed at the metal/$La_{0.7}Sr_{0.3}MnO_3$ interface [104],[105] which is not the case of our devices.

Different results were obtained when probes were located directly in contact to the metallic $La_{0.8}Sr_{0.2}MnO_3$ layer as observed in fig. 3.2. In this figure, bipolar resistive switching is plotted in a) linear and b) semi-log scales. At the lateral probe/$La_{0.8}Sr_{0.2}MnO_3$/probe device, the initial Low Resistance State (LRS) is changed to a High Resistance State (HRS) applying positive sweep voltage while negative sweep voltage is needed to return to the initial LRS. At positive small voltages, the current increases until a steady transition from LRS to HRS, called *Reset* process, is reached (branch 1). Then, the current remains in the HRS during the voltage back excursion (branch 2). At negative voltages, the current stays at small values until a sharp increase is observed around -5V (branch 3). At this *Set* voltage, the initial LRS is restored and maintained during the voltage back excursion where the initial current conduction is observed again (branch 4). As a result, Bipolar Resistive Switching (BRS) is demonstrated in $La_{0.8}Sr_{0.2}MnO_3$-based devices. It is noteworthy that the first initial transition in $La_{0.8}Sr_{0.2}MnO_3$ memristor devices is produced from LRS to HRS due to the metallic state of the layer at room temperature. In addition, the BRS is achieved without any previous electroforming process, indicating that no dielectric breakdown or conductive filament formation does not occur in the bulk oxide.

The *Set* and *Reset* are commonly used names when referring to transitions in the resistive switching phenomena. The nomenclature, widely used for insulating films in the pristine state, is a Set when they change from HRS to LRS and Reset in the opposite transition. For this reason, even if the first transition in metallic $La_{1-x}Sr_xMnO_3$ layers takes place from LRS to HRS, we have decided to keep the same nomenclature.

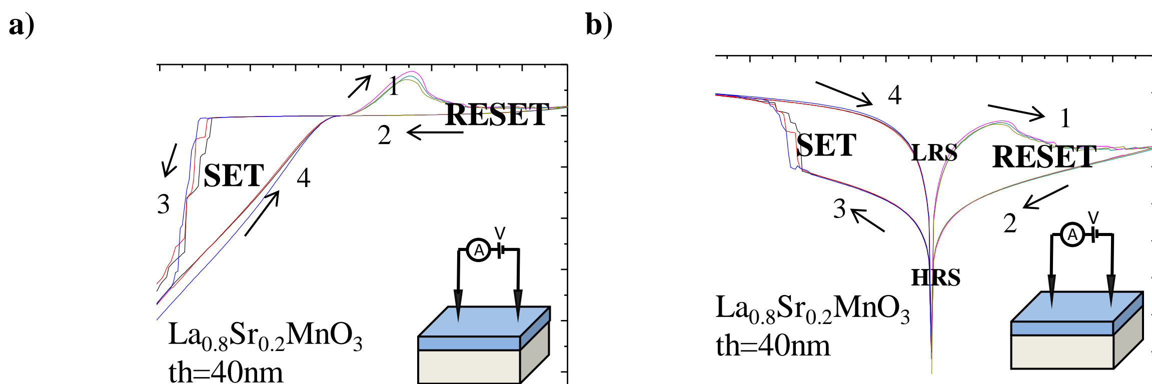

Fig. 3.2. Bipolar Resisitve Switching (BRS) observed in $La_{0.8}Sr_{0.2}MnO_3$. a) Linear scale and b)semi-log scale for the same measured curves. The transition from HRS to LSR is called Reset while Set is produced from HRS to LRS.

Consecutive voltage sweep loops were applied to a single device in order to measure the repeatability of resistive switching. In spite of small changes in the *Set* and *Reset* voltage, eventually measured from one cycle to another, any modification of the transition polarity has been observed (fig. 3.3a), which confirms the robustness of these devices. The measurements, conducted when probes are placed directly on $La_{0.8}Sr_{0.2}MnO_3$ layer, confirm BRS at least up to 100 Set/Reset cycles. Large resistance ratio (R_H/R_L) of the order of 10^2-10^3 can be observed when the resistance is plotted as a function the cycle number (fig. 3.3b). In this case, the read voltage was set to -1V.

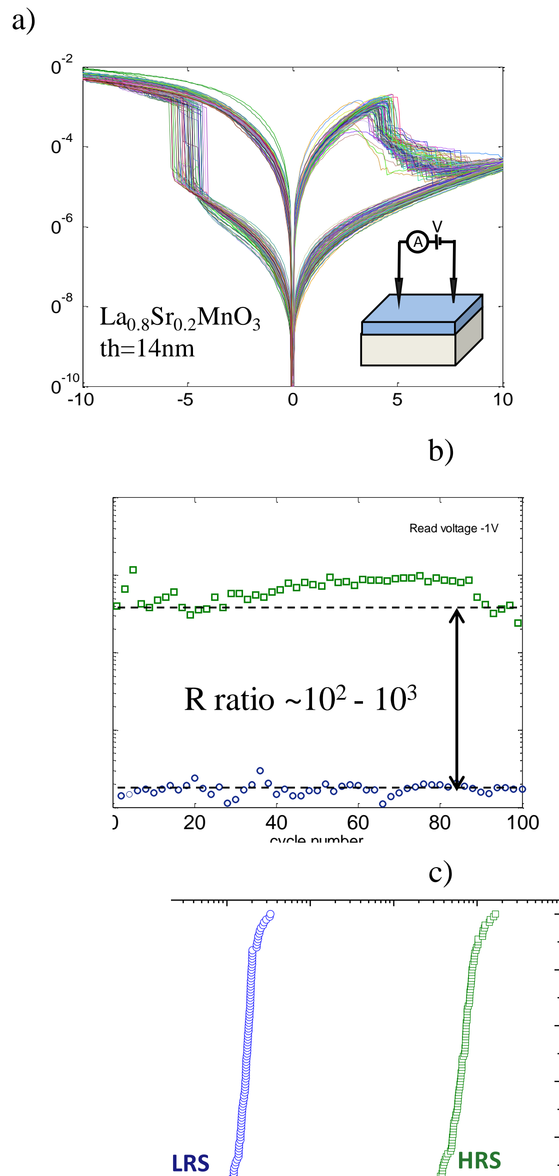

Fig 3.3 Repeatability test performed when probes are placed on top of LSMO. a) 100 cycles applied on the same memristor device. b) The resistance ratio is in the order of 10^2 - 10^3 at read voltage of -1V. c) Statistical distribution of the resistance in the LRS and HRS.

The cumulative distribution for the two different resistance staes is showed in figure 3.3c. In this curve, both the LRS and the HRS are clearly separated and the resistance ratio of 10^2-10^3 indicates that these two states can be used to robustly represent the two different memory states.

Therefore, BRS has been demonstrated in $La_{0.8}Sr_{0.2}MnO_3$ at micrometric scale only when probes are located on top of the $La_{0.8}Sr_{0.2}MnO_3$ layer. The repeatability test shows good resistance ratios for at least 100 Set/Reset consecutive cycles.

3.1.2 Oxygen ion migration as the mechanism for BRS in $La_{1-x}Sr_xMnO_3$

The oxygen ion (O^{2-}) migration through a MIT transition has been proposed as the mechanism to describe the resistive switching phenomena observed in $La_{0.7}Sr_{0.3}MnO_3$ layers [9], [106]. It has been reported that small changes in oxygen concentration in colossal magnetoresistance (CMR) materials results in large resistance changes [43], [107]–[109]. In addition, charge current injection of electrons can cause oxygen migration in perovskite oxides [83], [110]. The oxygen stoichiometry change, induced by electric field, is not only distributed at the interface region but within the bulk material. In particular, phase separation and phase transitions are known to exist in perovskites after application of electric field leading a modification of the topography and demonstrating hysteresis and memory effects [9], [111]

Regarding metal/$La_{1-x}Sr_xMnO_3$/metal memristor devices, when a sufficient high positive electric field is applied to one of the metal electrodes, the oxygen anions accumulate at the metal/$La_{1-x}Sr_xMnO_3$ interface. The metal electrodes act as a barrier for these oxygen ions, which does not allow exchange with the ambient and only redistribution within the $La_{1-x}Sr_xMnO_3$ layer is possible. Consequently, a remarkable RS effect is not achieved.

On the other hand, BRS is achieved when probes are located directly on $La_{1-x}Sr_xMnO_3$ layer. The positive electric field applied to one probe, which now acts as electrode, produces a Reset in $La_{1-x}Sr_xMnO_3$. In this case, the oxygen anions from the $La_{1-x}Sr_xMnO_3$ layer migrate to the probe/$La_{1-x}Sr_xMnO_3$ interface where they are exchanged with the ambient enabling the RS in $La_{1-x}Sr_xMnO_3$. A schematic of the oxygen ion migration from $La_{1-x}Sr_xMnO_3$ layer is presented in figure 3.4a. A comparison between the measurements performed on metal/$La_{1-x}Sr_xMnO_3$/metal and probe/La_{1-x}

Sr_xMnO_3/probe devices is presented in figure 3.4b. The current measured when probes are placed on the metal electrodes and when they are on the $La_{1-x}Sr_xMnO_3$ layers has different magnitude. This could be attributed to the lower quality of the probe/$La_{1-x}Sr_xMnO_3$ contact (probes are just placed on top of the $La_{1-x}Sr_xMnO_3$ layer manually) which has been associated to a much higher contact resistance.

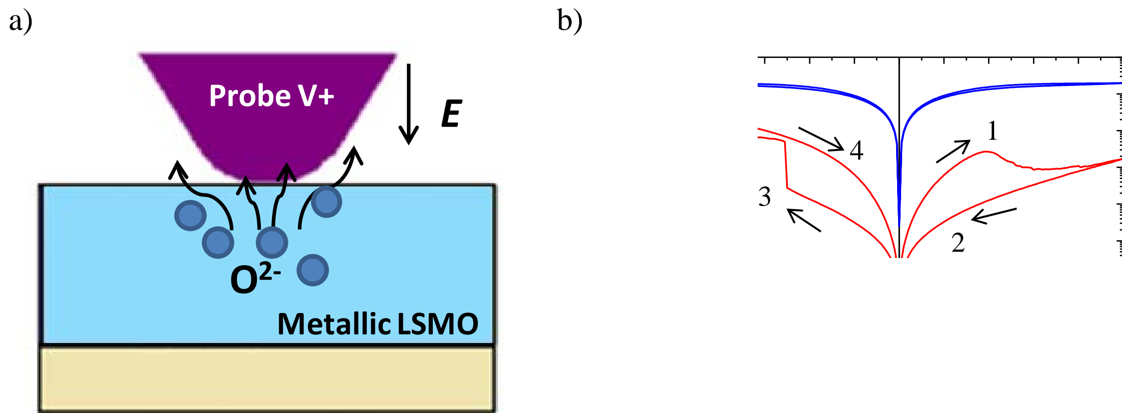

Fig 3.4 a) Schematic representing the oxygen exchange between the layer and the ambient. b) Curves measured when probes are located on metal electrodes (blue line) and when they are located directly on $La_{1-x}Sr_xMnO_3$ layer (red line).

Moreover, the lateral probe/$La_{1-x}Sr_xMnO_3$/probe configuration is a completely symmetric structure. For this reason, the direction of the applied electric field determines the polarity of the first resistive switching transition. There is only one electric polarization in which the oxygen ions can migrate outside from the $La_{1-x}Sr_xMnO_3$ layer according with the direction of the electric field. We can observe in figure 3.5, where the first voltage sweep is applied from 0 to $-V_{max}$, that the Reset transition is produced in the negative voltage sweep and thus the set/reset polarity transition is inverted.

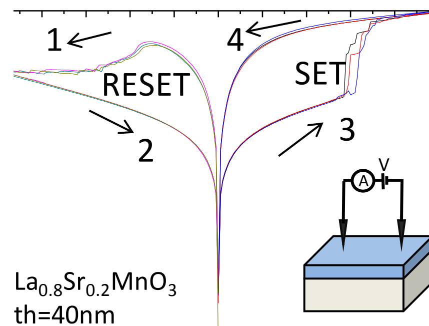

Fig. 3.5. The first negative voltage sweep induces an inversion of the BRS in the symmetric probe/$La_{0.8}Sr_{0.2}MnO_3$/probe lateral devices.

In order to better clarify this polarity effect, we make use of what we have learned from the use of the metal electrodes. During the resistive switching evaluation, one of the measurement probes is placed on top of the metal electrode meanwhile the other one is placed directly on the $La_{0.8}Sr_{0.2}MnO_3$ layer. The positive bias is defined by the current flowing from the metal electrode to the probe in contact with the $La_{0.8}Sr_{0.2}MnO_3$ layer, and the negative bias is defined in the opposite direction. The first positive voltage sweep does not induce any RS effect due to the fact that the oxygen ions are blocked by the metal electrode (branch 1-2 figure 3.6). In contrast, the negative voltage sweep induces a change from LRS to a HRS which is a consequence of the oxygen ions exchange (branch 3). From this point, the BRS behavior is observed for subsequent voltage sweeps.

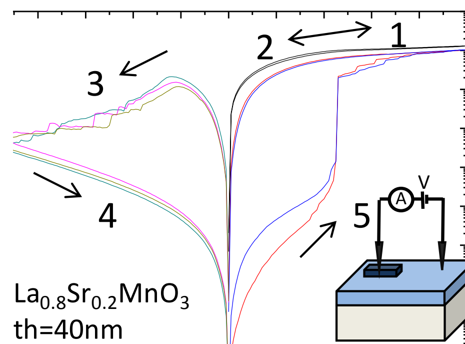

Figure 3.6. The positive measurement probe is placed on top of the metal electrode meanwhile the negative one is placed on the $La_{0.8}Sr_{0.2}MnO_3$ layer. The first positive voltage sweep does not induce any RS effect due to the fact that the oxygen ions are blocked by the electrode. In contrast, the negative voltage sweep induces a change from LRS to a HRS which is a consequence of the oxygen ions exchange.

From a circuit point of view, the probe/$La_{0.8}Sr_{0.2}MnO_3$/probe memristor device can be seen as a two resistances connected in series representing both sides of the $La_{0.8}Sr_{0.2}MnO_3$ layer under the measurement probes. Taking into account two important statements, the demonstration of the BRS happening under one single measurement probe is presented as follows:

- There is only one polarization in which the electric field favors the migration of oxygen ions outside the $La_{0.8}Sr_{0.2}MnO_3$ layer. Considering an as fabricated device as observed in figure 3.7, when a positive voltage is applied on a measurement probe A, the negative charged oxygen ions are attracted to the probe-LSMO interface where they are exchanged with the ambient resulting in a

transition from LRS to HRS. On the other hand, in the measurement probe B, the direction of the electric field produces a movement of the negatively charged ions to the substrate-$La_{0.8}Sr_{0.2}MnO_3$ interface. However, since the oxygen cannot be exchanged with the substrate any transition is observed under this electrode.

- When the transition from LRS to HRS takes place under probe A, the voltage drop in this area is higher compared to the voltage drop in area under probe B which remains in LRS. For this reason, although the electric field polarization favors the oxygen migration outside under probe B, its intensity is not enough to produce the transition. However, in the area under probe A, the transition from HRS to LRS is achieved.

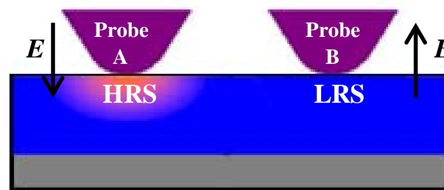

Fig. 3.7. The resistive switching transition studied in a lateral device. The direction and intensity of the applied electric field determines the region under the measurement probe where the transition takes place.

Providing that the resistive switching operation described before is repeated over several cycles, the resistive switching happening under one probe will follow the evolution presented in table 3.1.

	Region under probe A	Region under probe B
Initial state	LRS	LRS
0→Vmax	HRS	LRS
0→-Vmax	LRS	LRS
0→Vmax	HRS	LRS
0→-Vmax	LRS	LRS

Table 3.1.Evolution of the BRS induced in lateral devices under the two measurement probes. The transitions are enabled under only one probe.

The BRS has been described from the oxygen ion movement mechanism point of view. It has been demonstrated that the first voltage sweep performed not only determines the polarity of the transition but also probe/$La_{0.8}Sr_{0.2}MnO_3$ where the transition will take place during the whole RS experiment. Finally, it was demonstrated that the metal electrode annihilates the resistive switching effect due to the fact that the oxygen ion movement is blocked by the electrode; meanwhile the probes directly placed on the

$La_{0.8}Sr_{0.2}MnO_3$ film allow the oxygen exchange with the ambient favoring the resistive switching effect.

3.1.3 Influence of the $La_{0.8}Sr_{0.2}MnO_3$ thickness in the device operation

The properties of $La_{1-x}Sr_xMnO_3$ have been reported to display some changes when decreasing the layer thickness. In heteroepitaxial growth, a lattice mismatch exist between the deposited material and the susbtrate. The first layers at the film-substrate interface are strained. When increasing film thickness, the strain relaxes and the film properties approach to those of bulk. Consequently, there is a limit below which the material properties are dramatically changed. For instance, Boschker *et al.* [112] reported the insulating state without metal-insulator transition of $La_{2/3}Sr_{1/3}MnO_3$ layers when their thickness was below 10 unit cells. They attributed this behavior to the oxygen octahedral rotation pattern in thin films. In the past years, several papers concerning strain effects in $La_{0.7}Sr_{0.3}MnO_3$ layers have been published regarding degradation of Curie temperature (Tc) and resistivity (ρ) [46], [74], [113], [114].

In this work, the influence of the $La_{1-x}Sr_xMnO_3$ thickness has been first studied from the statistical point of view in the variability of the Vset and Vreset. As mentioned before, when several voltage cycles are applied on one single device, the value of set voltage (Vset) and reset voltage (Vreset) is shifted from one cycle to another. This cycle-to-cycle variability is a problem which negatively affects the application of RRAM and need to be improved by processing or by operation algorithms [115]. Moreover, it is important to determine their distribution in order to prevent misfunctionalities and assure reliability when the device is under programmation. Here, the distribution studies have been carried out in two different $La_{0.8}Sr_{0.2}MnO_3$ samples with 40nm and 14nm in thickness for comparison reasons.

The Vreset is defined as the voltage value where the current starts decreasing even when the voltage is increasing, leading a change forn LRS to HRS. On the other hand, the Vset is the voltage value where the current sharply increases producing a change from HRS to LRS. The Vset and Vreset are defined in figure 3.8. The difference between progressive Reset and sharp Set transitions might be attributed to the oxygen ion mechanism owing to the fact that some important parameters such as oxygen diffusion and distribution of the electric field at different regions of the $La_{1-x}Sr_xMnO_3$ layer

should be taking into account. However, this study is beyond the objectives of this thesis.

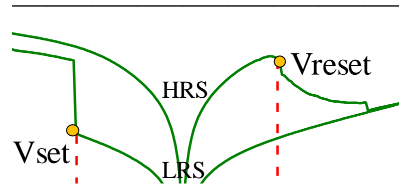

Fig 3.8. Vset and Vreset definiton from a bipolar resistive switching curve

In the case of Bipolar Resistive Switching, the Set/Reset processes could happen in opposite polarity bias.. However, the Vset and Vreset are always defined from the transition point of view and no matter the polarity they occur.

First, several voltage loops were applied to $La_{0.8}Sr_{0.2}MnO_3$when the measurements probes were placed on top of the layer. Figure 3.9a shows BRS cycles measured on $La_{0.8}Sr_{0.2}MnO_3$ with 40nm in thickness while figure 3.9b shows cycles for $La_{0.8}Sr_{0.2}MnO_3$ 14nm. Although different resistance values are observed after several cycles, the memristors mantain their switching behavior.

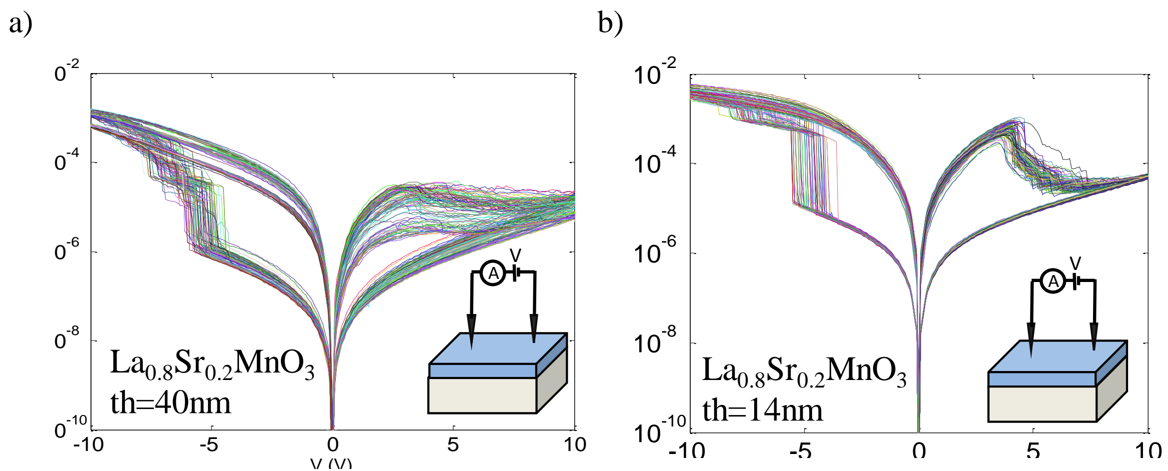

Fig. 3.9. Bipolar Resistive Switching induced in single memristor devices with $La_{0.8}Sr_{0.2}MnO_3$ in order to obtain a distribution of the Vset and Vrest. a) LSMO 40nm and b) LSMO 14nm.

From the curves in figure 3.9 we can observe that that current in the LRS is smaller in device with $La_{0.8}Sr_{0.2}MnO_3$ 40nm than in $La_{0.8}Sr_{0.2}MnO_3$ 14 nm. This effect can be attributed to higher probe/$La_{0.8}Sr_{0.2}MnO_3$ contact resistance. In addition, the Reset

transitions are clearly different for both devices. From one hand, a smooth steady Reset transition is observed in the device of $La_{0.8}Sr_{0.2}MnO_3$ 40 nm while a more abrupt Reset is observed in the device of LSMO 14nm. As expalined before, the mechanism of oxygen ion interchange could be responsible for this behavior. On the other hand, the Set transition in both devices is observed to be a sharp increase of the measured current.

Figure 3.10 compares the Vset and Vreset for the two different $La_{0.8}Sr_{0.2}MnO_3$ thicknesses analyzed in this section. A small decrease of the Vset and Vreset is observed for thinner $La_{0.8}Sr_{0.2}MnO_3$ layer. However, due to the fact that the influence of external effects such as the contact resistance and hence the electric field neccesary to induce the transitions, these results are only an orientation to show that the voltage needed to induce the transitions has decreased for thinner $La_{0.8}Sr_{0.2}MnO_3$ devices. Therefore, this give us the idea that $La_{1-x}Sr_xMnO_3$ thickness can be a parameter to tune the RS properties in $La_{1-x}Sr_xMnO_3$-based devices.

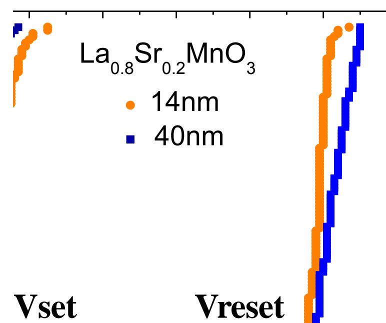

Fig. 3.10 Decrease in the Vset and Vreset is observed for memristors with thinner $La_{0.8}Sr_{0.2}MnO_3$ layer indicating that the thickness can be a parameter to tune the voltage operation of the memory device.

Moreover, different resistance states are reached by controlling the magnitude of the applied voltage $\pm V_{max}$ during the voltage sweep excursions. As mentioned before, the resistive switching takes place vertically along the thickness of the $La_{0.8}Sr_{0.2}MnO_3$ under the measurement probe. The non-volatility of the system is confirmed by applying consecutive sweeps since the measured current has the same magnitude of the previous sweep. As a result, multilevel switching has been demonstrated when probes were directly placed on metallic $La_{0.8}Sr_{0.2}MnO_3$. The voltage excursions show similar current conduction when a complete voltage cycle is performed (figure 3.11). Due to the fact that the *Reset* process shows a steady transition, different resistance levels are progressively achieved by controlling the final voltage during the voltage sweep.

Moreover, applying the same methodology with reverse bias, different resistance levels are also achieved. Since the *Set* process involves a sharp transition, the control of the resistance state is more difficult and fewer resistance levels could be obtained during this process. These results demonstrate that the applied voltage and the thickness are important parameters which need to be tuned to induce the resistive switching effect in the whole thickness of the $La_{0.8}Sr_{0.2}MnO_3$ layer.

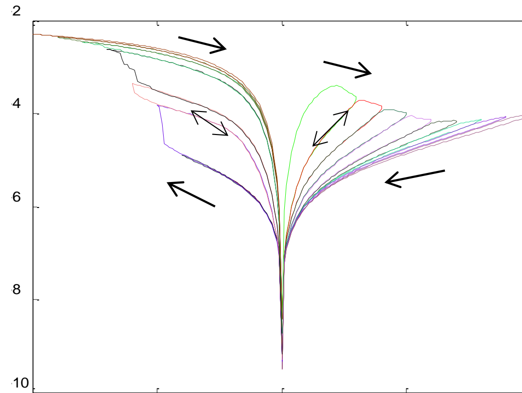

Fig. 3.11. Multilevel resistance achieved by applying consecutive sweep voltages in LSMO devices.

3.1.4 Resistive Switching evaluation in $La_{1-x}Sr_xMnO_3$ with different stoichiometry

The analysis of the physical properties with different stoichiometry x in $La_{1-x}Sr_xMnO_3$ has been already showed in Chapter 2. In this section, the BRS behavior in $La_{1-x}Sr_xMnO_3$ devices with x=0.15,0.25 and 0.3 is presented. The results can be understood in terms of the same oxygen ion exchange mechanism.

The electrical and magnetic properties of perovskite $La_{1-x}Sr_xMnO_3$ manganite can be modified by chemical doping of divalent cation by substitution of La^{3+} by Sr^{2+} and the conversion of Mn valence state from Mn^{3+} to Mn^{4+} [109]. In addition, this chemical doping can induce strain effects which can modify the microstructure giving rise to a change in the $La_{1-x}Sr_xMnO_3$ properties. Regarding the evaluation of resistive switching in $La_{1-x}Sr_xMnO_3$, recent studies have demonstrated that different Sr doping concentrations deeply modify the resistive switching characteristics. In their work, Choi *et al.* [22] used polycrystalline $La_{1-x}Sr_xMnO_3$ with doping concentration from 0.1 to 0.3. They correlated the observed RS characterisitcs to modifications in the growth orientation of $La_{1-x}Sr_xMnO_3$ on top of $Al/Ti/SiO_2/Si$ susbtrate. Since we are using

crystalline $La_{1-x}Sr_xMnO_3$ layers to evaluate the resistive switching, our results are not detrmined by different crystall orientation.

Figure 3.12 shows different curves measured in devices with different Sr content (x=0.3, 0.25 and 0.15) when probes are placed on metal electrodes. The metallic state is only measured and no remarkable RS is observed which is in agreement with our previous results observed in devices with $La_{0.8}Sr_{0.2}MnO_3$ showed in figure 3.1.

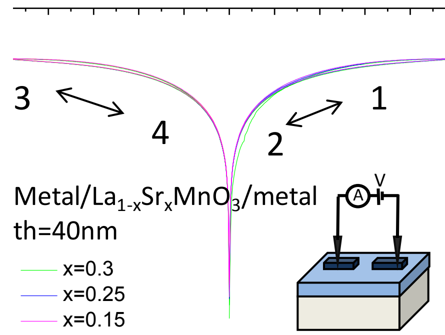

Fig. 3.12. The metallic state of different $La_{1-x}Sr_xMnO_3$ stoichiometries is measured when probes are located on metal electrodes in metal/$La_{1-x}Sr_xMnO_3$/metal devices

Regarding $La_{1-x}Sr_xMnO_3$ x=0.3, neither resistive switching effect could be induced even when probes are placed directly on LSMO layer and high voltage sweeps up to ±40V were applied (fig. 3.13a). However, the same sample was analyzed using C-SPM. The voltage was applied through a micrometric wire attached to the sample surface meanwhile the nanometric tip was grounded. In this case, BRS was induced (fig. 3.13b) at smaller voltage sweeps with similar resistance ratios as reproduced from the results of Moreno *et al*. [9]. The small Vset and Vreset indicate that the intensity of the electric field applied through the C-SPM tip on the $La_{1-x}Sr_xMnO_3$ sample, is better distributed and can enhance the migration of the oxygen ions in and out of the $La_{1-x}Sr_xMnO_3$ layer.

Different results were obtained for samples with Sr content x=0.25 and 0.15, as observed in figure 3.13c and 3.13d respectively, where the resistive switching is achieved when the measurement probes are located directly on top of the $La_{1-x}Sr_xMnO_3$ layer.

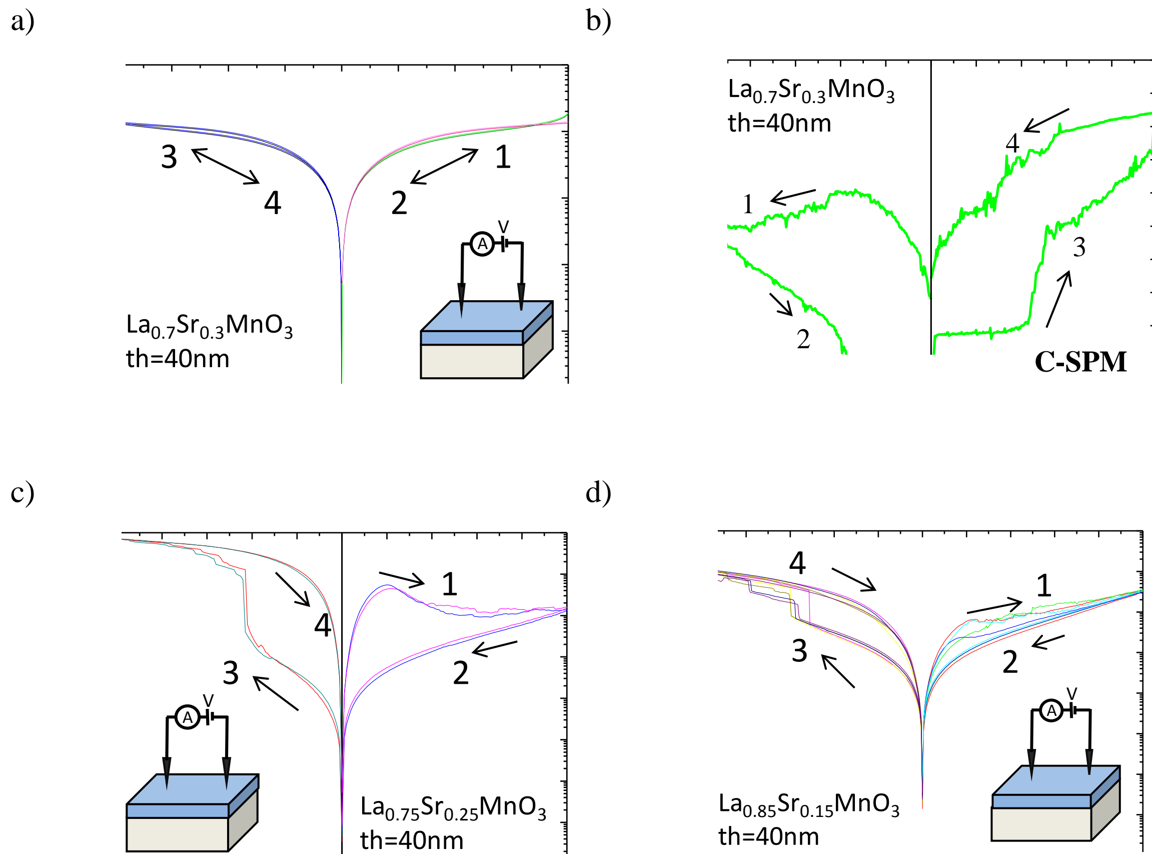

Fig. 3.13. a) BRS could not be induced in $La_{0.7}Sr_{0.3}MnO_3$ whit high voltage sweep using micrometric probes. b) BRS induced using C-SPM courtesy of J.C. Gonzalez. BRS observed in c) $La_{0.75}Sr_{0.25}MnO_3$ and d) $La_{0.85}Sr_{0.15}MnO_3$

Although BRS is clearly observed for $La_{1-x}Sr_xMnO_3$ x=015 and 0.25, there are some difference in the resistance ratio characteristics. As demonstrated before, the resistance ratio in devices with $La_{0.8}Sr_{0.2}MnO_3$ is in the order of 10^2-10^3 (fig 3.3). Similar values were measured in $La_{0.75}Sr_{0.25}MnO_3$; but in $La_{0.85}Sr_{0.15}MnO_3$ samples, the resistance ratio decreases up to 5 read at -1V. Owing to the fact that the electrical and magnetic properties of $La_{1-x}Sr_xMnO_3$ layers can be modified by chemical doping, in this case the Sr content, the resistive switching characteristics can be tuned by changing this parameter as well.

3.1.5 Summary of results observed in $La_{1-x}Sr_xMnO_3$ devices

First, bipolar resistive switching has been demonstrated at the micrometric scale in the memristor devices only when measurement probes were located directly on top of the La_{1-x} Sr_xMnO_3 layer. In any of the cases, no remarkable resistive switching could be induced when probes were located in metal electrodes. This is explained by the

proposed mechanism based on the oxygen ion exchange through a MIT transition, where the exchange of the oxygen ions with the ambient is favored at the probe/$La_{1-x}Sr_xMnO_3$ contact.

Moreover, it has been presented that the resistive switching characteristics, such as the Vset, Vreset endurance and resistance ratio, can be tuned by changing the thickness and the Sr doping content of the $La_{1-x}Sr_xMnO_3$ layers. In addition, multilevel resistive switching has been demonstrated by controlling the V_{max} applied during the voltage sweep in probe/ $La_{0.8}Sr_{0.2}MnO_3$/probe devices.

However, in order to fully use the $La_{1-x}Sr_xMnO_3$ as an active layer for resistive switching in non-volatile memory devices, the resistive switching has to be induced with metal electrodes.

3.2 Resistive Switching evaluation in bilayer devices

In the last section, the switching properties in $La_{1-x}Sr_xMnO_3$ have been only reported when measurement probes were located directly on top of the layer. According to the proposed mechanism, the switching is produced when oxygen ions are exchanged from the La_{1-x} Sr_xMnO_3 to the ambient and vice versa due to the polarity of the applied field. However, to fully demonstrate the feasibility of the use of the $La_{1-x}Sr_xMnO_3$ layer in memristor devices, it is mandatory to use metal electrodes. In order to overcome this problem, the implementation of a thin layer on top of the LSMO film, in a bilayer system, has been proposed with the objective of improving the oxygen ion exchange from the $La_{1-x}Sr_xMnO_3$ layer and hence, the resistive switching characteristics.

Recently, cerium dioxide (CeO_2) has been extensively investigated to serve as electrolyte material of solid oxide fuel cells due the ability of oxygen ion conduction [84], [116]. The reducibility of CeO_2 to CeO_{2-x} contributes to oxygen storage and release capability, which is compatible with the mechanism responsible of the resistive switching in $La_{1-x}Sr_xMnO_3$ layers.

Moreover, resistive switching properties have been reported in capacitors with CeO_2 as insulating layer. Depending on the deposition route followed to obtain the CeO_2 layer and the metal electrode used to form the MIM structure, the resistive switching characteristics observed are diverse: from unipolar to bipolar resistive switching.

However, an electroforming process is usually needed in order to induce the local phenomenon [16], [17], [90].

For these reasons, the implementation of the $CeO_{2-x}/La_{1-x}Sr_xMnO_3$ bilayer, used as element in memristor devices, is explored here.

3.2.1 Evaluation of CeO_{2-x} single layer in lateral devices

In this work, CeO_{2-x} layer was deposited by ALD method at low temperature on top of LSMO as described in chapter 2. However, in order to investigate the influence in the resistive switching characteristics of $La_{1-x}Sr_xMnO_3$, a single layer of CeO_{2-x} with thickness of 10nm was also deposited apart on top of a conductive $SrTiO_2$ doped Nb 0.05wt% (Nb:STO) substrate. Then, metal electrodes (Ag, Au and Pt), defined by photolithography, were sputtered on top of the CeO_{2-x} layer to form the metal/CeO_{2-x}/metal lateral devices (figure 3.14a). Double voltage sweeps were applied to these devices in order to evaluate their electric characteristics. In any case, resistive switching behavior was never induced even applying a sweep voltage of ±10V as seen in figure 3.14b. A high insulating behavior is observed during the whole applied voltage sweep. From these measurements we can conclude that no metallic conductive filaments were formed inside the CeO_{2-x} layer, especially those reported by Sawa *et al.* [117] where Ag conductive ions form a conductive filament produced by an electrochemical migration effect. Therefore, the ALD CeO_{2-x} can be used to evaluate the effect of promoting oxygen exchange in $La_{1-x}Sr_xMnO_3$ devices.

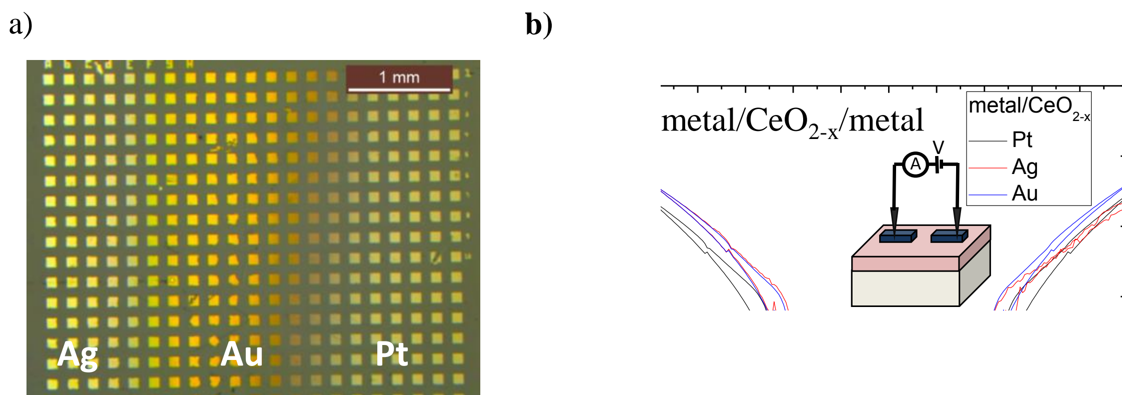

Fig. 3.14 a) Top view image of the measured devices showing the deposition of the three metals on the CeO_{2-x} layer. b) I-V curves measured in metal/CeO_{2-x}/metal lateral devices

3.2.2 Evaluation in CeO_{2-x}/$La_{0.8}Sr_{0.2}MnO_3$ bilayers using Ag electrodes

At the same time during the development of this thesis, a CeO_2 thin layer on top of $La_{0.7}Sr_{0.3}MnO_3$ was used to demonstrate the resistive switching characteristics through C-SFM [59] at the SUMMAN group of ICMAB-CSIC. In that work, modifications of the resistive switching characteristics of $La_{0.7}Sr_{0.3}MnO_3$ layer were reported when a thin CeO_2 layer was deposited on top. We depart from this initial approach in order to demonstrate the RS in bilayer devices using micrometric contacts.

Resistive switching characteristics were evaluated using Au, Ag and Pt metal electrodes for comparison reasons. Although all of them showed resistive switching characteristics, the most stable and reproducible results were found in lateral Ag/CeO_{2-x}/$La_{0.8}Sr_{0.2}MnO_3$/CeO_{2-x}/Ag devices. For this reason, all the results presented along these sections refer only to devices with Ag electrodes. Figure 3.15a shows the first positive voltage sweep performed on a pristine device until +5V where an electroforming event which is necessary to induce the resistive switching is observed. This electroforming turns the device from a very high insulating state to a less resistive one but without reaching completely the LRS of the resistive switching phase. Figure 3.15b shows the following negative voltage sweep that induces a sharp increase of current where a change from HRS to LRS is observed (branch 1). The device remains in the LRS during the voltage back excursion (branch 2). At positive voltage sweep, the memory device maintains the LRS until a sharp decrease of the current leads to a change to the HRS (branch 3) which is retained in the voltage back sweep (branch 4). Consequently, BRS is confirmed in Ag/CeO_{2-x}/$La_{0.8}Sr_{0.2}MnO_3$/CeO_{2-x}/Ag devices.

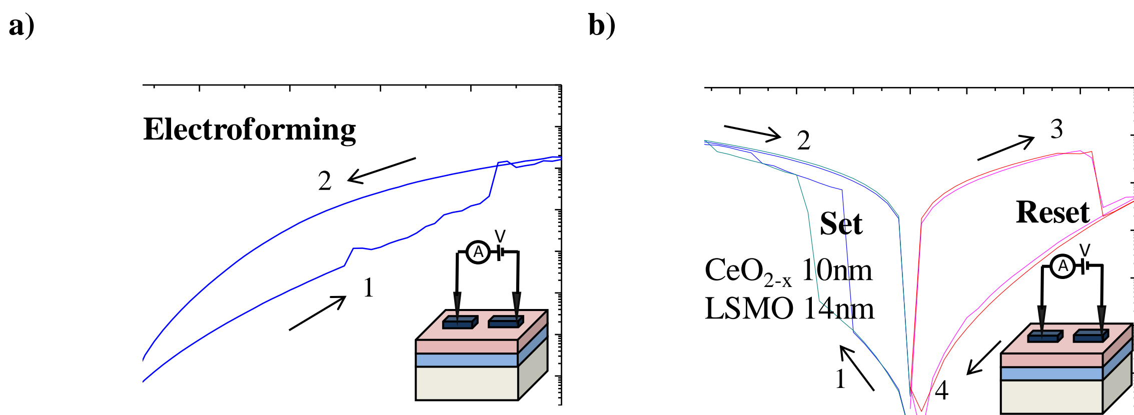

Fig. 3.15 I-V curves measured in on Ag/CeO_{2-x}/$La_{0.8}Sr_{0.2}MnO_3$/CeO_{2-x}/Ag devices. a) electroforming and b) BRS induced when probes are placed on metal electrodes

Comparing the BRS in these bilayer devices with the results observed in $La_{0.8}Sr_{0.2}MnO_3$ when the measurement probes were located directly on top of the layer, a decrease of the voltage operation is clearly accomplished probably due to the lower value of the contact resistance using metal electrodes. In addition, the Set and Reset transitions are sharply achieved which could be produced by the easier oxygen ion exchange between the CeO_{2-x} and the $La_{0.8}Sr_{0.2}MnO_3$ layer as explained later for the proposed mechanism.

The repeatability of the BRS in lateral $Ag/CeO_{2-x}/La_{0.8}Sr_{0.2}MnO_3/CeO_{2-x}/Ag$ devices was also measured up to 100 cycles. Figure 3.16a demonstrates the cycle-to-cycle repeatability after the electroforming with the Set/Reset voltages showing small variation from one cycle to another. Figure 3.16b shows the resistance ratio to be around 10^4 for these cycles at read voltage of -0.5V. It is clearly observed in this figure that the ratio is maintained along the 100 cycles with high reproducibility of the resistance values.

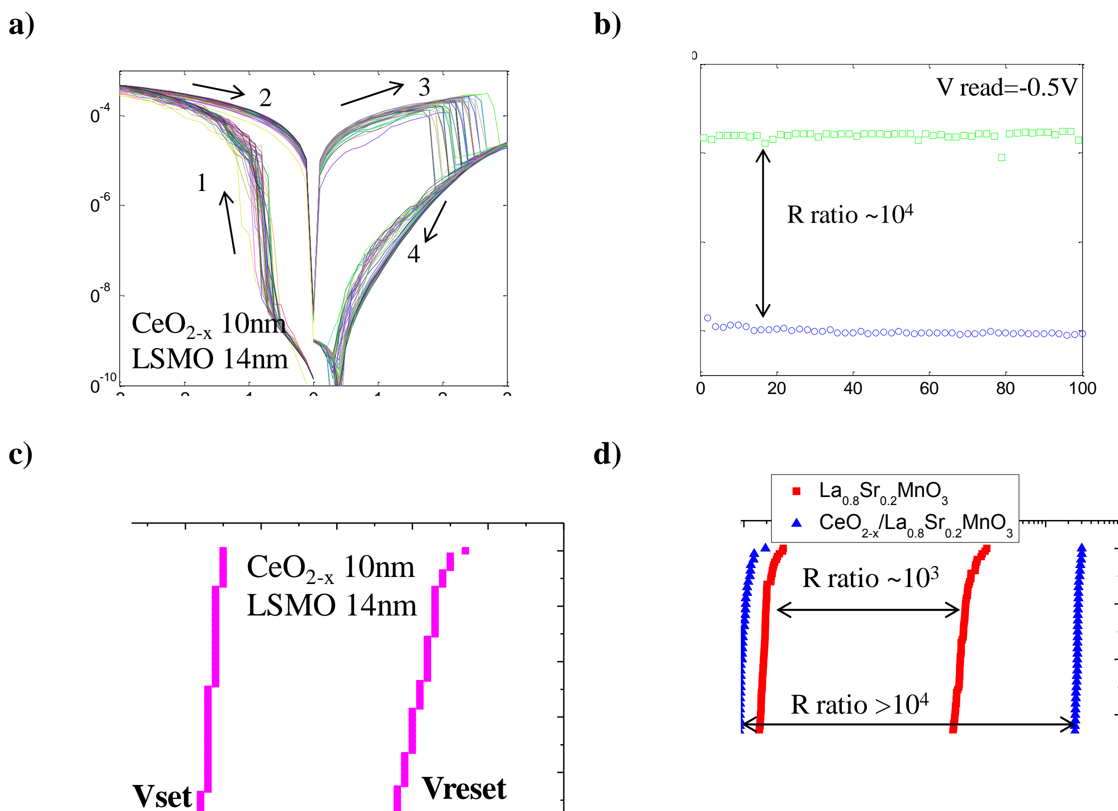

Fig. 3.16 a) Repeatability demonstrated in lateral $Ag/CeO_{2-x}/La_{0.8}Sr_{0.2}MnO_3/CeO_{2-x}/Ag$ devices after the electroforming. b) The resistance ratio measured at -0.5V. c) Distribution of the Vset/Vreset measured during the repeatability performance and d) Distribution of the resistance values comparing the values measured in single $La_{0.8}Sr_{0.2}MnO_3$ and bilayer $CeO_{2-x}/La_{0.8}Sr_{0.2}MnO_3$

The voltage values at which the Set/Reset transitions occur are plotted in figure 3.16c. It is observed that the transitions in bilayer systems are produced at relative low voltages values. For instance, the Set transition in bilayer is produced at voltage values smaller than -1V. From the mechanism point of view, the CeO_{2-x} layer improves the efficiency of oxygen ion exchange between this layer and the $La_{0.8}Sr_{0.2}MnO_3$ because it acts as an oxygen reservoir.

Figure 3.16d compares the resistance ratio between the values measured in $La_{0.8}Sr_{0.2}MnO_3$ devices and $CeO_{2-x}/La_{0.8}Sr_{0.2}MnO_3$ bilayer devices, showing the resistance ratio in the former is more than 10 times higher. In addition, despite the resistance ratios were measured at different voltages for the $La_{0.8}Sr_{0.2}MnO_3$ devices and the CeO_{2-x}/ $La_{0.8}Sr_{0.2}MnO_3$ bilayer system, the ratios were always taken at their maximum value confirming that low voltage values can produce higher resistance values in bilayer systems. For non-volatile memory applications, large resistance ratios to distinguish between the On and Off states, and small voltage operation for low power consumption are highly desired [7].

In conclusion, the properties observed in $La_{0.8}Sr_{0.2}MnO_3$ are deeply modified when a thin CeO_{2-x} layer is deposited on top. In particular, the addition of this layer enables BRS using metal electrodes, a result which was not achieved using single $La_{0.8}Sr_{0.2}MnO_3$ layers. Moreover, the resistance ratio is enhanced while the voltage needed to induce the Set/Reset transitions is decreased. These demonstrate that the use of a thin layer as oxygen reservoir modifies the $La_{0.8}Sr_{0.2}MnO_3$ properties and open the possibility of implementation as non-volatile memory devices.

3.2.3 Resistive switching mechanism in bilayer devices

The oxygen ion exchange through a MIT transition has been already proposed as the mechanism to induce resistive switching in $La_{1-x}Sr_xMnO_3$ devices. From our previous results in single $La_{1-x}Sr_xMnO_3$ layers, we state that the oxygen ion exchange is produced between the layer and the ambient. In addition, the oxygen migration is blocked by the use of metal electrodes and only when the measurement probes are located directly in contact with the $La_{1-x}Sr_xMnO_3$, the resistive switching is produced. For $CeO_{2-x}/La_{1-x}Sr_xMnO_3$ bilayer systems, the BRS is explained using the same oxygen ion exchange mechanism. Figure 3.17a shows the structure of one side of the lateral device under the measurement probe because the switching is produced only under one electrode

favoured by the electric field. In figure 3.17b, when an electric field is applied in the direction of the arrow, the oxygen anions are attracted to the $CeO_{2-x}/La_{1-x}Sr_xMnO_3$ interface where they are trapped, enabling the transition from LRS to HRS (Reset) of the device. When an electric field is applied to the same electrode but in the opposite direction, the oxygen anions are released from the CeO_{2-x} layer and they go back to the $La_{1-x}Sr_xMnO_3$ thus switching the layer to the initial LRS (Set) as shown in figure 3.17c. We believe that the CeO_{2-x} layer is acting as an oxygen reservoir which promotes easier ionic motion between the layers producing a reduction of the voltage operation of the devices and higher resistance ratios.

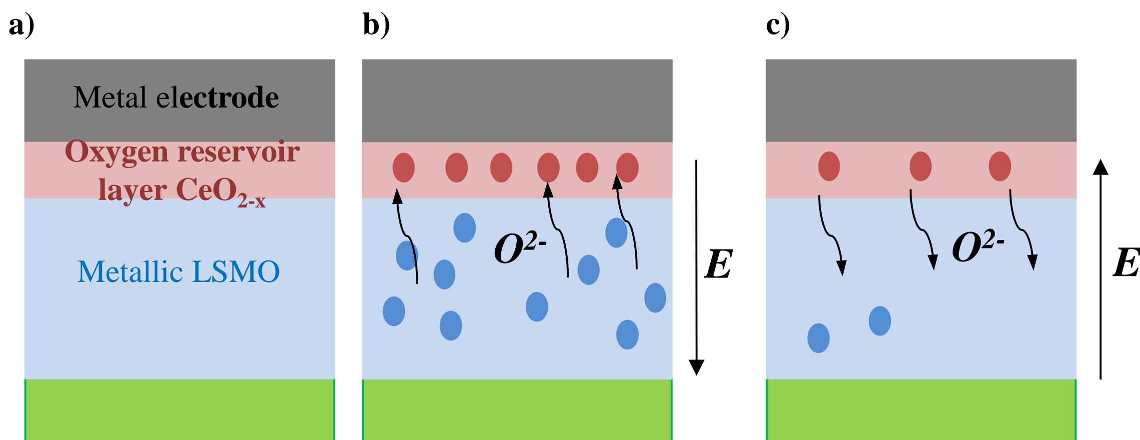

Fig. 3.17. Schematic representing the proposed mechanism for BRS in bilayer CeO_{2-x}/ $La_{1-x}Sr_xMnO_3$ devices

The presented mechanism qualitatively explains the BRS behavior observed in $La_{1-x}Sr_xMnO_3$-based devices after the electroforming process. In addition, it suggests the importance of the oxygen content in the switching layer and the control that should be taken during the fabrication process.

According to this mechanism, the oxygen migration can be produced under any metal electrode provided that the direction of the electric field favors the oxygen ion migration and the previous state of the transformed layer similar to what was proposed for $La_{0.8}Sr_{0.2}MnO_3$ devices. In addition, due to symmetry of the lateral devices, the Set/Reset transitions can occur at any polarity regarding the previous induced state in the device. However, once the BRS is produced in $CeO_{2-x}/La_{1-x}Sr_xMnO_3$ bilayer systems, the switching interface will be the same during the successive cycles.

3.2.4 Complementary Resistive Switching in CeO_{2-x} /$La_{0.8}Sr_{0.2}MnO_3$ bilayer devices

Complementary Resistive Switching (CRS) has been already proposed as a solution for the sneak-path current in crossbar arrays [4]. This kind of resistive switching has been observed when two memristors devices are antiserially-connected with inert top and bottom electrodes with an intermediate common active electrode as explained previously in chapter 2. Although the most studied configuration of memristors devices for CRS is the vertical configuration [29], [118], the lateral Ag/CeO_{2-x}/$La_{0.8}Sr_{0.2}MnO_3$/CeO_{2-x}/Ag memristor devices have the same structure with the $La_{1-x}Sr_xMnO_3$ layer acting as intermediate common metal layer.

The CRS is observed in lateral Ag/CeO_{2-x}/$La_{0.8}Sr_{0.2}MnO_3$/CeO_{2-x}/Ag devices when the voltage excursion is increased in both polarities up to ±5V after the electroforming event. As observed in figure 3.18, starting at small voltages, a sharp increase of current is observed around 1V (branch 1). The current increase steadily as the voltage also increases until a sharp decrease is observed at certain positive value (branch 2). The current remains in the HRS during the voltage back excursion (branch 3). For the opposite bias voltage, similar current behavior is observed (branches 4, 5 and 6). Regarding CRS, the Set and Reset transitions take place in the same program operation provided that enough electric field has been applied. It is noteworthy that each program sequence ends up with a reset operation which leaves the memory element always in a HRS.

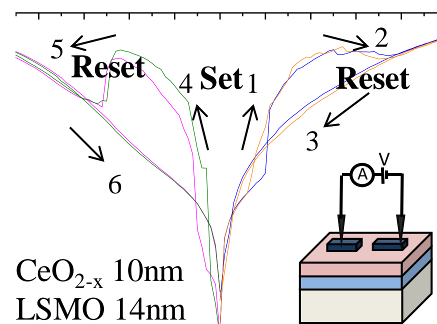

Fig. 3.18. Complementary Resistive Switching (CRS) observed in Ag/CeO_{2-x}/$La_{0.8}Sr_{0.2}MnO_3$/CeO_{2-x}/Ag bilayer devices when the voltage sweep is increased up to ±5V after the electroforming

In figure 3.19, a sequence of CRS is explained from the mechanism point of view. In this case, positive voltage is defined when current flows from electrode A to electrode

B. Moreover, considering that LRS has been induced in a previous operation, after electroforming, under electrode A (figure 3.19a). As the positive voltage sweep increases, the oxygen migration is favored by the electric field direction and the voltage drop enhanced at the HRS area under metal electrode B, producing a transition to LRS at a voltage value of Vth1. At this point, the LRS has been produced in both regions under the electrodes; as a result, the device is in the ON state (figure 3.19b). Moreover, as the positive voltage continues increasing, and once more favored by the direction of the electric field, the layer under the metal electrode A is switched to the HRS when the voltage reaches the Vth2 value, enabling a Reset transition (figure 3.19c). Although the voltage continues increasing, any other transition is observed and the device remains in the HRS (state OFF) during the voltage back excursion. Repeating this process in the opposite bias direction, the same CRS behavior is demonstrated owing to the fact of the device symmetry. Contrary to what happens during BRS, complementary switching involves both junctions alternatively, which are both Set and Reset during operation. In summary, CRS has been demonstrated in $Ag/CeO_{2-x}/La_{0.8}Sr_{0.2}MnO_3/CeO_{2-x}/Ag$ devices when the voltage sweep is increased up to ±5V producing a Set and Reset transition at the same voltage bias. Consequently, after any voltage sweep the device remains in the HRS which can be used as a solution to the sneak-path current in crossbar arrays.

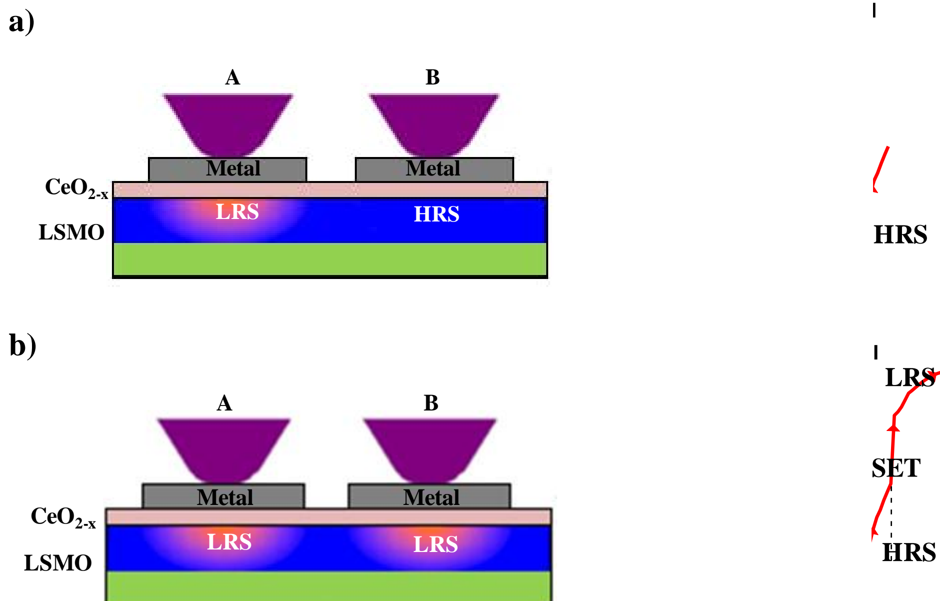

c)

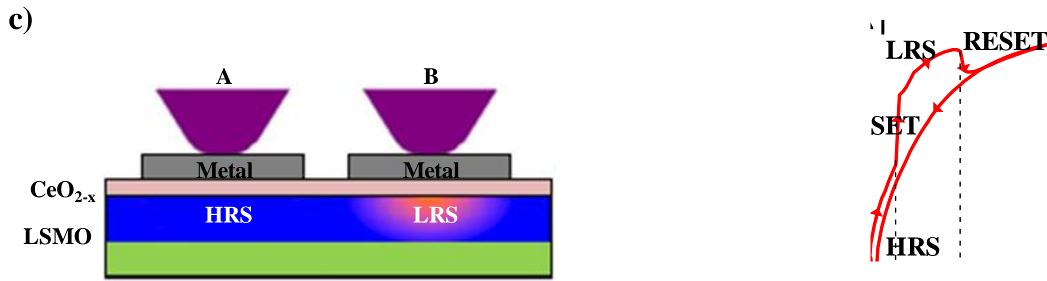

Fig. 3.19 Complementary Resistive Switching mechanism observed in Ag/CeO_{2-x}/$La_{0.8}Sr_{0.2}MnO_3$/CeO_{2-x}/Ag bilayer devices. a) a LRS has been induced under electrode A in a previous operation, b) a subsequent positive voltage sweep is applied enabling a transition to the LRS under metal electrode B at Vth1; and c) transition to HRS under metal electrode A when the value of the voltage sweep increases until Vth2.

3.2.5 Resistive Switching in CeO_{2-x}/$La_{0.7}Sr_{0.3}MnO_3$ bilayer devices

According to our previous results during the evaluation of $La_{0.7}Sr_{0.3}MnO_3$ layers, no resistive switching behavior could be induced even when the measurements probes were located directly on top of the layer. Different results were obtained when the same device was evaluated using a C-SFM approach. However, after the demonstration of RS in the Ag/CeO_{2-x}/$La_{0.8}Sr_{0.2}MnO_3$/CeO_{2-x}/Ag bilayer devices and the ability of the CeO_{2-x} layer to act as an oxygen reservoir, we decided to implement the same kind of device but using a CeO_{2-x}/$La_{0.7}Sr_{0.3}MnO_3$ bilayer instead. The RS was evaluated in a device with a CeO_{2-x} layer of 10nm in thickness on top of a $La_{0.7}Sr_{0.3}MnO_3$ layer of 14nm.

First, BRS has been achieved in these devices when the sweep voltage is stopped at ±2V as observed in figure 3.20a. In this figure, the Set and Reset transition are inverted in polarity with respect to what was shown in the last results of CeO_{2-x}/$La_{0.8}Sr_{0.2}MnO_3$ bilayer system. However, this behavior is expected due to device symmetry and the fact it also depends on the direction of the first voltage sweep. In this case, some previous voltage sweeps had been performed prior these measurements. It is worth noting that the electroforming process is also required in these devices to induce the resistive switching although it is not shown in the curves.

Moreover, in figure 3.20b CRS measured in the same device is presented. Starting from 0V, a Set transition is observed around 1V (branch 1) and a Reset at the same voltage sweep around 2.5V (branch 2); during the voltage back excursion, the device remains in the HRS (branch 3). This CRS is also observed at the opposite bias during the voltage sweep from 0V to -5V (branches 4, 5 and 6) which is in agreement with our previous

observation in $CeO_{2-x}/La_{0.8}Sr_{0.2}MnO_3$ bilayer devices. The coexistence of both switching modes, BRS and CRS in the same device, is confirmed as explained by Nardi *et al.* [29]. When the V_{max} is small, only BRS is observed under one of the junctions which alternatively produces a Set and Reset under opposite voltage polarities. When V_{max} is increased, both junctions switch during operation. Changing the maximum voltage, the device can be switched from form BRS and CRS and vice versa.

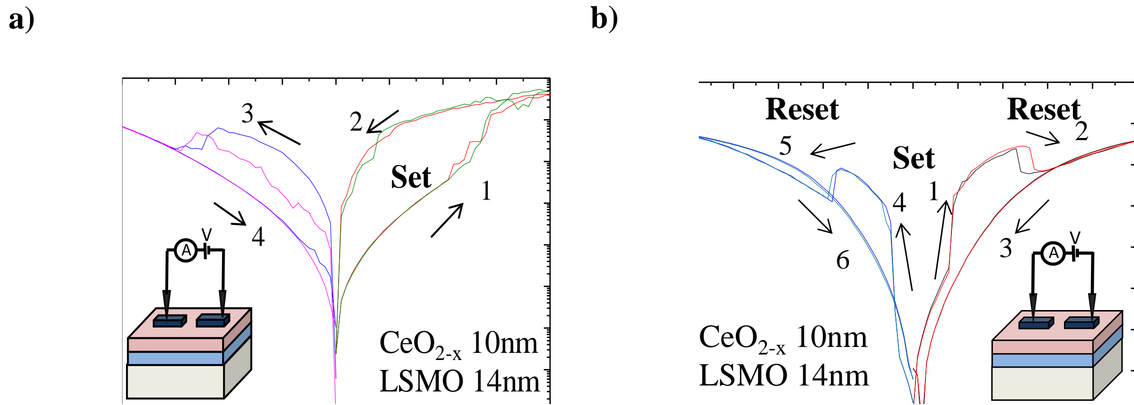

Fig. 3.20 a) CRS and b) BRS observed in Ag/$CeO_{2-x}/La_{0.7}Sr_{0.3}MnO_3/CeO_{2-x}$/Ag bilayer devices

Once the BRS has been demonstrated in Ag/$CeO_{2-x}/La_{0.7}Sr_{0.3}MnO_3/CeO_{2-x}$/Ag devices, their repeatability is investigated applying consecutive voltage sweeps. The measured curves up to 100 cycles are shown in figure 3.21. In this figure, we can observe some unstable cycles during the Reset transition at reverse bias which produces an increment in the negative voltage sweep required to accomplish the transition from LRS to HRS. The sharp Set and Reset transitions could indicate that the oxygen ion exchange is produced faster between the CeO_{2-x} and $La_{0.7}Sr_{0.3}MnO_3$ layers. The resistance ratio measured at 0.5V and the cumulative probability of the resistance values are shown in figure 3.21b and 3.21d, respectively. The average value of the resistance ratio observed in these devices is around 10^2, a lower value compared to the ~10^4 measured in $CeO_{2-x}/La_{0.8}Sr_{0.2}MnO_3$ bilayer devices. Figure 3.21c illustrates the dispersion of the Vset and Vreset measured in this device.

Finally, the BRS which had been already observed before in $La_{0.7}Sr_{0.3}MnO_3$ layers [9] and $CeO_2/La_{0.7}Sr_{0.3}MnO_3$ bilayers [59] through C-SPM has been successfully reproduced at device level using micrometric size metal electrodes thus demonstrating the feasibility of these materials to be used in non-volatile memory devices.

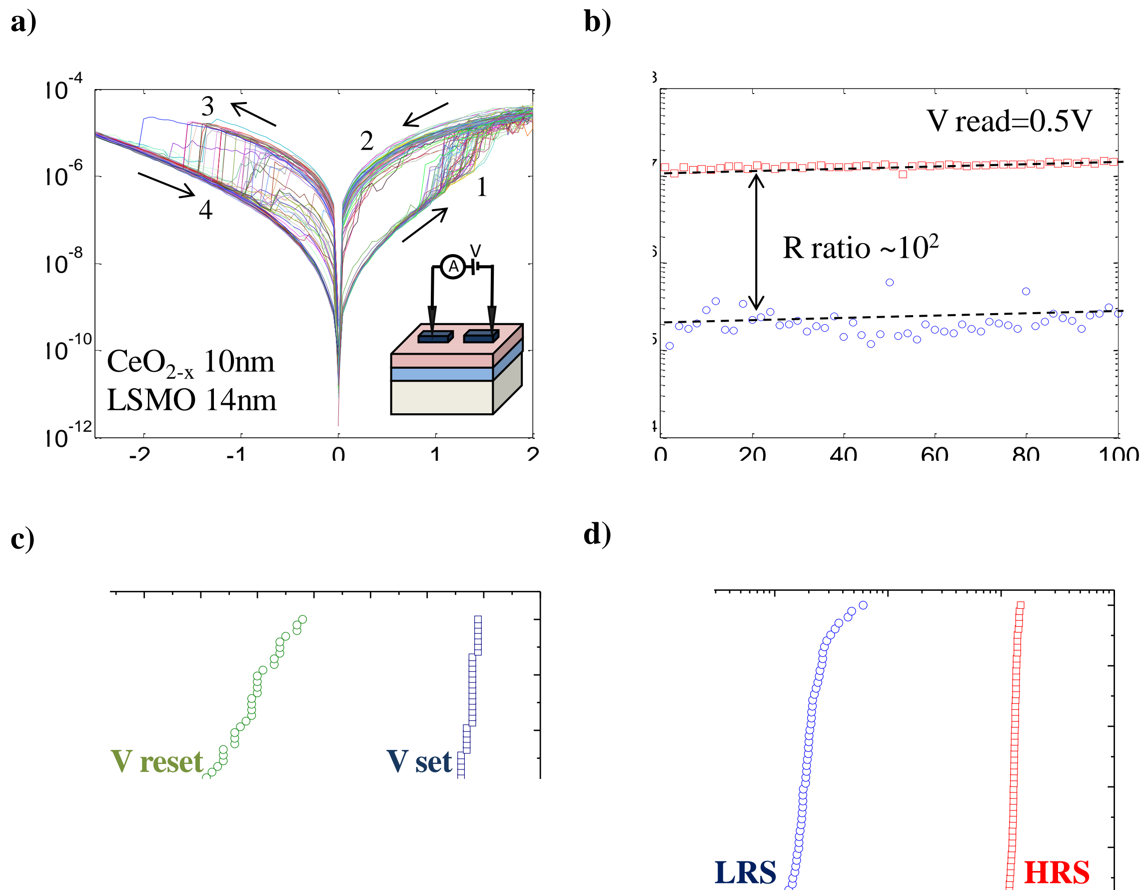

Fig. 3.21 Repeatability measured at least up to 100 cycles in $Ag/CeO_{2-x}/La_{0.7}Sr_{0.3}MnO_3/CeO_{2-x}/Ag$ devices. b) Resistance ratio of 10^2 measured at 0.5V. c) dispersion of the Vset and Vreset measured values and d) cumulative probability of the resistance values

3.2.6 Conclusions about Resistive Switching in $CeO_{2-x}/La_{1-x}Sr_xMnO_3$ bilayers

In this section, we have presented the evaluation of the resistive switching in $Ag/CeO_2/La_{1-x}Sr_xMnO_3/CeO_{2-x}/Ag$ bilayers devices. First, we have successfully achieved the use of metal electrodes to induce bipolar and complementary resistive switching. In addition, modifications of the RS has been observed in $La_{0.8}Sr_{0.2}MnO_3$ whet it was evaluated in a bilayer system due to the fact that the CeO_{2-x} layer acts as an oxygen reservoir promoting the oxygen ion exchange between these layers. The characterization of the $CeO_2/La_{0.8}Sr_{0.2}MnO_3$ bilayer demonstrate that the physical properties of the $La_{0.8}Sr_{0.2}MnO_3$ layer has not been modified indicating that the CSD and ALD deposition methods are compatible for the fabrication of memristive devices.

In addition, an electroforming process is necessary in pristine bilayer devices in order to induce the bipolar and complementary resistive switching phenomena. This electroforming turns the device from a very insulating behavior to an intermediate resistance state without reaching the low resistance state. Regarding bipolar resistive switching, it has been demonstrated repeatability over at least 100 Set/Reset cycles with resistance ratio of ~10^4 and device operation at relative low voltage between ±3V which is highly desired for the implementation of these devices as non-volatile memory devices.

3.3 Volume switching in bilayer devices

The modification across the whole thickness of the $La_{1-x}Sr_xMnO_3$ layer, produced by resistive switching phenomenon is called volume switching. The demonstration of this phenomenon through thickness in thin $La_{0.7}Sr_{0.3}MnO_3$ (10nm) layers has been already reported [9]. In these experiments, Moreno *et al.* used a C-SPM strategy, with a lateral configuration (Fig. 3.22), to induce the so-called volume switching. This experiment was later reproduced using our $La_{0.8}Sr_{0.2}MnO_3$ layers; figure 3.23 shows these images. It consisted of writing a ring with the measurement tip, at -10V (fig. 3.23a). The commercial tip used in these experiments is from Bruker DDESP-10 made of conductive diamond with radius of 200nm. Figure 3.23b shows that the unmodified inner part of the ring had been isolated from the rest of the layer. This behavior was produced by modifying the conduction state of the layer through the whole thickness. This was later confirmed by switching back a trajectory crossing the ring and finding that the non-modified conductive region inside of the ring was observed again in the conduction map (fig 3.23c). Such a simple experiment demonstrated the volume switching in $La_{0.8}Sr_{0.2}MnO_3$ layers was produced by a field effect and that could be accomplished by controlling the thickness of the layer.

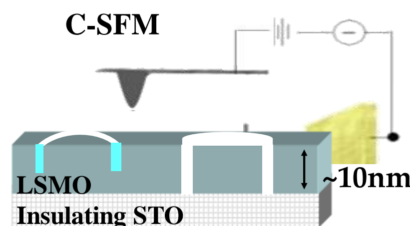

Fig, 3.22 Schematic of the C-SFM measurement set up used to produce the volume switching in $La_{1-x}Sr_xMnO_3$ layers. The voltage is applied through the probe and a metallic contact that is usually attached at the corner of the sample.

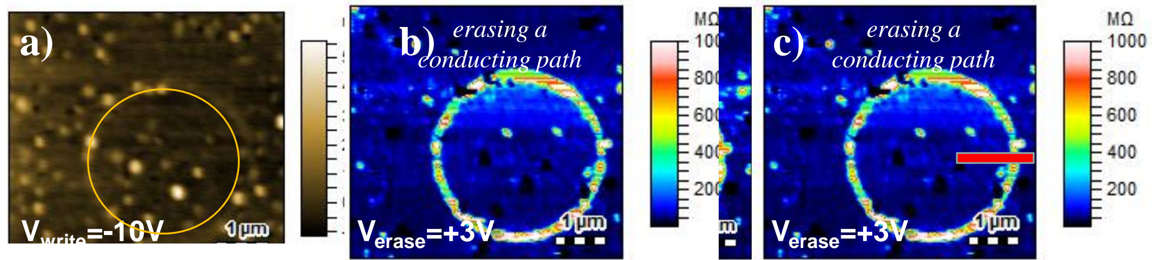

Fig 3.23 a) Topographic image of the ring written at -10V on $La_{0.8}Sr_{0.2}MnO_3$ layer 10nm. Later in b) when the current map is measured the inner region of the ring, which has not been modified, appears to be isolated. c) erasing a conducting path by applyin +3V, indicated by the red line, the non-modified area inside of the ring appears again in the conduction map. Courtesy of J.C. Gonzalez

As one important objective of this thesis, we wanted to reproduce this behavior at device level through the fabrication of three terminal field-effect based lateral memristor devices. To this purpose, test structures with metal gates were evaluated in order to demonstrate the feasibility of volume switching at device level. We have chosen the Ag/CeO_{2-x}/ $La_{0.8}Sr_{0.2}MnO_3$/CeO_{2-x}/Ag bilayer devices for this evaluation due to reliable switching properties presented before. The thickness of the CeO_{2-x} layer was 10nm while the $La_{0.8}Sr_{0.2}MnO_3$ layer was 40nm.

3.3.1 Evaluation of volume switching in three-terminal (3T) devices

Volume switching was evaluated on the three terminal structures defined by photolithography which are presented on a top view in figure 3.24a. As described in the fabrication process, the three terminal devices were first designed by software which allows the control of the structure’s dimensions. Then, the CeO_{2-x}/$La_{0.8}Sr_{0.2}MnO_3$ is etched by a RIE process and taken again to photolithography to define the metal electrodes by sputtering. The dimensions were chosen such that the measurement probes could be easily placed on the metal electrodes, especially on the gate electrode where the resistive switching was induced. Figure 4.24b shows a picture of the fabricated structures. The gate electrode is used to adjust the resistance along the track in a non-volatile, continuously tunable manner. In figure 4.24c, the induced resistive switching modifies the resistance of the LSMO vertically under the gate electrode. Then, the resistance of the track is evaluated transversally by performing a low voltage measurement. The evaluation of the conduction along the track is modified according the resistance state of the area under the gate electrode.

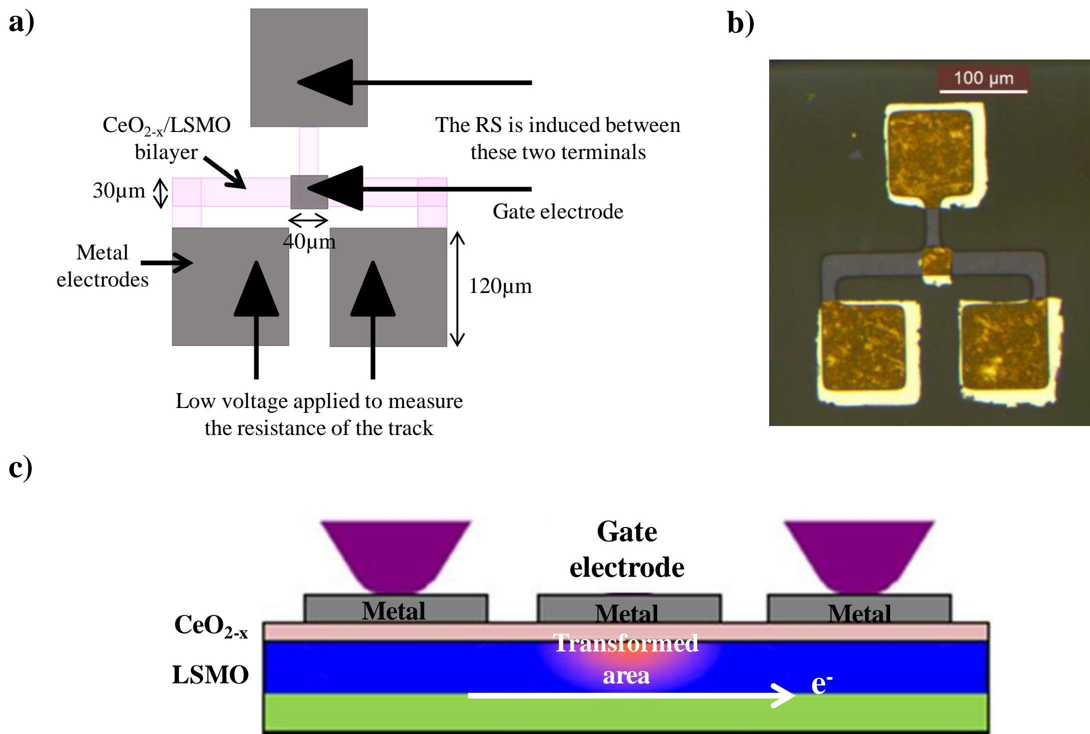

Fig. 3.24 Schematic of the three terminal structures a) Top view of the devices indicates the outermost electrodes where low voltage sweep is performed and the gate electrode where resistive switching is induced. b) Image of the fabricated structure and c) lateral view of the device indicating the current conduction along the LSMO layer which is modified when the resistance of the area under the gate electrode is modified.

In order to perform the evaluation of these devices, four probes were used to contact the metal electrodes. The probes were systematically enabled or disabled by software according to the procedure presented as follows.

1. First, the resistance of the track is measured applying a low voltage (±1V) between the outermost electrodes (Fig. 3.25a).
2. Then, the RS is induced through the probe on top of the gate electrode, located on the track (Fig. 3.25b).
3. Finally, the resistance is measured again, at low voltage values, between the outermost electrodes after each Set/Reset transition process (Figure 3.25c).

This procedure is repeated as many times as necessary to evaluate the volume switching. As a result, two different resistance states are able to be measured after each device transition (Set or Reset).

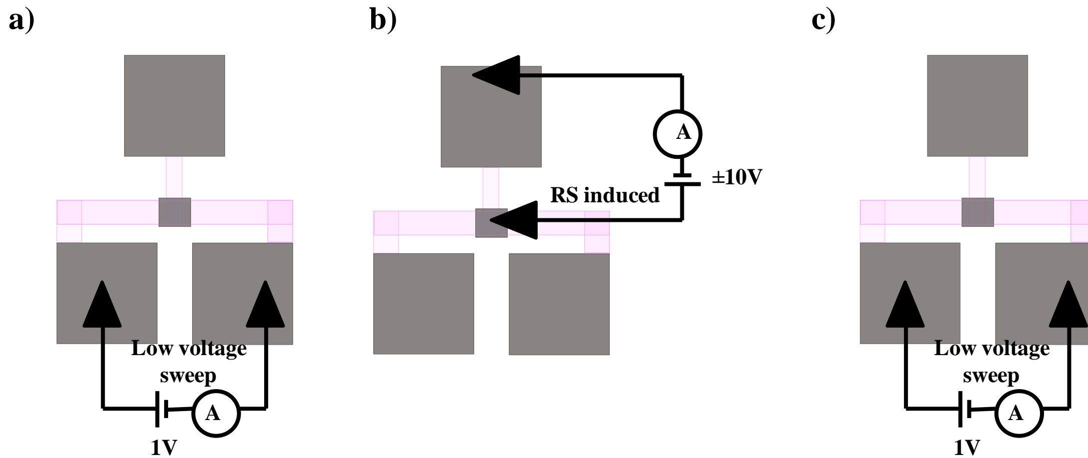

Fig. 3.25 Measurement setup used to evaluate the volume switching a) Low voltage sweep is used to evaluate the initial state of the track between the outermost electrodes. b) The RS is induced under the gate electrode by applying ±10V. c) Finally, the resistance along the track is evaluated again using low voltage sweep. The resistance of the track is changed after Set/Reset process

The resistance along the track is modified when the area under the gate electrode is modified by the RS effect. For this reason, it is necessary to assure that the low voltage measurements of the track do not modify the conduction on it. From our previous experiments we know that the RS effect is observed in bilayer devices just after an electroforming is performed, for this reason the low voltage sweep between the track electrodes assures that any transition is induced.

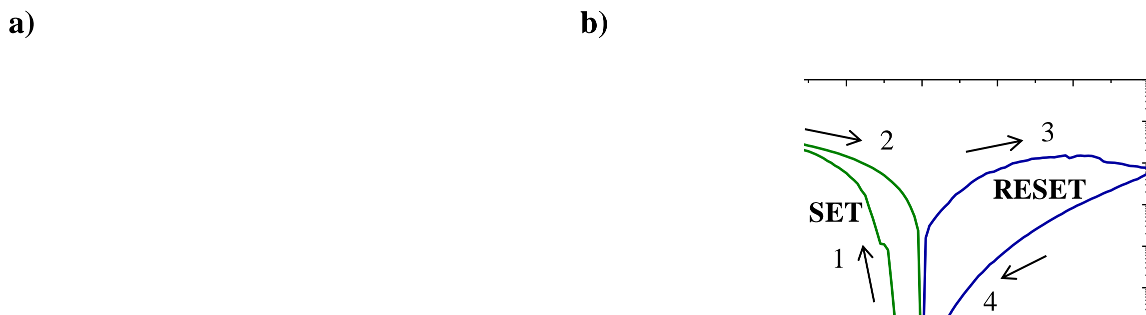

Fig. 3.26 a) Low voltage sweep performed in the outer electrodes of the track to investigate the resistance after each device operation. b) BRS under the gate electrode modifies the conduction properties of the track.

Figure 3.26 shows the measurement performed in these devices. Figure 4.26a shows the low voltage measurements performed in the outermost electrodes while figure 4.26b presents the BRS induced under the gate electrode. First, the resistance of the track is

measured after the electroforming process, in the plot is indicated as the initial curve. The track resistance of 1.1MΩ shows the HRS indicating that any breakdown in the CeO_{2-x} neither in the $La_{0.8}Sr_{0.2}MnO_3$ has been inducing during the electroforming process. Then, negative voltage up to -3V is applied between the gate and the third electrode (branches 1-2). This produces a transition from the HRS to LRS in the $La_{0.8}Sr_{0.2}MnO_3$ layer under the gate electrode due to oxygen migration mechanism. A new low voltage measurement is performed on the track between the outermost electrode where is observed that the resistance has decreased until a value of 66kΩ after the Set process, in the figure shown as the 'after Set' curve. Then, applying positive voltage at the gate electrode up to 3V, a change from LRS to HRS is produced (branches 3-4). The track resistance has increased until a value of 1MΩ recovering the initial state after this Reset transition.

From a circuit point of view, the resistance along the track can be represented by three resistances in series when the device is at the initial HRS (figure 3.27a). Different resistance values are observed when the RS is produced under the gate electrode as shown in figure 3.27b. The R_1 and R_3 resistances represent the untransformed area (HRS) of the track while the parallel resistances R_{2A} and R_{2B} represent both the transformed and the untransformed area, if any, under the gate electrode after a transition has been produced.

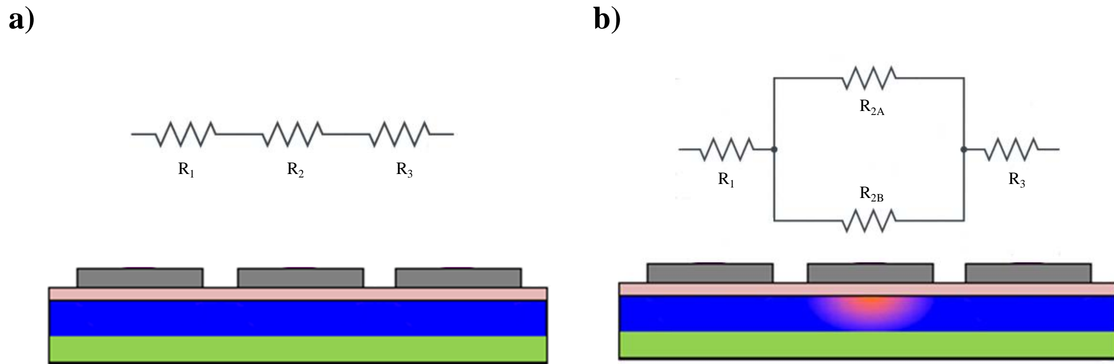

Fig. 3.27 a) Equivalent circuit of the device when it is in the HRS and any transition has been produced. b) Equivalent circuit when a transition to LRS has been produced under the gate electrode, the resistances in parallel denote the HRS and LRS of the transformed area

The resistance of the transformed area in the LRS can be calculated using the following expression:

$$R_{2A} = \rho_{LSMO} \frac{L}{W(t_{LSMO} - x)} \qquad \text{Eq. 4.1}$$

The ρ_{LSMO} and t_{LSMO} are the resistivity and the thickness of the LSMO layer respectively. The x factor indicates the part of the LSMO thickness that has been switched to the LRS. The equivalent resistance R_{eq} of the device as indicated in the figure 4.27b is presented as follows:

$$R_{eq} = \frac{R_{2A} \cdot R_{2B}}{R_{2A} + R_{2B}} \quad \text{Eq 4.2}$$

From the resistance ratio measurements we can make the approximation that the value of the R_{2B} is $R_{2B}=10^3 R_{2A}$. Substituting this value in eq. 4.2 we obtain:

$$R_{eq} = \frac{R_{2A} \cdot 10^3 R_{2A}}{R_{2A} + 10^3 R_{2A}} \quad \text{Eq. 4.3}$$

$$R_{eq} = \frac{R_{2A} \cdot 10^3 R_{2A}}{R_{2A}(1 + 10^3)} \quad \text{Eq. 4.4}$$

$$R_{eq} = R_{2A} = \rho_{LSMO} \frac{L}{W(t_{LSMO} - x)} \quad \text{Eq. 4.5}$$

The part of the transformed thickness can be known provided that all the parameters are known related to the geometry of the transformed area and resistivity. However, we only know that the resistance ratio measured along the track between the LRS and the HRS is around 15. The expression relating these parameters is presented as follows:

$$R_{ratio} = \frac{R_{HRS}}{R_{LRS}} = \frac{R_1 + R_2 + R_3}{R_1 + R_{eq} + R_3} \quad \text{Eq. 4.6}$$

The R_{HRS} and R_{LRS} of the track have been already measured when the cycles were evaluated. In addition, the resistances R_1 and R_3 can be easily calculated due to the device geometry is known, by using the following equation:

$$R = \rho_{LSMO} \frac{L}{W \cdot t_{LSMO}} \quad \text{Eq. 4.7}$$

From the design of the three terminal structures we know the dimensions of the devices and the resistivity of the LSMO in the LRS. The values of L=140µm and W=30µm, with the LSMO resistivity of 4.8mΩ-cm with thickness of 40nm results in a resistance

value of 5.6kΩ. In addition, due to the fact that the low voltage measurements do not produce any kind of resistive switching in other parts on the track just under the gate electrode, we can assure that the symmetry of the device the R_1 and R_3 remain both with the same resistance value, i.e., $R_1=R_3$. As a result, the R_{LRS} can be rewritten as:

$$R_{LRS} = 2R_1 + R_{eq} \qquad \text{Eq. 4.8}$$

Substituting the values of R_{LRS}, R_{HRS} and R_{ratio} in equation 4.6 we can obtain the value of R_{eq} as follows:

$$R_{ratio} = \frac{R_{HRS}}{2R_1 + R_{eq}} \qquad \text{Eq. 4.9}$$

$$15 = \frac{1x10^6\Omega}{2(5.6x10^3\Omega) + R_{eq}} \qquad \text{Eq. 4.10}$$

$$R_{eq} = 55.4k\Omega \qquad \text{Eq. 4.11}$$

The resistance of the transformed area is now known. Rewriting equation 4.5 is possible to know the thickness of the LSMO layer that has been switched using the length (40µm) and the width (30µm) of the gate electrode.

$$x = t_{LSMO} - \rho_{LSMO}\frac{L}{R_{eq}\cdot W} \qquad \text{Eq. 4.12}$$

$$x = 40x10^{-9}m - 4.8x10^{-5}\Omega m\frac{40x10^{-6}m}{55.4x10^3\Omega\cdot 30x10^{-6}m} \qquad \text{Eq. 4.13}$$

$$x = 38.8nm \qquad \text{Eq. 4.14}$$

This value reveals that the volume switching achieved in the $La_{0.8}Sr_{0.2}MnO_3$ layer transforms its whole thickness which is in agreement with the observations reported before [9]. However, in that report it was stated that in layers thicker than 10nm it was difficult to achieve volume switching across the $La_{0.7}Sr_{0.3}MnO_3$ layer using the C-SPM technique. In our case, it is demonstrated that in $CeO_{2-x}/La_{0.8}Sr_{0.2}MnO_3$ bilayers devices the thin CeO_{2-x} layer acts as an oxygen reservoir promoting the oxygen ion exchange and hence the volume switching can be induced using metal electrodes.

The results shown above confirm that inducing a resistance change under the gate electrode, the conduction at the $La_{0.8}Sr_{0.2}MnO_3$ layer is modified because the whole thickness has been switched to a different resistance state. Consequently, the volume switching has been confirmed in three terminal devices based on $CeO_{2-x}/La_{0.8}Sr_{0.2}MnO_3$ bilayers.

In order to observe the repeatability of the switching, the device was continuously switched without any important degradation of the resistance ratio. The first 20 cycles are shown in figure 3.27a and 3.27b. Figure 3.27c shows the resistance ratio around 15 measured on the track after each transition of the LSMO layer under the gate electrode while figure 3.27d shows the BRS ratio to be around 10^3. It is worth noting that a small length of the track has been modified when inducing a transition compared with the total length of the track measured at low voltage which explains the small resistance ratio. Further investigation of the volume switching inside the $La_{0.8}Sr_{0.2}MnO_3$ layer and optimization of the structure's dimensions will improve this resistance ratio. These results also confirm that the conduction is performed along the $La_{0.8}Sr_{0.2}MnO_3$ track due to the transformation induced by the BRS on this layer.

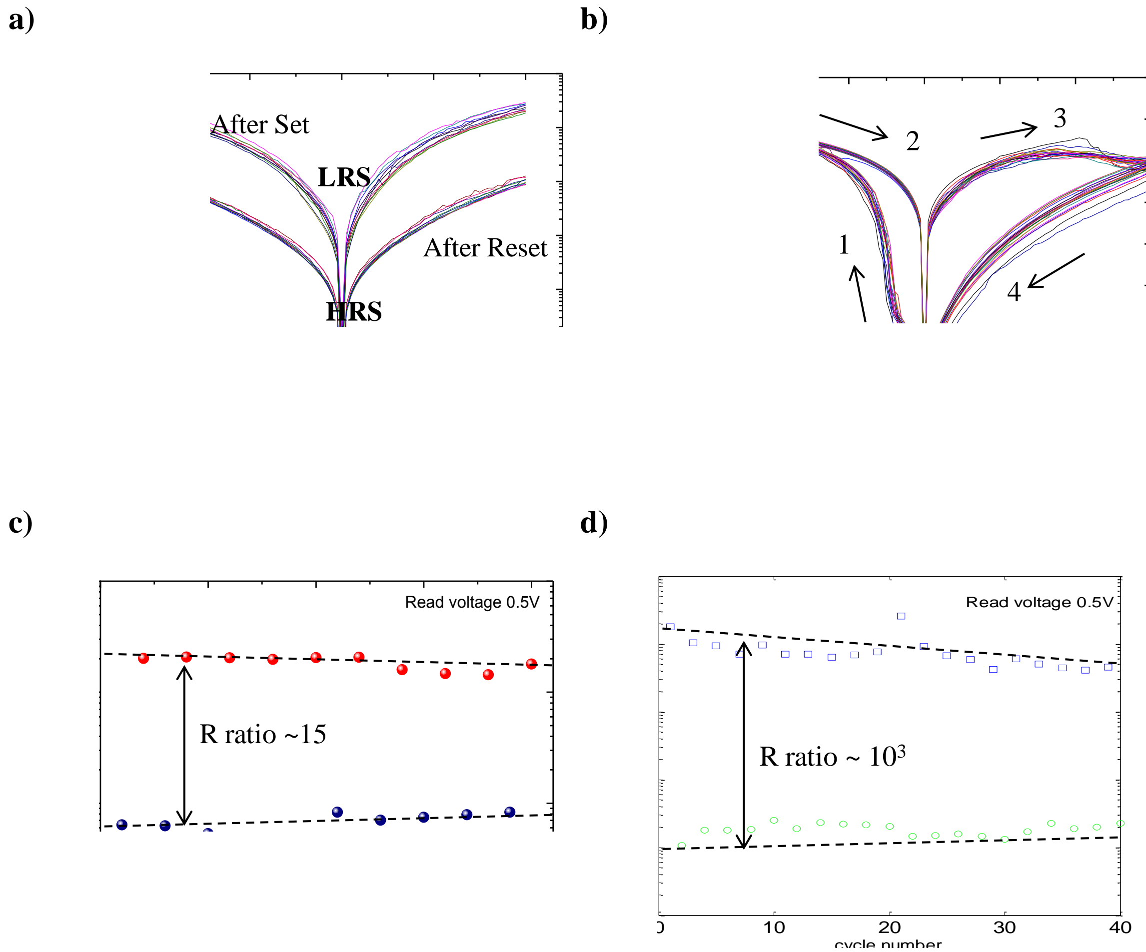

Fig. 3.27 a) Low voltage measurements performed to measure the track resistance state. b) The BRS induced on the gate electrode up to 20 cycles. Resistance ratio measured at 0.5V in c) the track resistance ratio is around 30 while d) the BRS induced on the gate electrode is around 10^3.

3.3.2 Conclusions about volume switching in bilayer devices

In the last section, volume switching in $CeO_{2-x}/La_{0.8}Sr_{0.2}MnO_3$ bilayer devices has been demonstrated. It was also shown that the volume switching is produced across the whole thickness of the $La_{0.8}Sr_{0.2}MnO_3$ layer.

A three-terminal device is proposed where the resistance along the track can be modulated through a gate electrode. The volume switching induced under the gate electrode modifies the current conduction along the track. The high resistance state measured in the tack just after the electroforming process indicates that no breakdown related to this initial step occurs in the CeO_{2-x} layer, In addition, the volume switching demonstrates that resistive switching is homogeneously extended over the $La_{0.8}Sr_{0.2}MnO_3$ layer and it is not produced by localized thin filaments in the switching

layer. However, deeper investigation has to be performed in these three-terminal devices to improve the resistance ratio when it is measured along the $La_{0.8}Sr_{0.2}MnO_3$ track.

3.4 Evaluation of the resistive switching in vertical devices.

In previous section, the RS characteristics have been measured in lateral devices where the conduction in the $La_{1-x}Sr_xMnO_3$ layer is produced transversally between the metal electrodes. In this section, we will present a first approach to the study of resistive switching in devices using a conductive Nb:STO substrate as a counter electrode so that we can apply the electric field vertically across the $La_{1-x}Sr_xMnO_3$ layer in a metal-oxide-metal (MOM) vertical configuration.

Here, after the deposition and growth of the $La_{1-x}Sr_xMnO_3$ layers on conductive Nb:STO substrate, their physical properties are investigated through some of the characterization techniques presented before in chapter 2. In addition, the RS characteristics will be analysed in single $La_{0.8}Sr_{0.2}MnO_3$ and $La_{0.8}Sr_{0.2}MnO_3/CeO_{2-x}$ bilayer devices.

3.4.1 Characterization of $La_{0.8}Sr_{0.2}MnO_3$ layers on conductive Nb:STO substrate

Conductive $SrTiO_3$ doped Nb 0.05wt% (Nb:STO) with resistivity value of 70mΩ·cm at 300K, available from Crystec, was used as substrate to grow epitaxial $La_{08}Sr_{0.2}MnO_3$. Similar to the process described in chapter 2, substrate thermal treatment and BHF cleaning was performed to this substrate in order to obtain the desired TiO_2 termination to favor the epitaxial growth of the $La_{08}Sr_{0.2}MnO_3$ layer [64]. In addition, the same CSD deposition method described in the same chapter was used to grow the $La_{08}Sr_{0.2}MnO_3$ layers.

Figure 4.28a show the AFM image of the grown layer where the root mean square of 3.2nm is observed. In addition, figure 3.28b shows the X-ray pattern around the (003) reflection where we can observe the peak related to $La_{08}Sr_{0.2}MnO_3$ (003) at θ=72.9º. The inset in this figure shows that no other peaks related to different phases are presented.

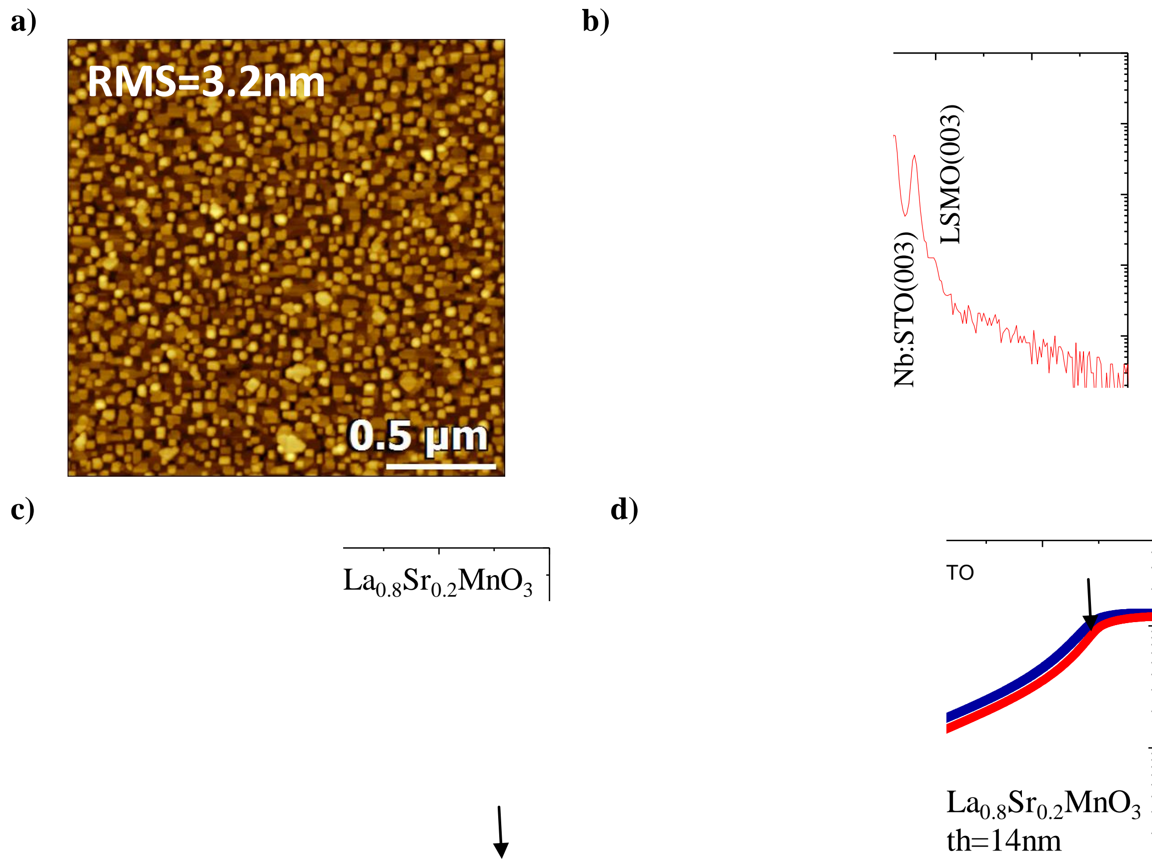

Fig. 3.28. Physical characterization of $La_{0.8}Sr_{0.2}MnO_3$ grown on conductive Nb:STO substrate. a) AFM image and b) resistivity measurements comparison with a layer grown on insulating STO.

Fig 3.28c shows the comparison between two $La_{08}Sr_{0.2}MnO_3$ layers grown on STO and Nb:STO substrates. Although the magnetization observed in the layer grown on the latter substrate is slightly lower, the T_C is similar in both layers. Moreover, fig. 3.28d compares the resistivity where the metal-insulator transition (MIT) happens at the same value of temperature.

Regarding bilayer systems, a thin CeO_{2-x} layer (10nm) was deposited by ALD on $La_{0.8}Sr_{0.2}MnO_3$ (14nm)/Nb:STO as described before in chapter 2. Due to the fact that the same conditions of ALD were used with this kind of samples, we assume that any modification of the physical properties was produced, in line with the previous results.

The Au, Ag and Pt electrodes, defined by photolithography, were separately sputtered on the same sample (fig. 3.29). They are 100x100µm square-shaped with separation of 100µm from one to another. However, the deposition conditions had not been optimized yet when microfabrication of this kind of devices so that the oxygen content in the layers could have been modified before the evaluation of the RS.

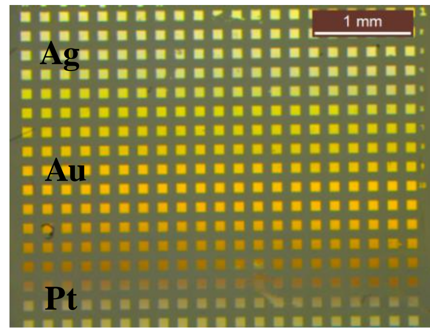

Fig. 3.29 Ag, Au and Pt electrodes deposited by sputtering on top of $La_{0.8}Sr_{0.2}MnO_3$/Nb:STO and CeO_2/ $La_{0.8}Sr_{0.2}MnO_3$/Nb:STO samples

3.4.2 Resistive Switching in $La_{0.8}Sr_{0.2}MnO_3$ layers and CeO_{2-x}/ $La_{0.8}Sr_{0.2}MnO_3$ bilayers in vertical devices

The RS properties investigated in $La_{0.8}Sr_{0.2}MnO_3$ layers and $CeO_{2-x}/La_{0.8}Sr_{0.2}MnO_3$ bilayers on conductive Nb:STO are presented in this section. The resistive switching characteristics were investigated applying systematic voltage sweeps where the positive bias is defined by the current flowing from the $La_{0.8}Sr_{0.2}MnO_3$ layer to the conductive Nb:STO substrate in a vertical way. The substrate, 0.5mm thick, is electrically connected through its back side to a conducting metal plate attached with silver paint in order to use it as the counter electrode. Although the evaluation of the RS was performed using the three different metal electrodes, the results presented here are all related to the Ag electrodes which demonstrated to have better performance.

First, no sign of RS was found in Ag/$La_{0.8}Sr_{0.2}MnO_3$/Nb:STO vertical devices similar to what we reported in lateral devices. On the other hand, BRS behavior is achieved when a complete voltage cycle is performed when a metal probe is placed directly on $La_{0.8}Sr_{0.2}MnO_3$ layer (figure 3.30). At forward bias, the current increases following a rectifying conduction until saturation (branch 1). During the voltage back excursion, the current stays at smaller values indicating that a transition from LRS to HRS (Reset) has taken place (branch 2). At reverse bias, the current sharply increases at small voltage values (branch 3) and the current is kept high during the negative voltage back excursion (branch 4). In this branch, the current has slightly increased indicating that a transition from HRS to LRS has taken place. From the observation of the curves in figure 3.30 it is difficult to mark a Vset and Vreset at which the transitions are taking place. However, the LRS and the HRS are clearly achieved.

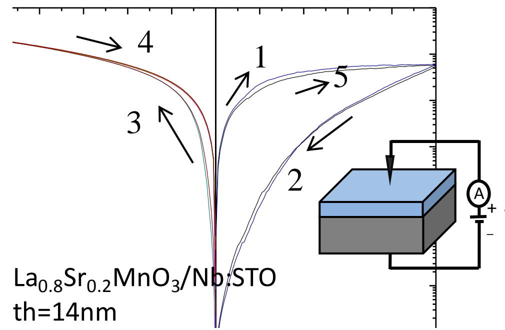

Fig. 3.30. BRS induced in vertical device probe/$La_{08}Sr_{0.2}MnO_3$/Nb:STO

A remarkable polarity effect is seen in the HRS I-V curves shown in figure 3.30 which are probably related to the asymmetry of the structure. At forward bias, after the Reset transition, the device remains in the HRS during the voltage back excursion (branch 2). On the other hand, at small reverse bias the conduction sharply increases indicating a Set transition which is not clearly located at any particular Set voltage (branch 3). There are two possible reasons which may explain this behavior. On one hand, the transition could happen at very small voltages which are not measured due to the resolution we used during the evaluation of the devices (steps of 0.1V). On the other hand, the interface $La_{0.8}Sr_{0.2}MnO_3$/Nb:STO could be playing an important role during the evaluation at reverse bias of the RS where the conduction at negative voltage is possibly dominated by this interface.

Moreover, repeatability was tested by applying consecutive voltage sweeps and the corresponding resistance states were read at 1V. Figure 3.31a shows these consecutive loops while figure 3.31b shows the resistance values plotted as a function of cycle number. In this figure, a resistance ratio of the order of 10^2 has been demonstrated over 50 cycles indicating good stability of the RS in these devices. Figure 3.31c shows the cumulative probability of these resistance values.

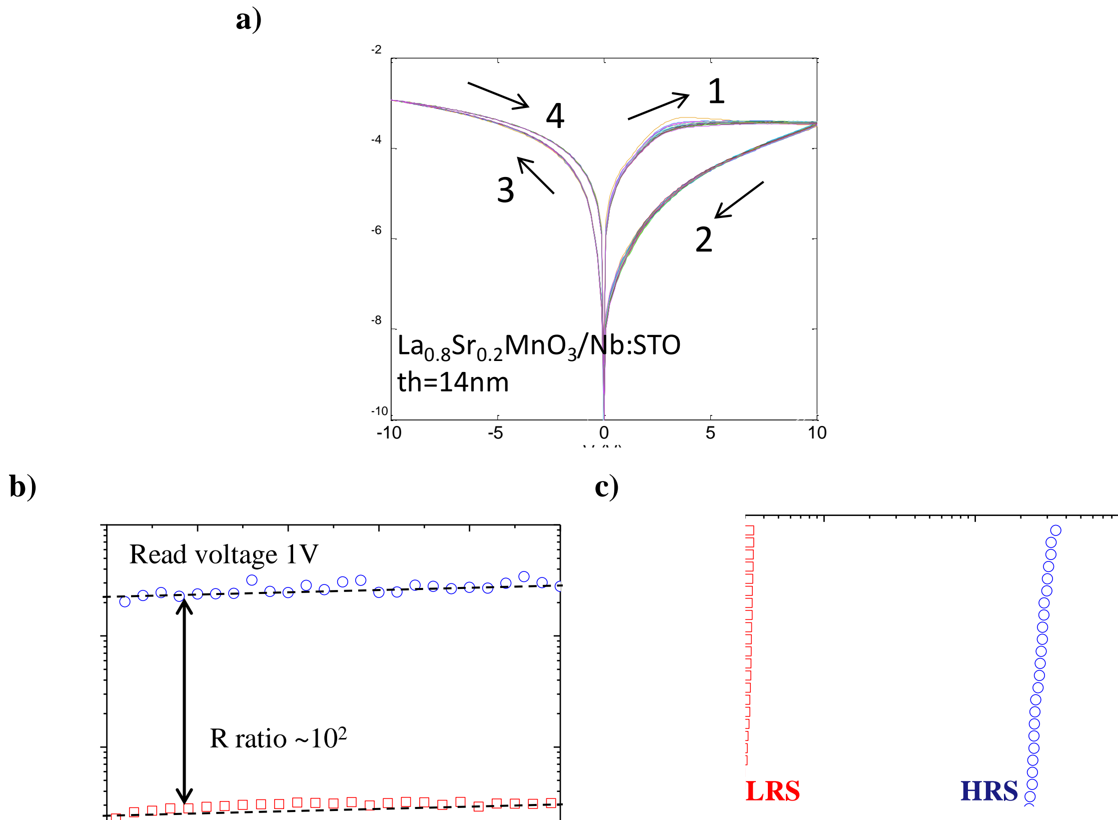

Fig. 3.31 a) Repeatability test in vertical devices. a) BRS induced over 50cycles, b) resistance ratio is in the order of 10^2 when resistance is read at 1V, c) cumulative probability of the resistance values

On the other hand, similar vertical configuration was used to measure Ag/CeO_{2-x}/ $La_{0.8}Sr_{0.2}MnO_3$/Nb:STO bilayer devices to obtain the RS characteristics with the measurement probe placed on top of the metal electrodes. Figure 3.32 shows the measured I-V curves when voltage was applied between ±10V. Here, an electroforming is needed to induce the BRS when starting from the pristine state. In the figure, branches 1 and 2 (electroforming branches) shows high resistance state which is turned to a less resistive state by applying positive voltage. The following reverse bias produces a transition from HRS to LRS which remains during the voltage back excursion (branches 3-4). Then, the following forward bias maintains the LRS (branch 5) until the voltage back excursion in positive voltage produces a different current trajectory at the HRS which indicates that a Reset transition has been produced.

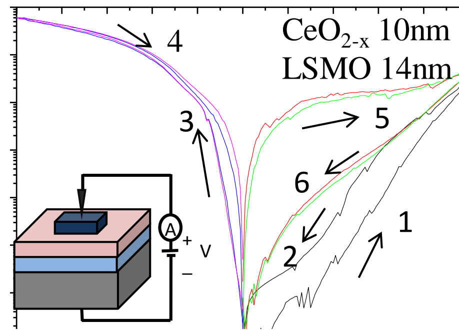

Fig. 3.32. BRS induced in vertical Ag/CeO_{2-x}/$La_{0.8}Sr_{0.2}MnO_3$/Nb:STO devices.

The I-V curves suggest the same RS behavior in $La_{0.8}Sr_{0.2}MnO_3$ layers and CeO_{2-x}/ $La_{0.8}Sr_{0.2}MnO_3$ bilayers because the shape of the curves and the values of the measured current are very similar, except for the electroforming needed in the latter devices. The BRS is explained using the oxygen ion exchange mechanism proposed for both $La_{0.8}Sr_{0.2}MnO_3$/Nb:STO and Ag/CeO_{2-x}/$La_{0.8}Sr_{0.2}MnO_3$/Nb:STO lateral devices. In the case of the bilayer devices, the CeO_{2-x} acts as an oxygen reservoir which decouples the metal electrode from the RS effect. However, the introduction of the Nb:STO substrate, specifically at the interface $La_{0.8}Sr_{0.2}MnO_3$/Nb:STO seems to introduce differences in the RS phenomena with respect to the one observed in lateral devices. Further work should be done in order to elucidate the origin of these differences.

3.4.3 Conclusions about resistive switching in vertical devices

The evaluation of the RS properties in vertical MOM devices has been presented in this section. The $La_{0.8}Sr_{0.2}MnO_3$ layers were deposited on conductive Nb:STO substrate in order to use it as the counter electrode. Besides, a CeO_{2-x} layer was deposited on top to form the bilayer devices. Finally, metal electrodes were sputtered on top to form metal/$La_{0.8}Sr_{0.2}MnO_3$/Nb:STO and metal/CeO_{2-x}/$La_{0.8}Sr_{0.2}MnO_3$/Nb:STO devices.

Regarding the evaluation of vertical metal/$La_{0.8}Sr_{0.2}MnO_3$/Nb:STO structures, the RS properties were not observed when the measurement probe was located directly at the metal electrode. Similar to what was observed during the evaluation of RS in single $La_{0.8}Sr_{0.2}MnO_3$, the BRS was produced only when the probe was directly located on the oxide layer. On the other hand, the BRS was also achieved in metal/CeO_{2-x}/

$La_{0.8}Sr_{0.2}MnO_3$/Nb:STO bilayer devices. However, in these devices, an electroforming process is required in agreement with the results reported in lateral devices.

After electroforming, the BRS induced between ±10V in both samples shows similar curve-shape and resistance values, and no significant difference is found with respect to the results reported in single Ag/$La_{0.8}Sr_{0.2}MnO_3$/Nb:STO vertical devices. We can conclude that the switching layer is the $La_{0.8}Sr_{0.2}MnO_3$. In addition, comparing with the results reported in lateral devices, we infer that the $La_{0.8}Sr_{0.2}MnO_3$/Nb:STO interface plays an important role in the conduction characteristics of this kind of devices and besides it explains the strong asymmetry observed between positive and negative bias voltage. However, deeper investigation is required in order to fully understand the influence of this interface.

3.5 Evaluation of the resistive switching in other different perovskite-like oxides: the case of $YBa_2Cu_3O_7$ cuprates

The yttrium barium copper oxide $YBa_2Cu_3O_7$ (YBCO) has been widely studied for its excellent superconductivity properties since it was discovered as a high temperature superconductor material with critical temperature around 93K [119]. The YBCO has a perovskite structure which is formed by the stack of Cu-O planes lying normal to the c-axis direction, sandwiched by Y-O and Ba-O planes with a metal-insulator transition also linked to oxygen doping. For this reason, YBCO cuprate layers will be also used here to investigate the RS at device level in a similar manner to $La_{1-x}Sr_xMnO_3$ devices.

Recently, during the development of this work, at the Superconducting Material and Large Scale Nanostructures (SUMAN) department of the ICMAB, the research on RS properties on YBCO has been conducted through C-SFM approach [59]. Similar to LSMO layers, oxygen ion exchange through a metal-insulator transition has been proposed as the switching mechanism responsible for the switching behaviour.

The YBCO samples used in this work to evaluate the resistive switching were all synthesized and characterized at the SUMAN group. These layers were grown following a CSD route on treated $LaAlO_3$ (LAO) substrates using metal-trifluoracetates (metal-TFA) as chemical precursors. After final thermal annealing at 810ºC under 10^{-4} bar of O_2 and oxygenation step at 450ºC, the resulting YBCO layers are grown fully

epitaxial and with high superconducting properties with 50nm in thickness. For more details of the deposition and growth of these thin YBCO layers see ref. [120]–[122].

3.5.1 Characterization of $YBa_2Cu_3O_7$ cuprate layers

Structural and physical properties were evaluated in YBCO layers using the same characterization methods followed for the evaluation of the LSMO layers. First, Atomic Force Microscopy (AFM) was performed on as grown YBCO layer in order to determine its flatness. Figure 3.33 shows the image of the YBCO layer surface where a RMS=8nm is observed.

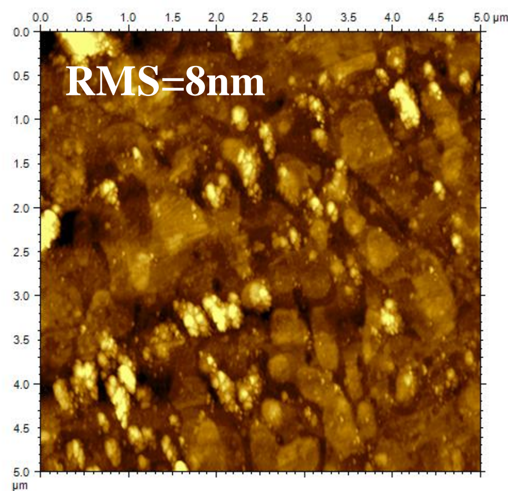

Fig. 3.33. AFM image of YBCO layer surface with RMS=8nm. Courtesy of J.C. Gonzalez

The structure of the YBCO layer was investigated through X-ray diffraction. Figure 3.34a shows the 2θ scan performed with the Rigaku Rotaflex RU 200B diffractometer. In this figure, it is observed that the YBCO layer is mainly (00*l*) oriented, indicating c-axis preferred orientation of the YBCO, but secondary phases have also been detected. They are indexed to Y_2O_3 and CuO compounds. From previous studies in the group, it is known that these phases are intermediate products that have not been completely transformed to c-axis YBCO during the high temperature growth process [123]. However, such secondary faces will not be detrimental for other physical properties and T_C of ~90K and J_C of ~3MA/cm^2 Figure 3.34b shows in plane texture from Φ-scan demonstrating high quality biaxial texture with ΔΦ(102)=1.3º which is attributed to high epitaxial growth of the YBCO layer.

a) **b)**

Fig. 3.34. a) XRD pattern of YBCO layer showing high intensity of (00l) YBCO reflections. Although secondary phases related to Y_2O_3 and CuO are also detected, they will not be detrimental for other physical properties. Image courtesy of J.C. Gonzalez. b) Φ-scan of YBCO layer demonstrating high epitaxial growth of the layer. Courtesy of M. Coll.

Resistivity as a function of temperature was measured in order to determine the transition from metallic to superconducting states. Figure 3.35 shows a typical ρ(T) transition at zero applied magnetic field where an ohmic behaviour is observed above T_C=93K. The curve also shows that at very low temperatures, below T_C, the YBCO is in the superconductor state. The measurements indicate that at room temperature (300K), the value of the resistivity in this kind of thin layers is around 330μΩ-cm which indicates that the YBCO is in the metallic state.

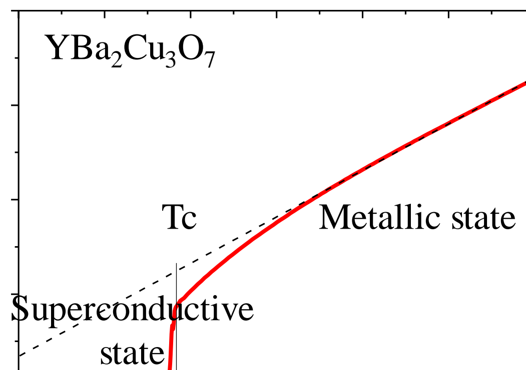

Fig. 3.35. Resistivity as a function of temperature measured in $YBa_2Cu_3O_7$ layer shows a transition between the metallic-ohmic to the superconductive state at a Tc around 93K. (Courtesy of A. Stangl)

An important parameter for the RS evaluation of YBCO layer is the oxygen content. This parameter strongly modifies the crystallographic structure and the mobile charge carrier concentration. Figure 3.36 [124] presents a generic phase diagram of high-

temperature superconductors (HTSC) showing the modification of the critical temperature (T_C) as a function of the carrier density (doping, *p*). At low doping, we have an insulating antiferromagnetic phase (AFM) which gradually disappears upon increase of doping, allowing a metallic phase presenting superconductivity (SC) around 0.05 doping level at low temperature. Some other phases presents in this figure are the pseudogap (PG) semiconducting phase below the T^* temperature, the marginal Fermi level (MFL) phase between the T^* and T_f temperatures and the true Fermi liquid (FL) phase The LRS and HRS related to the RS observed in this kind of materials at 300K are related to the PG semiconducting (insulating) and MFL (metallic) phases.

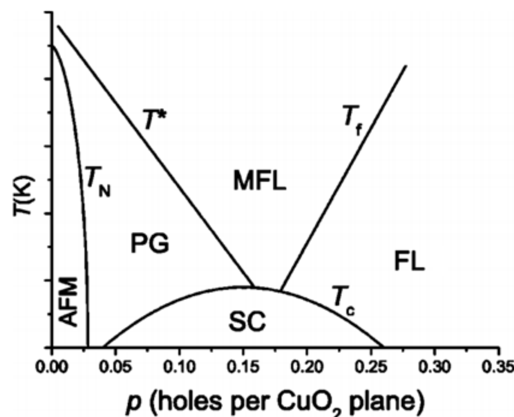

Fig. 3.36. Critical temperature Tc of $YBa_2Cu_3O_{7-x}$ as a function of the oxygen content x [125]

In order to confirm the doping state of the YBCO used to evaluate the RS behaviour, the transition temperature was determined measuring the susceptibility (χ_{DC}) as a function of temperature. According to figure 3.36, a shift in the Tc value indicates a change in the oxygen content of the YBCO layer which modifies its resistivity as well. Figure 3.37 shows the magnetization measurements performed on the same YBCO sample at three different stages of the fabrication process. First, in the as grown sample, a Tc value around 90K is measured. Then, in order to define the metal electrodes, a standard photolithography process followed by metal sputtering were performed to this sample. The susceptibility is measured again showing an important decrease of the Tc value down to 40K which indicates that the oxygen content of the YBCO sample has been modified during the fabrication process. In order to recover the optimum state of the metallic phase of YBCO suitable for the RS behaviour, the sample was annealed at 450ºC for 1h in oxygen atmosphere similar to the post-annealing thermal profile after metal evaporation (showed in chapter 2). This thermal annealing has demonstrated to improve the oxygen content of the YBCO layers. The magnetization curve measured

after this thermal annealing indicates that the superconducting properties were recovered with values of Tc around 90K similar to what was measured in the as grown sample. It is worth noting that the Tc=90K of these layers of 50nm is comparable with the value measured in thicker layers. We can conclude from this analysis that the oxygen content in YBCO layers is very sensible to the fabrication process which has to be optimized in order to obtain reliable measurements when the RS properties will be evaluated.

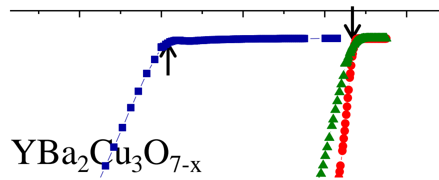

Fig. 3.37. DC susceptibility curves performed to an as growth YBCO sample and after to a metal sputtering demonstrate that Tc is shifted which indicates a change in the oxygen content in the YBCO. A thermal annealing process in O_2 ambient is performed to recover the initial state of the YBCO layer.

3.5.2 Resistive switching in $YBa_2Cu_3O_{7-x}$- based lateral devices

The RS curves presented here were measured as part of the collaboration work developed together with other members of the SUMAN group. The RS characteristics have been evaluated in YBCO layers through Pt, Ag and Au metal electrodes once the optimum oxygen content has been restored in YBCO layers. However, BRS was only induced when lateral Au/YBCO/Au and Ag/YBCO/Ag were evaluated. The results presented here are only related to Ag/YBCO/Ag devices just for convenience although measurements using Au as metal electrode showed similar behaviour. The lateral devices were measured by applying successive voltage sweeps between the Ag electrodes. Figure 3.38 shows the BRS induced in these devices. First, positive voltage was applied between the electrodes up to 3V which produces a transition from the LRS to the HRS (branch 1). This state is maintained during the voltage back excursion (branch 2). When the device is reverse biased up to -3V, a Set transition is produced (branch 3). During the voltage back sweep up to 0V the device remains in the initial LRS. As a result, the BRS is demonstrated in Ag/YBCO/Ag devices.

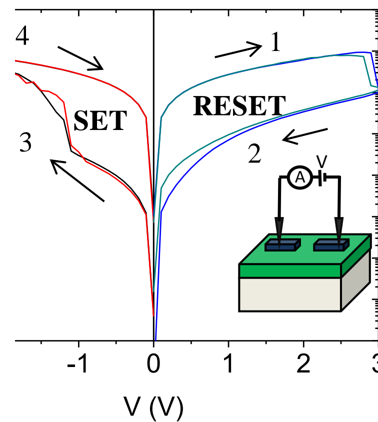

3.38. BRS induced in Ag/YBCO/Ag lateral devices when voltage is applied on metal electrodes.

According to the figure 3.38, the first transition is produced from the LRS to the HRS which indicates that the YBCO layer is in the metallic state at the pristine condition. In addition, different from what was observed during the evaluation of the RS in $La_{1-x}Sr_xMnO_3$ devices, the BRS has been achieved when measurement probes are placed on Ag and Au electrodes. The proposed mechanism responsible of the RS in these devices is the same oxygen ion migration which is induced by the electric field under one metal electrode. In the case of the metal/YBCO/metal devices, it is possible that oxygen ions could not be exchanged between the YBCO and the ambient due to the fact that metal electrodes would act as a barrier. The RS could be achieved through the diffusion of oxygen ions from the YBCO layer to a poorly oxygenated YBCO interlayer which would be formed at the interface metal/YBCO. This thin layer would play the same role of the CeO_{2-x} layer in CeO_{2-x}/LSMO bilayer as an oxygen reservoir enabling the RS in this kind of devices. However, evidence of the formation of this thin layer has not been obtained through characterization methods of materials yet. Moreover, the observation of the sharp Reset transition denotes that the oxygen ions are not associated/disassociated as required for the exchange with the ambient; instead, they are moved to/from the YBCO in agreement with the observations in $CeO_{2-x}/La_{1-x}Sr_xMnO_3$ bilayers. Second, this movement produces low voltage operation of the device due to the fact that the oxygen ions have not to be exchanged with the ambient being only moved from one layer to another. Finally, when the voltage sweeps are increased to ±6V, CRS is observed in Ag/YBCO/Ag and Au/YBCO/Au devices (figure 3.39). However, different from the $CeO_{2-x}/La_{1-x}Sr_xMnO_3$ bilayers, an electroforming process is not needed to induce the RS behaviour in YBCO devices.

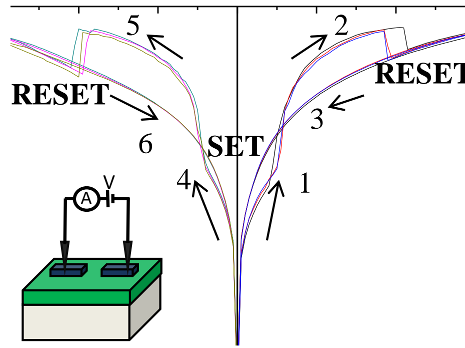

Fig. 3.39. Complementary Resistive switching measured in metal/YBCO/metal lateral devices when Ag and Au are used as metal electrodes.

In figure 3.39 the first positive sweep from 0V to 6V is induced on the device just after it was switched from LRS to a HRS during a Bipolar switching cycle. For this reason, the branch 1 begins from a HRS and it switch to a LRS around 1.2V. The voltage sweep continues increasing and the device is maintained at the LRS until a Reset transition is observed after 4V (branch 2). The HRS is maintained in branch 3 during the voltage back excursion. At the following reverse bias, at branch 4, a Set transition is achieved around -1.2V. Moreover, this state is changed when a following transition to LRS happens at around -4V in branch 5. The device is in this state during the negative voltage back excursion (branch 6). The CRS measured when the sweep voltage is increased indicates that the area under both measurement probes is switching alternatively according to the polarity of the voltage sweep in agreement with the observation in Ag/CeO_{2-x}/$La_{0.8}Sr_{0.2}MnO_3$/CeO_{2-x}/Ag devices.

The repeatability of the BRS behaviour in Ag/YBCO/Ag devices was investigated over 50 cycles. In this case, instabilities and fast degradation of the hysteresis behaviour during the measurements in these devices did not allow investigate further the repeatability. Figure 3.40a shows the curves where BRS is confirmed. Figure 3.40b shows the resistance ratio when both the LRS and the HRS are measured at 0.5V. During the first cycles, the resistance ratio is around 10^2 but it decreases half an order of magnitude over the following 50 cycles. A faster degradation indicated by the slope of the line connecting the points at the HRS produces the decrease of the resistance ratio. In addition, a wider distribution of this state is observed in figure 3.40c while a more stable LRS is observed. The distribution of the Set and Reset transitions achieved during the voltage excursions between +4V and -5V are plotted in figure 3.40d. The

sweep voltage had to be increased in order to assure that the device reaches the Reset transition as shown in this figure where a larger distribution at the Vreset is observed.

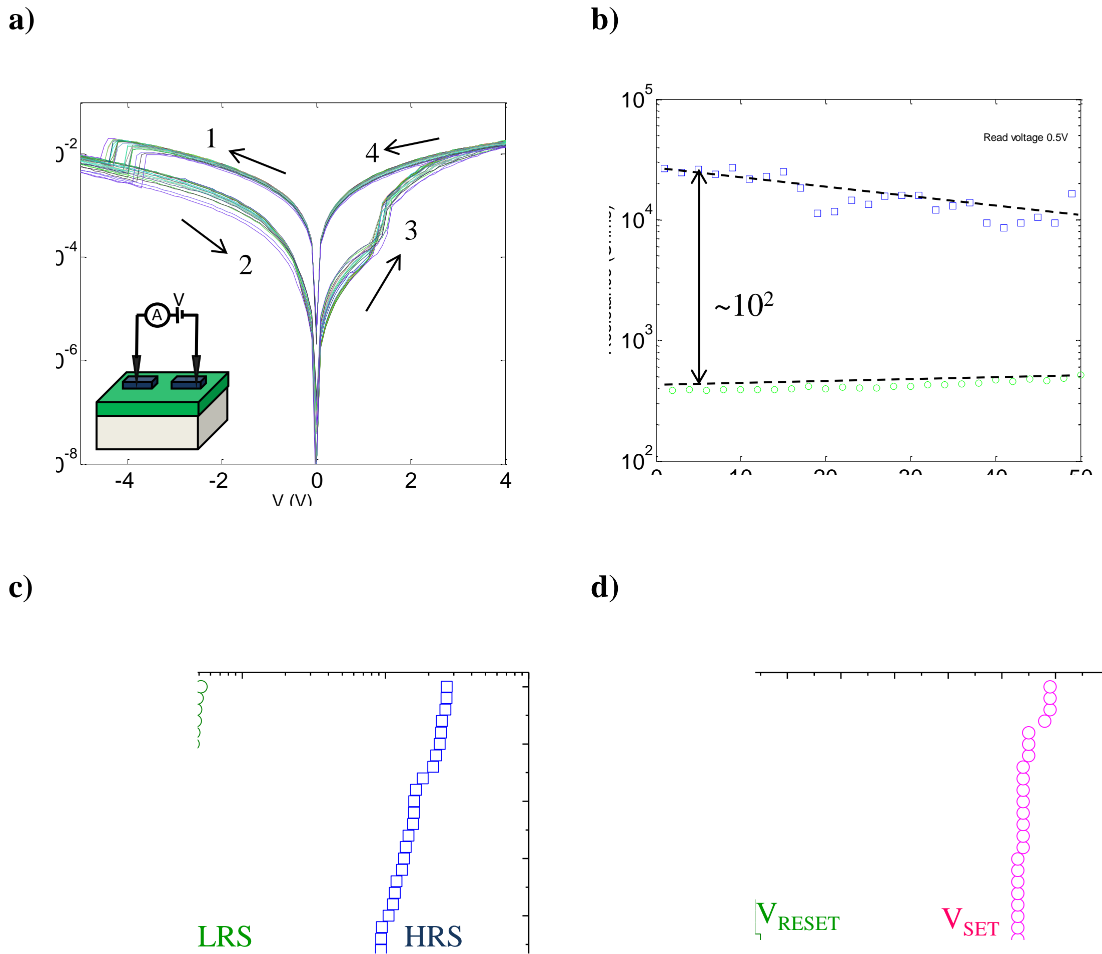

Figure 3.40 a) The first 50 cycles measured on the same Ag/YBCO/Ag device showing the repeatability of the BRS. b) The resistance ratio measured at 0.5V is ~10^2 at the first sweeps and decreases over the following cycles. c) A higher distribution is observed at the HRS for these cycles. d) The sweep voltage was increased between -5V and 4V to assure the Reset transition where a higher distribution is observed.

3.5.3 Conclusions about resistive switching in $YBa_2Cu_3O_7$ devices

The thin $YBa_2Cu_3O_7$ layer deposited on insulating LAO substrate was used to investigate the RS characteristics after metal electrodes were sputtered on top to form the metal/YBCO/metal lateral devices. It was demonstrated through susceptibility measurements that the Tc of the YBCO layer is modified during the fabrication process indicating a change of the oxygen content in the layer. The optimum oxygen level was

achieved again by performing a thermal annealing at 450ºC in oxygen ambient after device fabrication.

The BRS was demonstrated in these devices when they were biased only using Ag and Au metal electrodes between 4V and -5V. The first voltage sweep produces a transition from LRS to HRS indicating that the YBCO is in the metallic state at the pristine state. Moreover, when the voltage sweep is increased, CRS has been measured in the same devices. It was speculated that a thin poorly oxygenated YBCO interlayer is formed at the interface metal/YBCO which acts as an oxygen reservoir similar to the CeO_{2-x} layer in $CeO_{2-x}/La_{0.7}Sr_{0.3}MnO_3$ bilayer devices. Further analysis of the interface Ag/YBCO and Au/YBCO has to be performed in order to confirm the formation of such thin layer and determine the conditions to improve the RS behaviour.

On the other hand, the resistance ratio measured for BRS indicates degradation of the RS behaviour of half an order of magnitude at the HRS which is observed through the analysis of the distribution of the resistance states and the voltage transitions.

Finally, the RS behaviour in thin YBCO layer has been explained by the same mechanism of the oxygen ion exchange through a metal-insulator transition which is proposed to be responsible of the RS in this kind of perovskite oxides.

Chapter 4
General conclusions

In this thesis, we have explored the resistive switching phenomenon in micrometric devices for non-volatile memory applications. Basically, we have investigated the switching properties of the perovskite-type $La_{1-x}Sr_xMnO_3$ complex oxide in memristive metal-oxide-metal configuration. In addition, we have proposed a three-terminal device based on the control of the volume switching by a gate electrode.

Based on the previous knowledge of the SUMAN group, we have employed a metal-organic decomposition (MOD) route, derived from chemical solution deposition (CSD) method, to grow epitaxial layers on insulating $SrTiO_3$ (STO) substrates. The growth conditions of $La_{1-x}Sr_xMnO_3$ layers have been optimized in order to obtain flat epitaxial thin films with excellent physical properties.

Moreover, it was demonstrated that the thickness of the grown layers can be modified by changing the molar solution concentration of the deposited solution. In this regard, we have achieved thin layers between 4-42nm in thickness with T_C kept at 360K, similar value to that observed in bulk $La_{0.7}Sr_{0.3}MnO_3$ materials.

In addition, we have changed stoichiometry (Sr_x content) of $La_{1-x}Sr_xMnO_3$ in order to find the most suitable composition for resistive switching. In this case, the studies were conducted on samples with stoichiometry of x=0.15, 0.2, 0.25 and 0.3. It was found that T_C and T_{MI} decrease when the Sr content decreases. Modification of the magnetization properties and electronic transport were attributed to introduction of Sr^{2+} into La^{3+} cation sites which is balanced with the conversion of Mn^{3+} to Mn^{4+}. Although some effects due to oxygen vacancies could be observed specially for $La_{0.85}Sr_{0.15}MnO_3$. The created Mn^{4+} combines with Mn^{3+} and O^{2-} ions and creates a Mn^{3+}-O^{2-}-Mn^{4+} bond which modulates the electronic conduction in La_{1-x} Sr_xMnO_3. As a result, it was found that $La_{0.8}Sr_{0.2}MnO_3$ layers have a T_{MI}=303K, the lowest value to maintain the metallic behaviour at room temperature.

Moreover, we have employed microelectronic techniques such as photolithography, etching, metal evaporation and sputtering to fabricate memristor devices studied in this

thesis. Optimization of these different techniques has been performed along the work with the objective to maintain the initial physical properties of the layers. In this regard, after successive sputtering of metal electrodes, magnetization of $La_{1-x}Sr_xMnO_3$ layers has decreased attributed to important changes in the oxygen content mainly associated to the creation of oxygen vacancies. The sputtering of Ag electrodes has been optimized to maintain as low as possible these changes which play an important role during the evaluation of the resistive switching phenomena. In addition, we have determined the etching rate of $La_{1-x}Sr_xMnO_3$ and CeO_{2-x} layers when this process was performed with the reactive ion etcher (RIE).

Furthermore, evaluation of the resistive switching has been performed through linear voltage sweeps to generate I-V curves. First, bipolar resistive switching has been induced in metallic $La_{0.8}Sr_{0.2}MnO_3$ layers when the measurement probes were located directly on top of the layer. Since any remarkable switching was observed when the probes were located on top of metal electrodes, we suggested a possible mechanism based on the oxygen ion exchange through the MIT transition. According to the direction of the applied electric field, oxygen ions are released from the layer and they are exchanged with the ambient, enabling firstly a Reset transition. This exchange is strongly blocked by the metal electrodes being the principal reason of the lack of hysteresis. On the other hand, applying the opposite voltage polarity, the oxygen ions are brought back to the $La_{0.8}Sr_{0.2}MnO_3$ layer where a Set transition is observed. Interestingly, the area where the resistive switching is taking place is only the one in the $La_{0.8}Sr_{0.2}MnO_3$ layer under the probe where the first Reset transition is produced due to the fact of (i) direction of the applied electric field and (ii) the voltage drop enhanced at the area of high resistance state. Moreover, it has been presented that the resistive switching characteristics such as the Vset, Vreset and resistance ratio can be tuned by changing the thickness and the stoichiometry of the $La_{1-x}Sr_xMnO_3$ layers. In addition, in this probe/$La_{0.8}Sr_{0.2}MnO_3$/probe lateral configuration, multilevel resistive switching has been demonstrated by controlling the V_{max} applied during the voltage sweep.

In order to fully implement the memristor devices as suitable devices for non-volatile memory applications, the use of metal electrodes has been successfully achieved by introducing a thin CeO_{2-x} layer between the $La_{1-x}Sr_xMnO_3$ layer and the metal electrodes. This thin CeO_{2-x}, layer, deposited by Atomic layer Deposition (ALD) method, acts as an oxygen reservoir promoting the interchange of oxygen ions

modifying the resistive switching properties of the $La_{1-x}Sr_xMnO_3$ layer. Further characterization of the $CeO_{2-x}/La_{0.8}Sr_{0.2}MnO_3$ bilayer system demonstrate that the physical properties of the $La_{0.8}Sr_{0.2}MnO_3$ layers were not modified, indicating that combining CSD and ALD deposition methods are compatible for the fabrication of memristor devices.

In this regard, evaluation of the bipolar resistive switching was performed on Ag/CeO_{2-x}/$La_{1-x}Sr_xMnO_3$/CeO_{2-x}/Ag lateral devices. Firstly, the same CeO_{2-x} layer was deposited to form the Ag/CeO_{2-x}/Ag lateral devices. In this case, no resistive switching characteristics were induced when the evaluation was performed applying ±10V indicating that no metallic filaments are formed inside of the CeO_{2-x} layer so that no Ag^+ ions diffusion took place into the layer. On the other hand, regarding Ag/CeO_{2-x}/$La_{1-x}Sr_xMnO_3$/CeO_{2-x}/Ag lateral devices, an electroforming process is necessary before to induce the bipolar resistive switching. This electroforming process usually induced at +5V applied on devices in the pristine state, turns the memristor from a very high insulating behaviour to an intermediate resistance state without reaching the low resistance state. At the following lower voltage sweeps (±3V), the bipolar resistive switching is achieved. These results demonstrate not only we have reproduced successfully the bipolar resistive switching behaviour at device level but also the modification of the switching properties. For instance, the Set and Reset transitions were produced between ±3V while the repeatability performed over 100 cycles demonstrate resistance ratio of ~10^4.

Contrary to what was observed during the evaluation of probe/$La_{0.7}Sr_{0.3}MnO_3$/probe where no resistive switching behaviour was induced, in Ag/CeO_{2-x}/$La_{0.7}Sr_{0.3}MnO_3$/CeO_{2-x}/Ag bilayer devices, bipolar resistive switching has been reproduced in agreement with the measurements performed with the C-SPM system.

Moreover, complementary resistive switching has been induced in the same Ag/CeO_{2-x}/ $La_{1-x}Sr_xMnO_3$/CeO_{2-x}/Ag lateral devices. This behaviour has been achieved when we increased the V_{max} during the voltage sweep. Contrary to what happens in bipolar resistive switching, complementary switching involves both junctions alternatively which are both turning to Set and Reset during operation. Finally, it has been demonstrated that bipolar and complementary resistive switching behaviour can coexist in the same device by controlling the applied voltage sweep.

Furthermore, one of the most important results achieved in this thesis work, has been the demonstration of the volume switching in Ag/CeO_{2-x}/$La_{0.8}Sr_{0.2}MnO_3$/CeO_{2-x}/Ag bilayer devices. It was shown that volume switching is produced across the whole 40nm thickness of the $La_{0.8}Sr_{0.2}MnO_3$ layer. We have taken advantage of this phenomenon to propose a three-terminal device where the resistance along the track can be modulated through a gate electrode. The volume switching induced under the gate electrode modifies the current conduction along the track according to its actual resistance state. The high resistance state measured in the track just after the electroforming process indicates that no breakdown related to this initial step occurs in the CeO_{2-x} layer. In addition, the volume switching demonstrates that resistive switching is homogeneously extended over the 40nm $La_{0.8}Sr_{0.2}MnO_3$ layer and it is not produced by localized thin filaments.

At the end of the thesis, we have presented a first approach to the implementation of metal-oxide-metal vertical devices. In this case, we have used conductive $SrTiO_3$ doped Nb as substrate to grow epitaxial $La_{0.8}Sr_{0.2}MnO_3$. Ag deposition by sputtering was performed in order to obtain Ag/$La_{0.8}Sr_{0.2}MnO_3$/Nb:STO devices and Ag/CeO_{2-x}/ $La_{0.8}Sr_{0.2}MnO_3$/Nb:STO bilayer devices. In agreement with the results presented in lateral devices, bipolar resistive switching was induced in the latter devices when the measurement probe was located on top of the Ag electrode while in Ag/$La_{0.8}Sr_{0.2}MnO_3$/Nb:STO devices, no resistive switching was observed until the probe was placed directly on the $La_{0.8}Sr_{0.2}MnO_3$ layer. These results suggest that the same oxygen ion exchange produce the resistive switching in these vertical devices. However, the different shape of the I-V curves lead us to think that the interface $La_{0.8}Sr_{0.2}MnO_3$/Nb:STO could play an important role in the conduction characteristics of this kind of devices.

Finally, $YBa_2Cu_3O_7$ layers deposited on insulating $LaAlO_3$ substrates were used to investigate the resistive switching characteristics with the objective to extend our knowledge about the switching phenomenon to other different complex oxide with MIT transition. During the evaluation of the physical properties, we found that these physical properties had been modified mainly attributed to creation of oxygen vacancies during the fabrication process. We performed a post-thermal annealing in order to recover the optimal properties for the resistive switching evaluation. We have used these samples to induce bipolar resistive switching in Ag/$YBa_2Cu_3O_7$/Ag lateral devices at relative low

voltage sweeps (4V to -5V). In addition, complementary resistive switching has been induced in the same devices when the V_{max} voltage sweep was increased. It was speculated that a poorly oxygenated YBCO layer is formed at the interface $Ag/YBa_2Cu_3O_7$ which acts as an oxygen reservoir similar to the CeO_{2-x} layer in $CeO_{2-x}/La_{0.7}Sr_{0.3}MnO_3$ bilayer devices enabling this switching mode. The resistance ratio of $\sim10^2$ has been observed to decrease half order of magnitude over 50 operation cycles which indicate a moderate degradation of the properties of the oxide layer.

In summary, the evaluation of the resistive switching properties has been carried out basically in memristor devices based on $La_{0.7}Sr_{0.3}MnO_3$ layers and CeO_{2-x} $/La_{0.7}Sr_{0.3}MnO_3$ bilayer devices. The resistive switching properties observed in the latter structures demonstrate that these materials can be implemented in memristor for operation as non-volatile memory devices due to high resistance ratio and of $\sim10^4$ and low voltage operation (±3V) over at least 100 cycles. Using these $CeO_{2-x}/La_{0.7}Sr_{0.3}MnO_3$ bilayer devices, we have implemented three-terminal devices to induce volume switching used to modify the conduction characteristics of a track through a gate electrode. Therefore, the main objectives of this thesis have been achieved.

Appendix A
Characterization techniques overview

In this section we provide an overview of the working principles of the experimental techniques used for the analysis of the structural and physical properties of our samples. This techniques range from Atomic Force Microscopy (AFM), X-ray Diffraction (XRD), and measurements of physical properties such as magnetization and electric transport. In addition, using micrometric structures, some parameters such as resistivity and contact resistance are obtained. Some of these techniques were performed with the help of the technician staff in turn.

A.1 Atomic Force Microscopy (AFM)

Scanning Probe Microscopy (SPM) is defined as a specific type of microscopy that uses basic principle of scanning a surface with a very sharp probe to produce an image and measure properties of the material under analysis. According to the tip-sample interaction the microscopy has a specific name. The two primary forms are Scanning Tunnelling Microscopy (STM) and Atomic Force Microscopy (AFM) [126].

Regarding AFM, it can provide a profile on a nanoscale by measuring forces between a sharp probe and a surface at very short distance (0.2-10nm probe-sample separation). Figure A.1a shows a sharp tip at the free end of the cantilever which is brought in contact with the sample surface. The tip interacts with the surface, causing the cantilever to bend. A laser spot is reflected from the cantilever onto a position-sensitive photodiode detector. As the cantilever bends, the position of the laser spot changes. The resulting signal from the detector is the deflection in volts. There are three modes of function: contact mode, intermittent or tapping mode and non-contact mode. Figure A.1b shows the force interaction as the tip approaches to the sample. At the right side of the curve, the tip and the sample are separated by a large distance. As they approach, the tip and the sample atoms first weakly attract each other. This zone of interaction is known as the non-contact regime. When this approximation increases, in the intermittent contact regime, the repulsive van der Waals force predominates. When the distance between the tip and the sample is just a few angstroms, forces balance and the net force drops to zero. When the total force becomes positive (repulsive), the atoms are

in the contact regime. There are also other complications of the tip-sample interaction because of additional forces, including strong capillary and adhesive forces that may attract the tip and the sample [127].

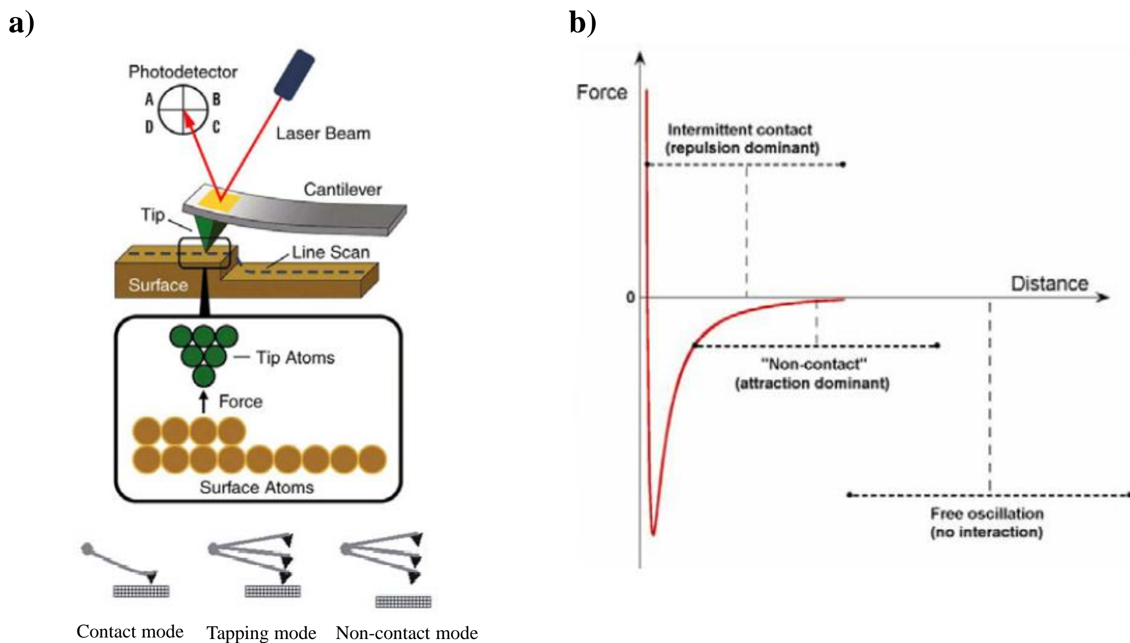

Fig. A.1 a) AFM setup and modes of operation and b) interaction forces between the tip and the sample.

The samples characterized in this thesis were analysed with two different devices: Agilent 5100 and Agilent 5500LS both located at the ICMAB. The images were acquired using a FORT tip using tapping mode. This mode is used for scanning the surface of the samples without any damage. The tips are made of Silicon with nominal radius of 150nm. In the tapping working mode, the tip vibrates at a frequency of 200-400 kHz which produces that the contact between the tip and the surface alternates. The commercial MountainsMap 7.0 software was used for treating the images obtained from the AFM setup. The root mean square roughness which is average of the roughness profile, is calculated using this software. In addition, measurements of the step profile used to obtain the layers thicknesses are performed using this software. An example of such procedure is observed in figure A.2. for a LSMO layer of 40 nm.

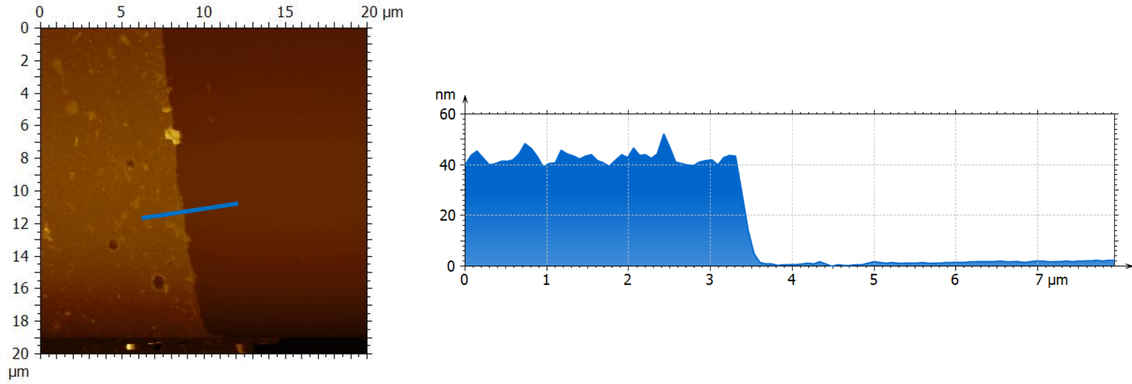

Fig. A2. AFM image of the step profile of a LSMO with thickness of 40nm.

A.2 X-Ray Diffraction (XRD)

X-rays are electromagnetic radiations with a wavelength in the range of 0.1-100 Å [128]. This technique is used to measure the atomic arrangement of materials and to identify the nature and structure of the crystallized products. When a monochromatic X-ray beam hit a sample, it interacts with the electron surrounding the atoms and scattering is produced. Providing that the X-ray fulfill the Bragg condition, we will have a constructive interference and observe a diffraction peak. Bragg's law describes the diffraction of X-rays by a crystal. In Figure A.3, the incident X-rays hit the crystal planes in an angle θ, and the reflection angle is also θ. The diffraction pattern is a function when the Bragg condition is satisfied such that:

$$n\lambda = 2d_{h,k,l} \sin\theta \qquad \text{(A1.1)}$$

Where λ is the wavelength, *d* is the distance between each adjacent crystal plane (d spacing), and θ is the Bragg angle at which one observes a diffraction peak. For real materials, the diffraction patterns vary from theoretical delta functions with discrete relationships between points to continuous distributions with spherical symmetry.

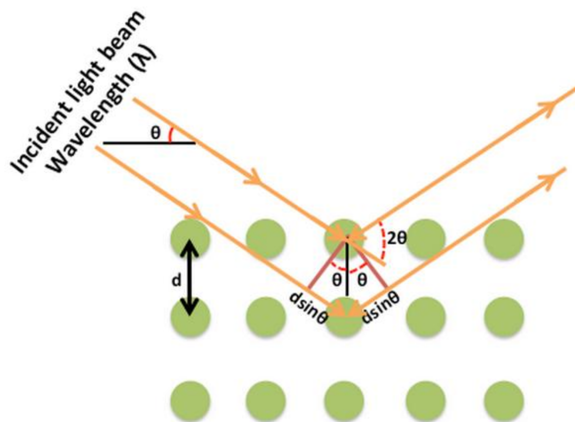

A.3. Schematic description of the Bragg's diffraction law [127]

A diffraction pattern can be obtained by changing the incidence angle of X-rays resulting in a characteristic fingerprint of a particular material. The number, position and intensity of Bragg peaks in a diffraction pattern basically depend on the symmetry and size of the unit cell, the arrangement of atoms within it and on the nature and wavelength of the radiation employed. In particular, in highly oriented samples such as single crystals or epitaxial thin films, only specific families of *hkl* planes are in diffraction conditions and, thus, the pattern exhibits only those planes. Different diffraction conditions can be achieved by modifying the relative position between sample and detector (fig. A.4) and, thus, collect information like crystal structure and quality, or in-plane and out-of-plane texture and orientation.

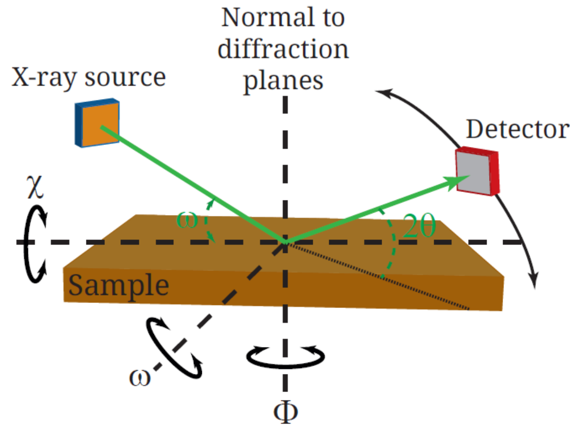

Fig. A.6. General set up and angle nomenclature in XRD measurements. Particular, tuning will be necessary depending on the experimental.

In this thesis, we have performed one dimension (1D) θ-2θ scans which give information about the crystallographic orientation of substrates and thin films. This measurements were performed with a Rigaku Rotaflex RU-200BV diffractometer located at ICMAB with a Cu-K_α source (λ^{Cu}=1.5406 Å). Data acquisition was typically performed with a 0.02° step size.

For LSMO we have considered a pseudocubic system:

$$d_{h,k,l} = \frac{a}{\sqrt{h^2 + k^2 + l^2}} \qquad \text{(A1.2)}$$

So that the Bragg's law (A.1.1) can be rewritten as:

$$n\lambda = \frac{2a}{\sqrt{h^2 + k^2 + l^2}} \sin\theta \qquad \text{(A1.3)}$$

$$2\theta = 2\sin^{-1}\left(\frac{n\lambda\sqrt{h^2 + k^2 + l^2}}{2a}\right) \qquad \text{(A1.4)}$$

Based on equation A1.3, position of the diffraction peaks can be calculated providing that the parameters are well known. In $La_{0.7}Sr_{0.3}MnO_3$ we know the lattice constant $a = 3.873Å$. For n=1 and the (003) reflection, for instance, we have:

$$2\theta = 2\sin^{-1}\left(\frac{1.5406Å\sqrt{0^2+0^2+3^2}}{2*3.873Å}\right) \quad \text{(A1.5)}$$

$$2\theta = 73.26° \quad \text{(A1.6)}$$

This procedure is repeated for other reflection (001) and (002) in $La_{0.7}Sr_{0.3}MnO_3$ and STO with lattice constant $a = 3.905Å$. Table A.1 summarizes the values calculated using these parameters.

Reflections	(001)	(002)	(003)
$La_{0.7}Sr_{0.3}MnO_3$	22.94°	46.87°	73.26°
$SrTiO_2$	22.75°	46.47°	72.56°

Table A.1. K_α peak positions for (00l) reflections for $La_{0.7}Sr_{0.3}MnO_3$ and STO

However, the easiest way to correlate the peaks is through JCPDS database which is a software created by the International Centre for Diffraction Data (ICDD) [129] where the 2θ values are calculated according to the material composition. In this work, both procedures were used to determine the 2θ reflections.

A.3 Magnetization measurements

A superconducting quantum interference device (SQUID) is a very sensitive magnetometer utilized for the measurement of magnetization properties of our samples. This can be achieved thanks to a superconducting loop with one or two weak links inserted in these devices. Basically, they generate an output voltage signal, which is a periodic function of the magnetic flux, a geometry known as DC-SQUID (constant bias current). The magnetometer consists of a SQUID system and a precision temperature control unit attached to a high-field superconducting coil. The sample is put inside the coil producing a uniform dc-magnetic field at its location. Once the sample is magnetized, it is moved through a set of pickup coils inducing a current in the detection system which is proportional to the variation of magnetic flux. This signal is amplified via a SQUID sensor in form of voltage. Therefore, the magnetic moment of the sample is proportional to voltage variations detected with the SQUID, which can resolve

magnetic moments as subtle as 10^{-7} emu. The whole system goes inside a helium cryostat whose function is to refrigerate the superconducting coil and provides precise temperature control. Field and temperature dependent magnetization curves of LSMO thin films were measured at ICMAB using a commercial MPMS XL-7T SQUID DC-magnetometer (Quantum Design) equipped with a 7 T superconducting coil and a helium cryostat with temperature control from 1.8 to 400 K.

We have used this magnetometer to characterize LSMO layers and CeO_{2-x}/LSMO bilayers to obtain two different curves: (i) magnetization versus applied magnetic field at fixed temperature (fig A.7a) and (ii) magnetization as a function of temperature at fixed applied magnetic field (fig A.7b). The magnetization curves presented a strong negative slope due to the diamagnetic contribution of the single crystal substrates. Data treatment involved the withdrawal the aforementioned contribution by linear fitting of the diamagnetic signal as shown in figure A.7a. In addition, this contribution produces negative magnetization values in the m(T) curve which are suppressed by shifting the most negative value to 0 as observed in figure A.7b.

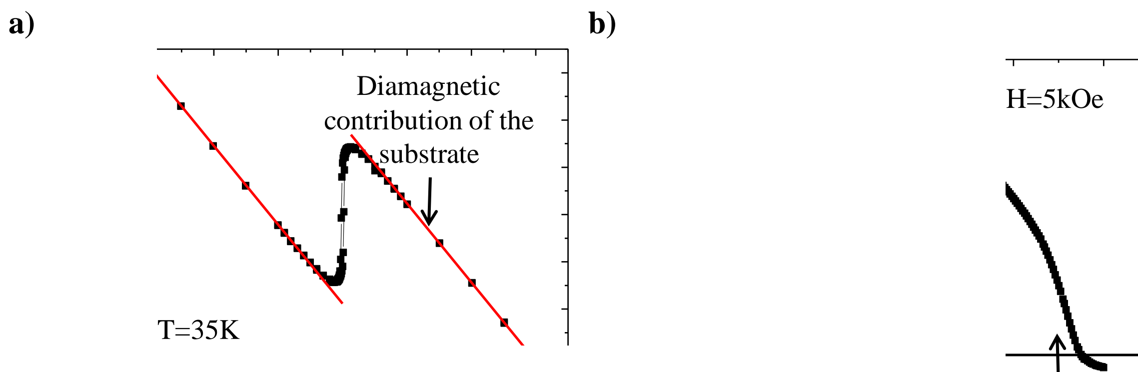

Fig. A.7. Magnetization curves presented diamagnetic contribution of the substrate STO a) magnetization as a function of the applied field and b) magnetization as a function of temperature.

A.4 Electric transport

Electric transport measurements in $La_{1-x}Sr_xMnO_3$ films have been measured using a Physical Properties Measurement System (PPMS) from Quantum Design located at ICMAB. Similar to SQUID system, the PPMS has a 9T superconducting magnet and He cryostat which allows a precise control of temperature between 1.8K and 400K. In addition, it incorporates a voltmeter and an AC/DC current source which can provide current values down to 1μA and up to 2A. A thermometer is located just below the sample mounting space to monitor accurately the sample temperature.

The sample is attached to a special puck for resistivity measurements from Quantum Design. In order to provide good thermal conductivity between the puck and the sample, it is attached with silver paint in the back side. Since we are using a high insulator STO substrate, no leakage current is observed.

The resistivity of thin films is determined based on the van der Pauw method [82]. Fig. A.8 presents a sketch of the measurements using a four point configuration which allows us to avoid the contribution of contact resistivity. In this configuration, the current is applied through two contacts (M and N) and voltage is measured on the other two (O and P). Then, a second measurement is performed by applying current through two other contacts (O and N) and voltage is measured on the remaining ones (P and M).

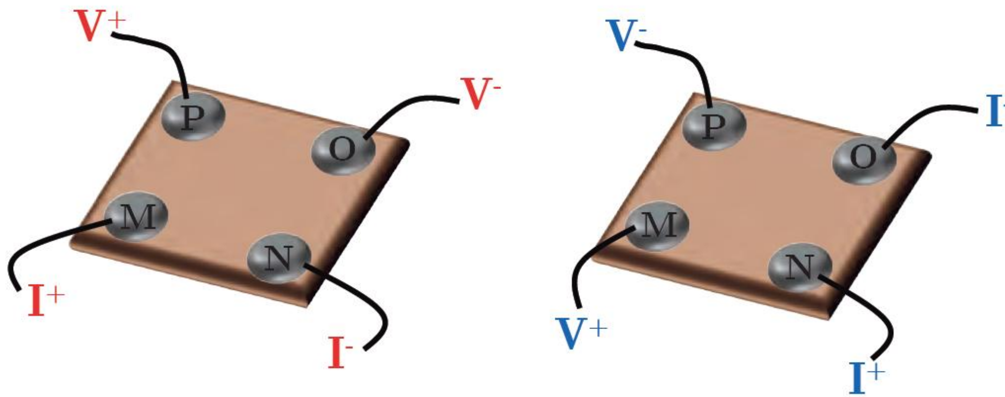

Fig. A.8. Van der Pauw configuration to perform resistivity measurements in layers.

The resistivity ρ is calculated following the van der Pauw method using the following expression:

$$\rho = \frac{\pi t}{\ln 2}\frac{R_{MN,PO} + R_{NO,MP}}{2}F \qquad \text{(A1.7)}$$

Where $R_{MN,PO} = V_{PO}/I_{MN}$ and $R_{NO,MP} = V_{NO}/I_{MP}$ are the resistance values for the two measurements, t is the thickness of the sample and F is a correction factor which depends on the ratio $R_r = R_{MN,PO}/R_{NO,MP}$. The dependence of F on R_r is shown in figure A.9.

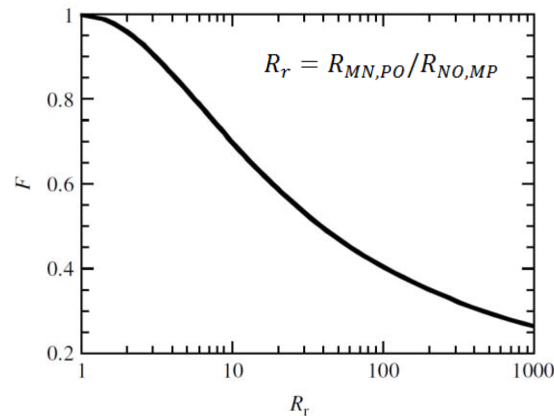

Fig. A.9 The van der Pauw correction factor F versus R_r.[100]

A.5 Modified Four-probe measurements

Material research and device testing often involve determining the resistivity of the sample. With a four-probe technique, also known as Kelvin, two of the probes are used as current source and the other two probes are used to measure voltage. Using for probes eliminates measurement errors due to probe resistance, the spreading resistance under each probe, and the contact resistance between each metal probe and the material. Because a high impedance voltmeter drives small current, the voltage drops across the probe resistance, spreading resistance and contact resistance are very small. In figure A.10, a four-probe resistance measurement setup is presented. The two outer probes are used for sourcing current while the two inner probes are used for measuring the resulting voltage drop across the surface of the sample.

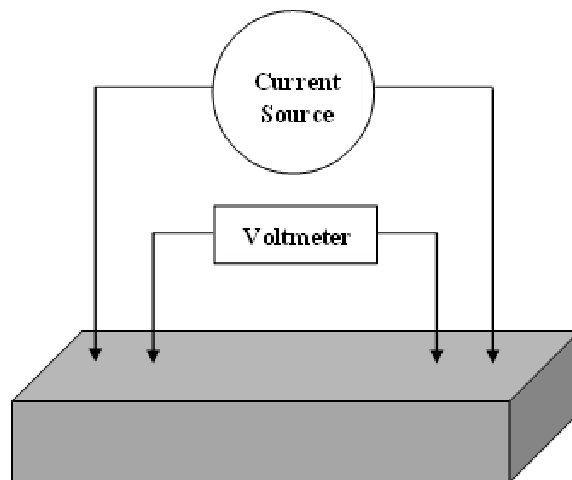

Fig. A.10. Four-point probe resistance measurement

This kind of measurements were performed by using either the Keithley model 4200 system or the Agilent Semiconductor Parameter Analyzer 4156B, both located at the Electronic Department of UAB. In this regard, the four source-measure units (SMUs) have to be used to perform these measurements. Three of the SMUs are set to current bias while the fourth is the ground unit (GNDU). An example of how this can be set up with the measurement equipment is shown in figure A.11. One SMU1 and the GNDU defined in SMU4 are used as current source. Two other SMUs (SMU2 and SMU3) are used to measure the voltage drop between the two inner probes [130].

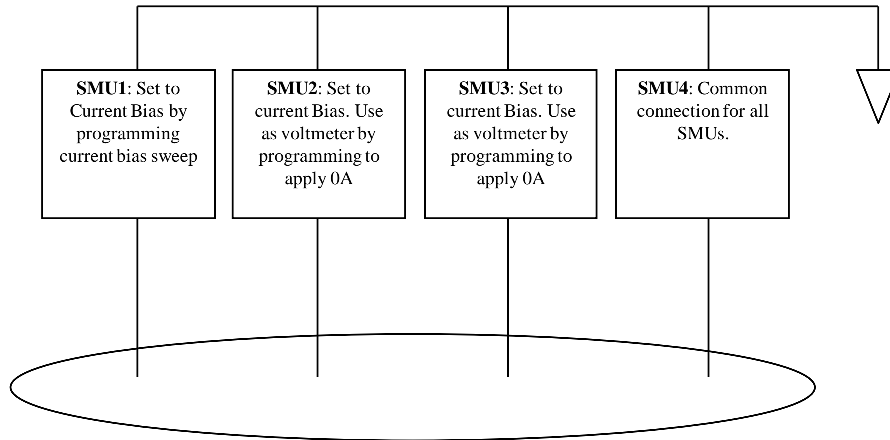

Fig. A.11, SMUs designation for four-point probe measurements.

The resistivity and the contact resistance are measured in a cross-bridge structure [100], which has been patterned on $La_{1-x}Sr_xMnO_3$ using photolithography and etching processes. Then, sputtering has been performed to form the metal electrodes. In chapter 2, figure 2.22 shows a schematic of the cross-bridge structure fabricated on a $La_{0.7}Sr_{0.3}MnO_3$ layer.

This method was applied in order to obtain the resistivity value through resistance measurements. Since a four-point probe collinear-like configuration was applied in the cross-bridge structures, the resistivity (ρ) can be calculated as follows:

$$\rho = R\frac{tW}{L} \quad \text{(A1.8)}$$

Where R represents the measured resistance in Ω and the geometric parameters of the structure, thickness (t), length (L) and width (W) are well known from the design and they are showed in a picture taken to a patterned structure in figure A.12.

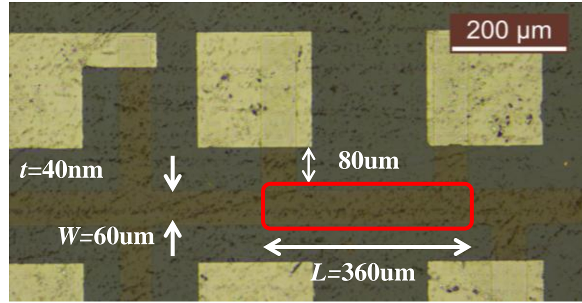

A.12. Schematic of a cross-bridge structure showing its dimensions. The red square represents the line where the voltage drop in SMU2 and SMU3 is measured.

As a result, the resistance can be calculated from Ohm's law by taking into account the voltage drop in SMU2 and SMU3 (red square in figure A.12) and the value of the applied current. First, the resistance difference between these two units is obtained by subtracting the R_{V2} to R_{V1} producing the R_{4P}=R_{V1}-R_{V2} showed in figure A.13. In this case, the R_{4P}=7340Ω is calculated from the slope.

Ag (50nm)/$La_{0.7}Sr_{0.2}MnO_3$(40nm)

Fig. A.13. The resistance in the line is deduced from the slope of R_{V1}-R_{V2}.

Finally, the resistivity is calculated by substituting the value R_{4P} in R and those parameters related to the geometry in equation A1.8.

A.6 Contact Resistance

Once the value of the resistivity has been calculated using the methodology presented in the modified four-point probe measurements, the contact resistance metal/$La_{0.7}Sr_{0.3}MnO_3$ was evaluated using two different methods: the cross-bridge structure and the transmission line method [100].

A.6.1 Evaluation of the contact resistance using the cross-bridge structure

In this case, the same cross-bridge structure is used to perform 2-probe measurements. Figure A.14 shows a schematic of the area where the evaluation of the resistance is

measured. In this image we can see, apart from the track taking into account where the resistivity measurements were performed, another two small tracks of the $La_{0.7}Sr_{0.3}MnO_3$ considered for the calculation.

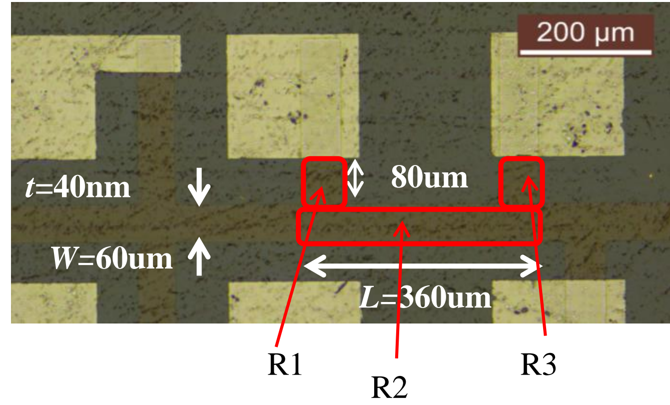

Fig. A.14. Schematic of the track considered for the evaluation of the contact resistance.

Therefore, the resistance of the track is:

$$R_{track} = R_1 + R_2 + R_3 \quad \text{(A.9)}$$

The resistance R_2 is already known from the 4-point probe measurements and R_1 and R_3 are calculated using equation A1.8 since the resistivity and the geometrical parameters are also known. As a result, the contact resistance is the half of difference between the resistances measured with 2-probes minus the resistance calculated for the track as follows:

$$R_C = \frac{R_{2probe} - R_{track}}{2} \quad \text{(A.10)}$$

A.6.2 Evaluation of the contact resistance using the transmission line method

This method was developed to measure the contact resistance of a metal-semiconductor junction but we have adapted it for measuring metal/$La_{1-x}Sr_xMnO_3$ junctions. The first step is to deposit the metal on the $La_{1-x}Sr_xMnO_3$ layer and pattern it so that you have identical pads spaced varying distances apart. All the pads in any one row must be the same size, and the distances between pads must vary. The measurements required are simple I-V curves. From this, we calculate the resistance between those two pads using the Ohms law. The total resistance between any two pads is the series combination of 3 resistors: metal to $La_{1-x}Sr_xMnO_3$, through the $La_{1-x}Sr_xMnO_3$, and back into metal. In the limit where the distance between the pads approaches 0, R_{semi} goes to 0 and what is left is $2R_{pad.}$ A schematic of the transmission line method is shown in figure A.15.

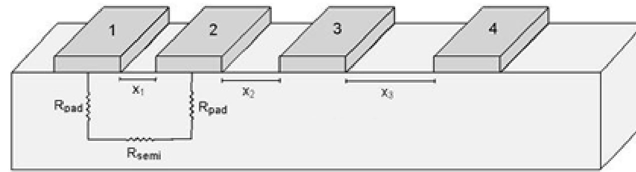

Fig. A.15 Schematic of the transmission line method to measure contact resistance.

A $La_{0.7}Sr_{0.3}MnO_3$ sample was patterned to have a collection of 6 pads in each row. A schematic of this sample is shown in figure A.16 where the distance between the pads is also shown.

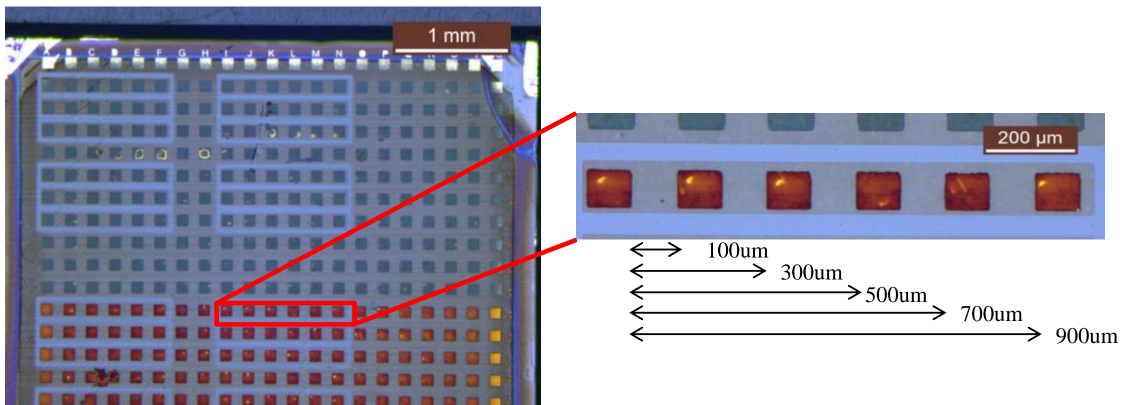

Fig. 1.16. $La_{0.7}Sr_{0.3}MnO_3$ sample patterned to perform the contact resistance measurements using the transmission line method. The distance between the electrodes is shown.

The measurements were performed by leaving one static probe in the first pad and moving the second probe along the pads in the row. For each measurement, the resistance is calculated from the slope of the I-V curves according to what was shown in figure A.17 where a set of 6 curves is plotted for each row. Finally, the resistance is plotted as a function of the distance between the pads. In the limit of zero-length resistor, the residual resistance is just twice the contact resistance. This can be found from the graph by extrapolating back to L=0.

Fig A.17. Set of I-V curves measured in one row to obtain the contact resistance according to the transmission line method

A.7 Resistive switching measurement setup

The evaluation of the resistive switching in memristor devices was performed using either the Keithley 4200-Semiconductor Characterization System and the Agilent 4156C Semiconductor Parameter analyzer. The functionalities used from each system are not different between them and we refer indistinctly as the measurement setup. In all of our measurements, the sample was placed inside of a probe station which is insulated as a Faraday shield in order to avoid electric interferences. In addition, the sample was firmly attached to the chuck through a vacuum system and the micrometric probes were placed manually on the sample. I-V measurements were conducted through these two probes which have been configured by software to apply voltage ramps while sensing the current as illustrated in figure A.18a.

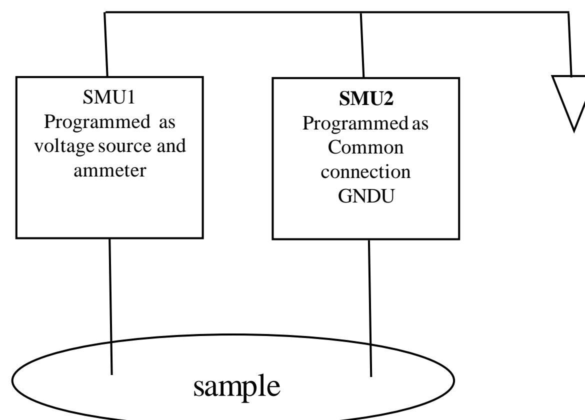

Fig. A.18. Setup configuration for two-probe measurements.

Double voltage ramps were programmed at each voltage sweep as illustrated in figure A.19a. At each step, the programmed voltage is applied and the current is measured after short integration time (fig. A.19b). In order to avoid noisy measurements, we have employed normal integration time defined as 1.00PLC (power line cycles). In the case of the line with 50Hz, the PLC value is 20msec (1/50Hz).

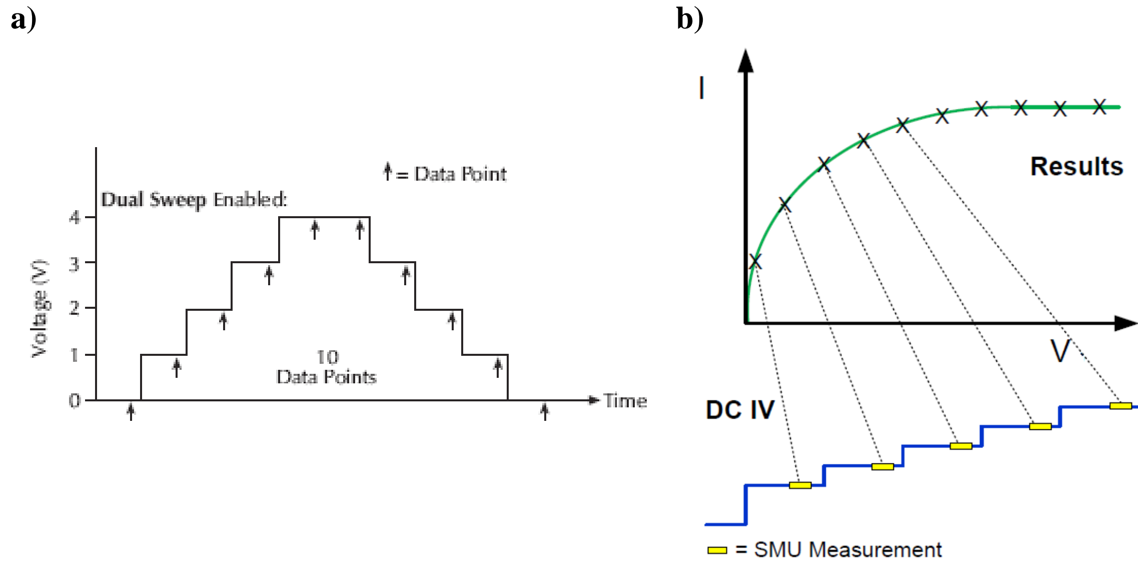

Fig. A.19. a) Double voltage sweep used to perform resistive switching measurements in two-terminal memristor devices and b) creation of the I-V curves departing from voltage sweeps measurements.

Bibliography

[1] ITRS ERD Working Group, “International Technology Roadmap for Semiconductors 2011 Edition - Emerging Research Devices,” 2011.

[2] G. W. Burr, B. N. Kurdi, J. C. Scott, C. H. Lam, K. Gopalakrishnan, and R. S. Shenoy, “Overview of candidate device technologies for storage-class memory,” *IBM J. Res. Dev.*, vol. 52, no. 449, 2008.

[3] M. H. Kryder, “After Hard Drives—What Comes Next?,” *IEEE Trans. Magn.*, vol. 45, no. 10, pp. 3406–3413, Oct. 2009.

[4] E. Linn, R. Rosezin, C. Kügeler, and R. Waser, “Complementary resistive switches for passive nanocrossbar memories.,” *Nat. Mater.*, vol. 9, no. 5, pp. 403–406, May 2010.

[5] H. Akinaga and H. Shima, “Resistive Random Access Memory (ReRAM) Based on Metal Oxides,” *Proc. IEEE*, vol. 98, no. 12, pp. 2237–2251, Dec. 2010.

[6] A. Sawa, “Resistive switching in transition metal oxides,” *Mater. Today*, vol. 11, no. 6, pp. 28–36, 2008.

[7] R. Waser, R. Dittmann, C. Staikov, and K. Szot, “Redox-based resistive switching memories nanoionic mechanisms, prospects, and challenges,” *Adv. Mater.*, vol. 21, no. 25–26, pp. 2632–2663, Jul. 2009.

[8] S. D. Ha and S. Ramanathan, “Adaptive oxide electronics: A review,” *J. Appl. Phys.*, vol. 110, no. 7, p. 071101, 2011.

[9] C. Moreno, C. Munuera, S. Valencia, F. Kronast, X. Obradors, and C. Ocal, “Reversible resistive switching and multilevel recording in La0.7Sr0.3MnO3 thin films for low cost nonvolatile memories.,” *Nano Lett.*, vol. 10, no. 10, pp. 3828–3835, Oct. 2010.

[10] W. S. Lee, “Future memory technologies,” in *International Conference on Solid-State and Integrated Circuits Technology Proceedings, ICSICT*, 2008, pp. 1–4.

[11] R. Waser and M. Aono, “Nanoionics-based resistive switching memories.,” *Nat. Mater.*, vol. 6, no. 11, pp. 833–840, 2007.

[12] L. Chua, “Memristor-The missing circuit element,” *IEEE Trans. Circuit Theory*, vol. 18, no. 5, 1971.

[13] D. C. Kim, M. J. Lee, S. E. Ahn, S. Seo, J. C. Park, I. K. Yoo, I. G. Baek, H. J. Kim, E. K. Yim, J. E. Lee, S. O. Park, H. S. Kim, U.-I. Chung, J. T. Moon, and B. I. Ryu, “Improvement of resistive memory switching in NiO using IrO2,” *Appl. Phys. Lett.*, vol. 88, no. 23, p. 232106, 2006.

[14] L. Goux, R. Degraeve, B. Govoreanu, H.-Y. Chou, V. V. Afanas'ev, J. Meersschaut, M. Toeller, X. P. Wang, S. Kubicek, O. Richard, J. a. Kittl, D. J. Wouters, M. Jurczak, and L. Altimime, "Evidences of anodic-oxidation reset mechanism in TiN\NiO\Ni RRAM cells," *2011 Symp. VLSI Technol. - Dig. Tech. Pap.*, vol. 77, no. 2010, pp. 24–25, 2011.

[15] C. Rohde, B. J. Choi, D. S. Jeong, S. Choi, J. S. Zhao, and C. S. Hwang, "Identification of a determining parameter for resistive switching of TiO2 thin films," *Appl. Phys. Lett.*, vol. 86, no. 26, pp. 1–3, 2005.

[16] A. Younis, D. Chu, and S. Li, "Oxygen level: the dominant of resistive switching characteristics in cerium oxide thin films," *J. Phys. D. Appl. Phys.*, vol. 45, no. 35, p. 355101, Sep. 2012.

[17] C.-Y. Lin, D.-Y. Lee, S.-Y. Wang, C.-C. Lin, and T.-Y. Tseng, "Reproducible resistive switching behavior in sputtered CeO2 polycrystalline films," *Surf. Coatings Technol.*, vol. 203, no. 5–7, pp. 480–483, Dec. 2008.

[18] X. Lian, X. Cartoixà, E. Miranda, L. Perniola, R. Rurali, S. Long, M. Liu, and J. Suñé, "Multi-scale quantum point contact model for filamentary conduction in resistive random access memories devices," *J. Appl. Phys.*, vol. 115, no. 24, p. 244507, Jun. 2014.

[19] Y. S. Chen, H. Y. Lee, P. S. Chen, W. H. Liu, S. M. Wang, P. Y. Gu, Y. Y. Hsu, C. H. Tsai, W. S. Chen, F. Chen, M. J. Tsai, and C. Lien, "Robust high-resistance state and improved endurance of HfOX resistive memory by suppression of current overshoot," *IEEE Electron Device Lett.*, vol. 32, no. 11, pp. 1585–1587, 2011.

[20] A. Sawa, T. Fujii, M. Kawasaki, and Y. Tokura, "Hysteretic current–voltage characteristics and resistance switching at a rectifying Ti/Pr0.7Ca0.3MnO3 interface," *Appl. Phys. Lett.*, vol. 85, no. 18, p. 4073, 2004.

[21] S. Park, S. Jung, M. Siddik, M. Jo, J. Lee, J. Park, W. Lee, S. Kim, S. M. Sadaf, X. Liu, and H. Hwang, "Memristive switching behavior in Pr0.7Ca0.3MnO3 by incorporating an oxygen-deficient layer," *Phys. status solidi - Rapid Res. Lett.*, vol. 5, no. 10–11, pp. 409–411, Nov. 2011.

[22] S. G. Choi, H.-S. Lee, H. Choi, S.-W. Chung, and H.-H. Park, "The effect of Sr concentration on resistive switching properties of La1−xSrxMnO3 films," *Thin Solid Films*, vol. 529, pp. 352–355, Feb. 2012.

[23] D. Liu, N. Wang, G. Wang, Z. Shao, X. Zhu, C. Zhang, and H. Cheng, "Programmable metallization cells based on amorphous La0.79Sr0.21MnO3 thin films for memory applications," *J. Alloys Compd.*, vol. 580, pp. 354–357, Dec. 2013.

[24] L. Vandelli, A. Padovani, L. Larcher, G. Broglia, G. Ori, M. Montorsi, G. Bersuker, and P. Pavan, "Comprehensive physical modeling of forming and switching operations in HfO 2 RRAM devices," *Tech. Dig. - Int. Electron Devices Meet. IEDM*, no. 10, pp. 421–424, 2011.

[25] T. Fujii, M. Kawasaki, A. Sawa, H. Akoh, Y. Kawazoe, and Y. Tokura, “Hysteretic current–voltage characteristics and resistance switching at an epitaxial oxide Schottky junction SrRuO3⁄SrTi0.99Nb 0.01Osub3,” *Appl. Phys. Lett.*, vol. 86, no. 1, p. 012107, Dec. 2005.

[26] R. Fors, S. Khartsev, and A. Grishin, “Giant resistance switching in metal-insulator-manganite junctions: Evidence for Mott transition,” *Phys. Rev. B*, vol. 71, no. 4, p. 045305, Jan. 2005.

[27] T. Oka and N. Nagaosa, “Interfaces of correlated electron systems: Proposed mechanism for colossal electroresistance,” *Phys. Rev. Lett.*, vol. 95, no. 26, p. 266403, Dec. 2005.

[28] J. Wu, J. Cao, W.-Q. Han, A. Janotti, and H.-C. Kim, Eds., *Functional Metal Oxide Nanostructures*, vol. 149. New York, NY: Springer New York, 2012.

[29] F. Nardi, S. Balatti, S. Larentis, and D. Ielmini, “Complementary switching in metal oxides: Toward diode-less crossbar RRAMs,” *2011 Int. Electron Devices Meet.*, pp. 31.1.1–31.1.4, Dec. 2011.

[30] T. Berzina, S. Erokhina, P. Camorani, O. Konovalov, V. Erokhin, and M. P. Fontana, “Electrochemical control of the conductivity in an organic memristor: a time-resolved X-ray fluorescence study of ionic drift as a function of the applied voltage.,” *ACS Appl. Mater. Interfaces*, vol. 1, no. 10, pp. 2115–8, Oct. 2009.

[31] T. Sakamoto, N. Banno, N. Iguchi, H. Kawaura, S. Kaeriyama, M. Mizuno, K. Terabe, T. Hasegawa, and M. Aono, “Three terminal solid-electrolyte nanometer switch,” in *IEEE InternationalElectron Devices Meeting, 2005. IEDM Technical Digest.*, pp. 475–478.

[32] Y. Kaneko, H. Tanaka, M. Ueda, Y. Kato, and E. Fujii, “A novel ferroelectric memristor enabling NAND-type analog memory characteristics,” in *68th Device Research Conference*, 2010, pp. 257–258.

[33] M. H. Ben Jamaa, S. Carrara, J. Georgiou, N. Archontas, and G. De Micheli, “Fabrication of memristors with poly-crystalline silicon nanowires,” pp. 152–154.

[34] D. Sacchetto, M. H. Ben-Jamaa, G. DeMicheli, and Y. usuf Leblebici, “Fabrication and characterization of vertically stacked Gate-All-Around Si Nanowire FET arrays,” in *2009 Proceedings of the European Solid State Device Research Conference*, 2009, pp. 245–248.

[35] D. Sacchetto, G. De Micheli, and Y. Leblebici, “Multiterminal Memristive Nanowire Devices for Logic and Memory Applications: A Review,” *Proc. IEEE*, vol. 100, no. 6, pp. 2008–2020, Jun. 2012.

[36] S. H. Jo, K.-H. Kim, and W. Lu, “High-Density Crossbar Arrays Based on a Si Memristive System,” *Nano Lett.*, vol. 9, no. 2, pp. 870–874, Feb. 2009.

[37] L. Chua, “Memristors: A new nanoscale CNN cell,” in *Cellular Nanoscale Sensory Wave Computing*, C. Baatar, W. Porod, and T. Roska, Eds. Boston, MA: Springer US, 2010.

[38] D. Beeman, “Hodgkin-Huxley model,” in *Encyclopedia of Computational Neuroscience*, D. Jaeger and R. Jung, Eds. New York, NY: Springer New York, 2015.

[39] L. O. Chua, “Memristive devices and systems,” *Proc. IEEE*, vol. 64, no. 2, pp. 209–223, Feb. 1976.

[40] Y. L. Jin, K. Jin, C. Ge, H. Lu, and G. Yang, “Resistive Switching Phenomena in Complex Oxide Heterostrucutres,” *Mod. Phys. Lett. B*, Nov. 2013.

[41] V. M. Goldschmidt, “Die Gesetze der Krystallochemie,” *Naturwissenschaften*, vol. 14, no. 21, pp. 477–485, May 1926.

[42] H. A. Jahn and E. Teller, “Stability of Polyatomic Molecules in Degenerate Electronic States. I. Orbital Degeneracy,” *Proc. R. Soc. A Math. Phys. Eng. Sci.*, vol. 161, no. 905, pp. 220–235, Jul. 1937.

[43] Y. Tokura, “Critical features of colossal magnetoresistive manganites,” *Reports Prog. Phys.*, vol. 69, no. 3, pp. 797–851, Mar. 2006.

[44] C. Zener, “Interaction Between the d Shells in the Transition Metals,” *Phys. Rev.*, vol. 81, no. 3, pp. 440–444, Feb. 1951.

[45] E. Dagotto, T. Hotta, and A. Moreo, “Colossal Magnetoresistant Materials: The Key Role of Phase Separation,” p. 76, Dec. 2000.

[46] A.-M. Haghiri-Gosnet and J.-P. Renard, “CMR manganites: physics, thin films and devices,” *J. Phys. D. Appl. Phys.*, vol. 36, no. 8, pp. R127–R150, Apr. 2003.

[47] A. P. Ramirez, “Colossal magnetoresistance,” *J. Phys. Condens. Matter*, vol. 9, no. 39, pp. 8171–8199, Sep. 1997.

[48] A. Urushibara, T. Arima, A. Asamitsu, G. Kido, and Y. Tokura, “Insulator-metal transition and giant magnetoresistance in La1-xSrxMnO3,” *Phys. Rev. B*, vol. 51, no. 20, pp. 14103–14109, May 1995.

[49] M. Rajeswari, R. Shreekala, A. Goyal, S. E. Lofland, S. M. Bhagat, K. Ghosh, R. P. Sharma, R. L. Greene, R. Ramesh, T. Venkatesan, and T. Boettcher, “Correlation between magnetic homogeneity, oxygen content, and electrical and magnetic properties of perovskite manganite thin films,” *Appl. Phys. Lett.*, vol. 73, no. 18, p. 2672, Nov. 1998.

[50] Z. L. Wang, J. S. Yin, Y. D. Jiang, and J. Zhang, “Studies of Mn valence conversion and oxygen vacancies in La1−xCaxMnO3−y using electron energy-loss spectroscopy,” *Appl. Phys. Lett.*, vol. 70, no. 25, p. 3362, Jun. 1997.

[51] E. Breckenfeld, Z. Chen, A. R. Damodaran, and L. W. Martin, “Effects of nonequilibrium growth, nonstoichiometry, and film orientation on the metal-to-insulator transition in $NdNiO_3$ thin films.,” *ACS Appl. Mater. Interfaces*, vol. 6, no. 24, pp. 22436–44, Dec. 2014.

[52] Y. Zhou and S. Ramanathan, “Correlated Electron Materials and Field Effect Transistors for Logic: A Review,” *Crit. Rev. Solid State Mater. Sci.*, vol. 38, no. 4, pp. 286–317, Jan. 2013.

[53] J. Hubbard, “Electron Correlations in Narrow Energy Bands. II. The Degenerate Band Case,” *Proc. R. Soc. A Math. Phys. Eng. Sci.*, vol. 277, no. 1369, pp. 237–259, Jan. 1964.

[54] T. Inoue, Y. Yamamoto, S. Koyama, S. Suzuki, and Y. Ueda, “Epitaxial growth of CeO2 layers on silicon,” *Appl. Phys. Lett.*, vol. 56, no. 14, pp. 1332–1333, 1990.

[55] X. Obradors, T. Puig, A. Pomar, F. Sandiumenge, N. Mestres, M. Coll, A. Cavallaro, N. Romà, J. Gázquez, J. C. González, O. Castaño, J. Gutierrez, A. Palau, K. Zalamova, S. Morlens, A. Hassini, M. Gibert, S. Ricart, J. M. Moretó, S. Piñol, D. Isfort, and J. Bock, “Progress towards all-chemical superconducting YBa 2 Cu 3 O 7 -coated conductors,” *Supercond. Sci. Technol.*, vol. 19, no. 3, pp. S13–S26, Mar. 2006.

[56] E. P. Murray, T. Tsai, and S. A. Barnett, “A direct-methane fuel cell with a ceria-based anode,” vol. 400, no. 6745, pp. 649–651, Aug. 1999.

[57] S. P. S. Badwal, D. Fini, F. T. Ciacchi, C. Munnings, J. A. Kimpton, and J. Drennan, “Structural and microstructural stability of ceria – gadolinia electrolyte exposed to reducing environments of high temperature fuel cells,” *J. Mater. Chem. A*, vol. 1, no. 36, p. 10768, Aug. 2013.

[58] Y.-M. Chiang, D. P. Birnie, and W. D. Kingery, *Physical Ceramics: Principles for Ceramic Science and Engineering*. 1996.

[59] M. Coll, A. Palau, J. C. Gonzalez-Rosillo, J. Gazquez, X. Obradors, and T. Puig, “Integration of atomic layer deposition CeO2 thin films with functional complex oxides and 3D patterns,” *Thin Solid Films*, vol. 553, pp. 7–12, Feb. 2014.

[60] J. Zabaleta, “Growth and advanced characterization of solution-derived nanoscale La0.7Sr0.3MnO3 heteroepitaxial systems,” Universitat Autonoma de Barcelona, 2012.

[61] M. Coll, J. Gazquez, A. Palau, M. Varela, X. Obradors, and T. Puig, “Low Temperature Epitaxial Oxide Ultrathin Films and Nanostructures by Atomic Layer Deposition,” *Chem. Mater.*, vol. 24, no. 19, pp. 3732–3737, Oct. 2012.

[62] F. Sánchez, C. Ocal, and J. Fontcuberta, “Tailored surfaces of perovskite oxide substrates for conducted growth of thin films.,” *Chem. Soc. Rev.*, vol. 43, no. 7, pp. 2272–85, Apr. 2014.

[63] C. Noguera, *Physics and Chemistry at Oxide Surfaces*. Cambridge: Cambridge University Press, 1996.

[64] G. Koster, B. L. Kropman, G. J. H. M. Rijnders, D. H. A. Blank, and H. Rogalla, "Quasi-ideal strontium titanate crystal surfaces through formation of strontium hydroxide," *Appl. Phys. Lett.*, vol. 73, no. 20, p. 2920, Nov. 1998.

[65] R. W. Schwartz, T. Schneller, and R. Waser, "Chemical solution deposition of electronic oxide films," *Comptes Rendus Chim.*, vol. 7, no. 5, pp. 433–461, May 2004.

[66] R. W. Schwartz, "Chemical Solution Deposition of Perovskite Thin Films," *Chem. Mater.*, vol. 9, no. 11, pp. 2325–2340, Nov. 1997.

[67] X. Obradors, T. Puig, M. Gibert, A. Queraltó, J. Zabaleta, and N. Mestres, "Chemical solution route to self-assembled epitaxial oxide nanostructures.," *Chem. Soc. Rev.*, vol. 43, no. 7, pp. 2200–25, Apr. 2014.

[68] A. Hassini, A. Pomar, J. Gutiérrez, M. Coll, N. Romà, C. Moreno, A. Ruyter, T. Puig, and X. Obradors, "Atomically flat MOD La 0.7 Sr 0.3 MnO 3 buffer layers for high critical current YBa 2 Cu 3 O 7 TFA films," *Supercond. Sci. Technol.*, vol. 20, no. 9, pp. S230–S238, Sep. 2007.

[69] A. Queraltó, "Growth of functional oxide heterostructures from chemical solutions using advanced processing methodologies," Universitat Autonoma de Barcelona, 2015.

[70] C. Moreno, P. Abellán, A. Hassini, A. Ruyter, A. P. del Pino, F. Sandiumenge, M.-J. Casanove, J. Santiso, T. Puig, and X. Obradors, "Spontaneous Outcropping of Self-Assembled Insulating Nanodots in Solution-Derived Metallic Ferromagnetic La 0.7 Sr 0.3 MnO 3 Films," *Adv. Funct. Mater.*, vol. 19, no. 13, pp. 2139–2146, Jul. 2009.

[71] J. Zabaleta, N. Mestres, P. Abellán, M. Gibert, F. Sandiumenge, T. Puig, and X. Obradors, "Orientational ordering of solution derived epitaxial Gd-doped ceria nanowires induced by nanoscratching.," *Nanotechnology*, vol. 21, no. 2, p. 025302, Jan. 2010.

[72] A. K. Pradhan, D. Hunter, T. Williams, B. Lasley-Hunter, R. Bah, H. Mustafa, R. Rakhimov, J. Zhang, D. J. Sellmyer, E. E. Carpenter, D. R. Sahu, and J.-L. Huang, "Magnetic properties of La0.6Sr 0.4MnO3 thin films on SrTiO3 and buffered Si substrates with varying thickness," *J. Appl. Phys.*, vol. 103, no. 2, p. 023914, Jan. 2008.

[73] J. H. Van Der Merwe, "Crystal Interfaces. Part II. Finite Overgrowths," *J. Appl. Phys.*, vol. 34, no. 1, p. 123, Jun. 1963.

[74] C. Adamo, X. Ke, H. Q. Wang, H. L. Xin, T. Heeg, M. E. Hawley, W. Zander, J. Schubert, P. Schiffer, D. A. Muller, L. Maritato, and D. G. Schlom, "Effect of biaxial strain on the electrical and magnetic properties of (001) La0.7Sr0.3MnO3 thin films," *Appl. Phys. Lett.*, vol. 95, no. 11, p. 112504, Sep. 2009.

[75] G. H. Jonker and J. H. Van Santen, "Ferromagnetic compounds of manganese with perovskite structure," *Physica*, vol. 16, no. 3, pp. 337–349, Mar. 1950.

[76] C. Zener, "Interaction between the d -Shells in the Transition Metals. II. Ferromagnetic Compounds of Manganese with Perovskite Structure," *Phys. Rev.*, vol. 82, no. 3, pp. 403–405, May 1951.

[77] T. Becker, C. Streng, Y. Luo, V. Moshnyaga, B. Damaschke, N. Shannon, and K. Samwer, "Intrinsic inhomogeneities in manganite thin films investigated with scanning tunneling spectroscopy.," *Phys. Rev. Lett.*, vol. 89, no. 23, p. 237203, Nov. 2002.

[78] M. Coll, J. Gázquez, A. Pomar, T. Puig, F. Sandiumenge, and X. Obradors, "Stress-induced spontaneous dewetting of heteroepitaxial Y Ba 2 Cu 3 O 7 thin films," *Phys. Rev. B*, vol. 73, no. 7, p. 075420, Feb. 2006.

[79] S. E. Lofland, S. M. Bhagat, C. Kwon, S. D. Tyagi, Y. M. Mukovskii, S. G. Karabashev, and A. M. Balbashov, "Ferromagnetic resonance in a crystal of La0.7Sr0.3MnO3," *J. Appl. Phys.*, vol. 81, no. 8, p. 5737, Apr. 1997.

[80] M. Angeloni, G. Balestrino, N. G. Boggio, P. G. Medaglia, P. Orgiani, and A. Tebano, "Suppression of the metal-insulator transition temperature in thin La0.7Sr0.3MnO3 films," *J. Appl. Phys.*, vol. 96, no. 11, p. 6387, Nov. 2004.

[81] F. Tsui, M. C. Smoak, T. K. Nath, and C. B. Eom, "Strain-dependent magnetic phase diagram of epitaxial La0.67Sr0.33MnO3 thin films," *Appl. Phys. Lett.*, vol. 76, no. 17, p. 2421, Apr. 2000.

[82] L. J. van der Pauw, "A method of measuring the resistivity and hall coefficient of discs of arbitrary shape," *Philips Res. Reports*, vol. 13, no. 1, pp. 1–9, 1958.

[83] J. Sakai, N. Ito, and S. Imai, "Oxygen content of La1−xSrxMnO3−y thin films and its relation to electric-magnetic properties," *J. Appl. Phys.*, vol. 99, no. 8, p. 08Q318, 2006.

[84] M. Mogensen, T. Lindegaard, U. R. Hansen, and G. Mogensen, "Physical Properties of Mixed Conductor Solid Oxide Fuel Cell Anodes of Doped CeO2," vol. 141, no. 8, pp. 2122–2128, 1994.

[85] M. Ritala, "Atomic Layer Deposition of Oxide Thin Films with Metal Alkoxides as Oxygen Sources," *Science (80-.).*, vol. 288, no. 5464, pp. 319–321, Apr. 2000.

[86] S. A. Campbell, *The Science and Engineering of Microelectronic Fabrication*. 1996.

[87] R. C. Jaeger, *Introduction to Microelectronic Fabrication*. Prentice Hall, 2002.

[88] J. D. Plummer, M. D. Deal, and P. B. Griffin, *Silicon VLSI Technology: Fundamentals, Practice and Modeling*. Prentice Hall, 2000.

[89] L. Pain, S. Tedesco, and C. Constancias, “Direct write lithography: the global solution for R&D and manufacturing,” *Comptes Rendus Phys.*, vol. 7, no. 8, pp. 910–923, Oct. 2006.

[90] Z. Liao, P. Gao, Y. Meng, W. Fu, X. Bai, H. Zhao, and D. Chen, “Electrode engineering for improving resistive switching performance in single crystalline CeO2 thin films,” *Solid. State. Electron.*, vol. 72, pp. 4–7, Jun. 2012.

[91] Z. L. Liao, Z. Z. Wang, Y. Meng, Z. Y. Liu, P. Gao, J. L. Gang, H. W. Zhao, X. J. Liang, X. D. Bai, and D. M. Chen, “Categorization of resistive switching of metal-Pr0.7Ca 0.3MnO3-metal devices,” *Appl. Phys. Lett.*, vol. 94, no. 25, p. 253503, 2009.

[92] C. B. Lee, B. S. Kang, A. Benayad, M. J. Lee, S.-E. Ahn, K. H. Kim, G. Stefanovich, Y. Park, and I. K. Yoo, “Effects of metal electrodes on the resistive memory switching property of NiO thin films,” *Appl. Phys. Lett.*, vol. 93, no. 4, p. 042115, Aug. 2008.

[93] M. Hasan, R. Dong, H. J. Choi, D. S. Lee, D.-J. Seong, M. B. Pyun, and H. Hwang, “Effect of ruthenium oxide electrode on the resistive switching of Nb-doped strontium titanate,” *Appl. Phys. Lett.*, vol. 93, no. 5, p. 052908, Aug. 2008.

[94] N. Ghenzi, M. J. Sánchez, F. Gomez-Marlasca, P. Levy, and M. J. Rozenberg, “Hysteresis switching loops in Ag-manganite memristive interfaces,” *J. Appl. Phys.*, vol. 107, no. 9, p. 093719, 2010.

[95] H. Y. Peng, L. Pu, J. C. Wu, D. Cha, J. H. Hong, W. N. Lin, Y. Y. Li, J. F. Ding, A. David, K. Li, and T. Wu, “Effects of electrode material and configuration on the characteristics of planar resistive switching devices,” *APL Mater.*, vol. 1, no. 5, p. 052106, Nov. 2013.

[96] D. M. Mattox, *Handbook of Physical Vapor Deposition (PVD) Processing*. William Andrew, 2010.

[97] BOSE, *IC Fabrication Technology*. McGraw Hill Education (India) Pvt Ltd.

[98] J. C. Hoogvliet and W. P. van Bennekom, “Gold thin-film electrodes: an EQCM study of the influence of chromium and titanium adhesion layers on the response,” *Electrochim. Acta*, vol. 47, no. 4, pp. 599–611, Nov. 2001.

[99] S. M. Sze, *Semiconductor Devices: Physics and Technology*. John Wiley & Sons, Limited, 2012.

[100] D. K. Schroder, *Semiconductor Material and Device Characterization*. John Wiley & Sons, 2006.

[101] C. Moreno, “New features in derivative La0.7Sr0.3MnO3 Thin Films: Spontaneous Outcropping and Nanoscale Reversible Resistive Switching,” Universitat Autonoma de Barcelona, 2010.

[102] A. Sawa, T. Fujii, M. Kawasaki, and Y. Tokura, “Hysteretic current–voltage characteristics and resistance switching at a rectifying Ti⁄Pr0.7Ca0.3MnO3 interface,” *Appl. Phys. Lett.*, vol. 85, no. 18, p. 4073, Sep. 2004.

[103] L. Peña, L. Garzón, R. Galceran, A. Pomar, B. Bozzo, Z. Konstantinovic, F. Sandiumenge, L. Balcells, C. Ocal, and B. Martinez, “Macroscopic evidence of nanoscale resistive switching in La2/3Sr1/3MnO3 micro-fabricated bridges.,” *J. Phys. Condens. Matter*, vol. 26, no. 39, p. 395010, Oct. 2014.

[104] D. Liu, N. Wang, G. Wang, Z. Shao, X. Zhu, C. Zhang, and H. Cheng, “Nonvolatile bipolar resistive switching in amorphous Sr-doped LaMnO3 thin films deposited by radio frequency magnetron sputtering,” *Appl. Phys. Lett.*, vol. 102, no. 13, p. 134105, 2013.

[105] Y. W. Xie, J. R. Sun, D. J. Wang, S. Liang, and B. G. Shen, “Reversible electroresistance at the Ag⁄La0.67Sr0.33MnO3 interface,” *J. Appl. Phys.*, vol. 100, no. 3, p. 033704, 2006.

[106] Z. Xu, K. Jin, L. Gu, Y. Jin, C. Ge, C. Wang, H. Guo, H. Lu, R. Zhao, and G. Yang, “Evidence for a crucial role played by oxygen vacancies in LaMnO3 resistive switching memories.,” *Small*, vol. 8, no. 8, pp. 1279–84, Apr. 2012.

[107] E. L. Nagaev, “Colossal-magnetoresistance materials: manganites and conventional ferromagnetic semiconductors,” *Phys. Rep.*, vol. 346, no. 6, pp. 387–531, Jun. 2001.

[108] H. L. Ju, J. Gopalakrishnan, J. L. Peng, Q. Li, G. C. Xiong, T. Venkatesan, and R. L. Greene, “Dependence of giant magnetoresistance on oxygen stoichiometry and magnetization in polycrystalline La 0.67 Ba 0.33 MnO z,” *Phys. Rev. B*, vol. 51, no. 9, pp. 6143–6146, Mar. 1995.

[109] Y. Tokura, “Orbital Physics in Transition-Metal Oxides,” *Science (80-.).*, vol. 288, no. 5465, pp. 462–468, Apr. 2000.

[110] N. A. Tulina and V. V. Sirotkin, “Electron instability in doped-manganites-based heterojunctions,” *Phys. C Supercond.*, vol. 400, no. 3–4, pp. 105–110, Jan. 2004.

[111] X. Chen, N. Wu, J. Strozier, and A. Ignatiev, “Spatially extended nature of resistive switching in perovskite oxide thin films,” *Appl. Phys. Lett.*, vol. 89, no. 6, p. 063507, Aug. 2006.

[112] H. Boschker, J. Kautz, E. P. Houwman, W. Siemons, D. H. A. Blank, M. Huijben, G. Koster, A. Vailionis, and G. Rijnders, “High-Temperature Magnetic Insulating Phase in Ultrathin La 0.67 Sr 0.33 MnO 3 Films,” *Phys. Rev. Lett.*, vol. 109, no. 15, p. 157207, Oct. 2012.

[113] J. Dho, N. H. Hur, I. S. Kim, and Y. K. Park, “Oxygen pressure and thickness dependent lattice strain in La0.7Sr0.3MnOsub 3 films,” *J. Appl. Phys.*, vol. 94, no. 12, p. 7670, Dec. 2003.

[114] L. Ranno, A. Llobet, R. Tiron, and E. Favre-Nicolin, “Strain-induced magnetic anisotropy in epitaxial manganite films,” *Appl. Surf. Sci.*, vol. 188, no. 1–2, pp. 170–175, Mar. 2002.

[115] A. Kalantarian, G. Bersuker, D. C. Gilmer, D. Veksler, B. Butcher, A. Padovani, O. Pirrotta, L. Larcher, R. Geer, Y. Nishi, and P. Kirsch, “Controlling uniformity of RRAM characteristics through the forming process,” in *2012 IEEE International Reliability Physics Symposium (IRPS)*, 2012, pp. 6C.4.1–6C.4.5.

[116] S. Park, J. Vohs, and R. Gorte, “Direct oxidation of hydrocarbons in a solid-oxide fuel cell,” *Nature*, vol. 404, no. 6775, pp. 265–7, Mar. 2000.

[117] A. Sawa, T. Fujii, M. Kawasaki, and Y. Tokura, “Hysteretic current-voltage characteristics and resistance switching at a rectifying Ti/Pr0.7Ca0.3MnO3 interface,” p. 3, Sep. 2004.

[118] S. Balatti, S. Member, S. Ambrogio, D. C. Gilmer, D. Ielmini, and S. Member, “Set Variability and Failure Induced by Complementary Switching in Bipolar RRAM,” vol. 34, no. 7, pp. 861–863, 2013.

[119] T. Sheahen, *Introduction to High-Temperature Superconductivity*. 1994.

[120] N. Roma, S. Morlens, S. Ricart, K. Zalamova, J. M. Moreto, A. Pomar, T. Puig, and X. Obradors, “Acid anhydrides: a simple route to highly pure organometallic solutions for superconducting films,” *Supercond. Sci. Technol.*, vol. 19, no. 6, pp. 521–527, Jun. 2006.

[121] X. Obradors, T. Puig, S. Ricart, M. Coll, J. Gazquez, A. Palau, and X. Granados, “Growth, nanostructure and vortex pinning in superconducting YBa 2 Cu 3 O 7 thin films based on trifluoroacetate solutions,” *Supercond. Sci. Technol.*, vol. 25, no. 12, p. 123001, Dec. 2012.

[122] J. Antoja Lleonart and A. Palau Masoliver, “Study of the resistive switching phenomenon in YBCO superconducting samples,” 2014.

[123] J. Gàzquez, F. Sandiumenge, M. Coll, A. Pomar, N. Mestres, T. Puig, X. Obradors, Y. Kihn, M. J. Casanove, and C. Ballesteros, “Precursor Evolution and Nucleation Mechanism of YBa 2 Cu 3 O x Films by TFA Metal−Organic Decomposition,” *Chem. Mater.*, vol. 18, no. 26, pp. 6211–6219, Dec. 2006.

[124] H. Castro and G. Deutscher, “Anomalous Fermi liquid behavior of overdoped high- T c superconductors,” *Phys. Rev. B*, vol. 70, no. 17, p. 174511, Nov. 2004.

[125] V. Breit, P. Schweiss, R. Hauff, H. Wühl, H. Claus, H. Rietschel, A. Erb, and G. Müller-Vogt, “Evidence for chain superconductivity in near-stoichiometric YBa 2 Cu 3 O x single crystals,” *Phys. Rev. B*, vol. 52, no. 22, pp. R15727–R15730, Dec. 1995.

[126] R. De Oliveira, D. Albuquerque, T. Cruz, F. Yamaji, and F. L. Leite, *Atomic Force Microscopy - Imaging, Measuring and Manipulating Surfaces at the Atomic Scale*. InTech, 2012.

[127] A. R. Barron, *Physical methods in chemistry*. 1992.

[128] B. B. He, *Two-Dimensional X-Ray Diffraction*, vol. 0. John Wiley & Sons, 2011.

[129] "The International Centre for Diffraction Data - ICDD." [Online]. Available: http://www.icdd.com/. [Accessed: 13-Oct-2015].

[130] "Four-Probe Resistivity and Hall Voltage Measurements with the Model 4200-SCS," in *Keithley user's guide*, no. 2475, 2007.

List of symbols and abbreviations

3T	three-terminal device
AFM	Atomic Force Microscopy
Ag	Silver
ALD	Atomic Layer Deposition method
Au	Gold
BHF	Buffer fluorhydric acid solution
BRS	Bipolar resistive switching
CeO_2	Cerium dioxide
CeO_{2-x}	Cerium dioxide out of stoichiometry
CI	Spin-canted insulating phase
CMOS	Complementary Metal-oxide-semiconductor
CRS	Complementary resistive switching
CSD	Chemical Solution Deposition method
C-SFM	Conductive atomic force microscopy
DRAM	Dynamic Random Access Memory
DUT	Device under test
FET	Field-effect transistor
FI	ferromagnetic insulating phase
FL	Fermi liquid phase
FM	Ferromagnetic phase
GND	Ground unit
HDD	Hard disk drives
HRS	High resistance state
I-V	Current-voltage curve also termed I(V)
L	Length of the track where resistance is being evaluated

LAO	Lanthanum aluminate $LaAlO_2$ substrate
LHB	Low Hubbard band
LRS	Low resistive state
LSMO	Lanthanum manganite doper Sr termed as well as $La_{1-x}Sr_xMnO_3$
MFL	Marginal Fermi level phase
MIM	Metal-insulator-metal structure
MIT	Metal-insulator transition
MOD	Metal-organic decomposition
MOM	Metal-oxide-metal architecture
Nb:STO	Strontium titanate doped Nb substrate
PCMO	Praseodymium manganite doped Ca
PG	Pseudogap semiconducting phase
PI	Paramagnetic insulating phase
PLC	Power line cycles (50Hz)
PLD	Pulsed laser deposition
PM	Paramagnetic phase
PPMS	Physical properties measurements system
Pt	Platinum
R	Resistance
R_C	Contact resistance
RE	Rare earth element
R_H/R_L	Resistance ratio
RIE	Reactive ion etching
RMS	Root mean square
RRAM	Resistive random-access memory
RS	Resistive switching
SC	Superconductivity phase

SQUID	Superconducting Quantum Interference Device
SMU	Source-meter unit
SRAM	Static Random Access Memory
STEM	Scanning Transmission Electron Microscopy
STO	Strontium titanate $SrTiO_3$ substrate
SUMAN	Superconducting materials and large scale nanostructures group
T	temperature
t	thickness
Tc	Curie temperature of the ferromagnetic-paramagnetic transition
TLM	Transmission line method
$T_{M\text{-}I}$	Metal-insulator transition temperature
TMOs	Transition metal oxides
U	Coulomb repulsion energy
UHB	Upper Hubbard band
URS	Unipolar resistive switching also known as non-polar
VCM	Valence change memory
V_{max}	Maximum voltage
W	Width of the track where resistance is being evaluated
XRD	X-ray diffraction
YBCO	Yttrium barium copper oxide $YBa_2Cu_3O_7$
Δ	Gap between the UHB and the oxygen 2p band
χ_{DC}	Magnetic susceptibility
ρ	Resistivity

Publication and conference contributions

Journal article

- R. Ortega-Hernandez, M. Coll, J. C. Gonzalez-Rosillo, A. Palau, X. Obradors, E. Miranda, T. Puig and J. Suñe. “Resisitve switching in CeO2/La0.8Sr0.2MnO3 bilayer for non volatile memory applications” *Microelectron Eng.,* vol. 147, pp 37-40, Nov. 2015

Conferences

- *European Material Research Society EMRS 2014.* DATES: 26-30 May, 2014. VENUE: Grand Palais Congress Center. Lille, France. TITLE: Resistive Switching observed in $CeO_2/La_{0.7}Sr_{0.3}MnO_3$ complex oxide bilayer. AUTHORS: R. Ortega-Hernandez, T. Puig, J. Suñé, J.C. Gonzalez-Rosillo, M.Coll, A. Palau, X.Obradors. Oral Presentation
- *NANOSELECT 2014.* DATES: 25-27 June, 2015. VENUE: Eden Roc, Sant Feliu de Guixols, Spain. TITLE: Resisitve switchin phenomena observed in $La_{0.8}Sr_{0.2}MnO_3$. AUTHORS: R. Ortega, J.C. González, M. Coll, A. Palau, X. Obradors, J. Suñé and T. Puig. Oral Presentation.

- *INSULATING FILMS ON SEMICONDUCTORS INFOS 2015.* DATES: 30 June – 3 July, 2015. VENUE: Palazzo Antonini, Udine, Italy. TITLE: Resistive switching in metallic $La_{0.8}Sr_{0.2}MnO_3$ for non-volatile memory applications. AUTHORS: R. Ortega-Hernandez, J. Gonzalez-Rosillo, M. Coll, A. Palau, X. Obradors, T. Puig, E. Miranda, J. Suñe. Poster